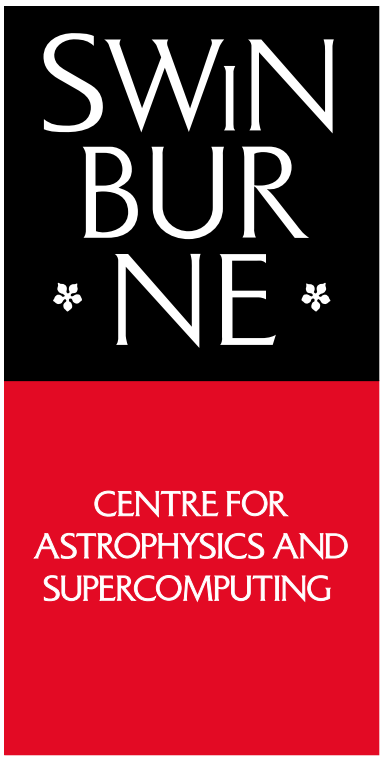

Kinematics and dynamics of extragalactic globular clusters

Vincenzo Pota

Presented in fulfillment of the requirements
of the degree of Doctor of Philosophy

2014

Faculty of Information and Communication Technology
Swinburne University

Abstract

In this work we study the kinematics and motions of globular cluster systems in nearby galaxies in the context of current galaxy formation scenarios. A globular cluster (GC) is a collection of thousands of stars notable for its compactness and high surface brightness.

We will discuss how the study of globular cluster systems allows us to:

1. explore galaxy haloes, for which simulations predict observable signatures of ancient assembly;

2. test whether the metallicity bimodality observed in GC systems is also present in GC kinematics;

3. study how the kinematics of GC systems can trace back the evolutionary history of the parent galaxy;

4. investigate if GC systems are linked to the supermassive black holes at the very centre of their host galaxies;

5. model the dark matter content of elliptical galaxies with unprecedented accuracy and infer their shape as a test of cosmological predictions.

We will make use of a state of the art dataset of GCs in external galaxies, from the SLUGGS survey. SLUGGS is the SAGES Legacy Unifying Globulars and Galaxies Survey, where SAGES is the Study of the Astrophysics of Globular Clusters in Extragalactic Systems. Galaxies are observed with wide-field ground-based and space-based telescopes in order to identify GCs. These are followed up with the DEIMOS multi-object spectrograph in order to measure their recession velocities and hence kinematics. To date, this is the largest, most homogeneous and most accurate spectro-photometric dataset of extragalactic GCs in external galaxies.

Our main findings are that some GC systems studied in this work have two kinematically distinct subpopulations, one sharing the physical properties of the bulge of the host galaxy, and the other more linked with the assembly of the host galaxy halo. We show that this property is not enough to distinguish whether the bulge or the halo of galaxies regulates the formation of supermassive black holes, probably because the dataset is still too small. The kinematic bimodality is used to show that the dark matter halo of the galaxy NGC 1407 has a dark matter density core, in contrast with dark matter cusps predicted in computer simulations. This is the first evidence of a dark matter core in an elliptical galaxy, and consistent with findings in dwarf galaxies and galaxy clusters.

Acknowledgements

A special “grazie” goes to my supervisor, Duncan, for his moral and financial support over these four years. I also want to acknowledge the members of my Swinburne team (Christina, Nicola, Chris, Caroline, Sreeja, Lee), the members of the SAGES collaboration (Aaron and Jean in particular) and Nicola Napolitano.

On more of personal note, I want to thank my new Australian friends. You have all given me something that I will carry deep inside me for the rest of my days. Thanks Gonzalo for playing rock and roll with me and for sharing thoughts and laughs. I’ll come to Argentina to see some punk rock concerts with you. Thanks Greg for watching the Beatles Anthology with me. Thanks Peter for showing me how never to give up. A special hug goes to Glenn, Rob, Elisa & Carina (psf), my fellow students and Charlotte. Thanks to Ben, Big Boy, Max and Valentine for helping me in difficult times and for being my Australian family over the last few months. Thanks to the Junk Company for the marvelous music we were able to create. Teresa, this is the second thesis in which I thank you for the way you are making my life marvelous. If one day I will write another thesis, I hope I will thank you in that one to.

I acknowledge financial support from a Swinburne University PhD scholarship, without which my PhD would not have been possible. Most of this work was carried out with Wolfarm Mathematica tools, for which Swinburne University provided full license. The figures for this thesis have been created using the excellent LevelScheme scientific figure preparation system (Caprio, 2005). Most of the data presented herein were obtained at the W. M. Keck Observatory, operated as a scientific partnership among the California Institute of Technology, the University of California and the National Aeronautics and Space Administration, and made possible by the generous financial support of the W. M. Keck Foundation. This research has made use of IRAF, which is distributed by the National Optical Astronomy Observatories and operated by AURA, Inc., under cooperative agreement with the National Science Foundation. This research has made use of the NASA/IPAC Extragalactic Database (NED) which is operated by the Jet Propulsion Laboratory, California Institute of Technology, under contract with the National Aeronautics and Space Administration.

Declaration

The work presented in this thesis has been carried out in the Centre for Astrophysics & Supercomputing at Swinburne University of Technology between April 2010 and December 2013. This thesis contains no material that has been accepted for the award of any other degree or diploma. All work presented is primarily that of the author. To the best of my knowledge, this thesis contains no material previously published or written by another author, except where due reference is made in the text of the thesis. Figure 1.2 was produced by the author specifically for the Introduction. The content of the chapters listed below has appeared in refereed journals. I acknowledge the contribution of co-authors on the publications. Minor alterations have been made to the published papers in order to maintain argument continuity and consistency of spelling and style.

- Chapter 2 has been published as Pota, Vincenzo; Forbes, Duncan A.; Romanowsky, Aaron J.; Brodie, Jean P.; Spitler, Lee R.; Strader, Jay; Foster, Caroline; Arnold, Jacob A.; Benson, Andrew; Blom, Christina; Hargis, Jonathan R.; Rhode, Katherine L.; Usher, Christopher, *The SLUGGS Survey: kinematics for over 2500 globular clusters in 12 early-type galaxies , 2013, MNRAS, 428, 389*;

- Chapter 3 has been published as Pota, Vincenzo; Graham, Alister W.; Forbes, Duncan A.; Romanowsky, Aaron J.; Brodie, Jean P.; Strader, Jay, *The SLUGGS survey: probing the supermassive black hole connection with bulges and haloes using red and blue globular cluster systems , 2013, MNRAS, 433, 235*;

- Chapter 4 is in advanced state of preparation, with title *Cusp or core? The shape of the dark matter halo of the galaxy NGC 1407 from stars and globular clusters*, to be submitted to MNRAS.

Vincenzo Pota
Melbourne, Australia
December 13, 2013

Contents

Abstract i

Acknowledgements ii

Declaration iv

List of Figures ix

List of Tables xii

1 Introduction 1

1.1 The current status of galaxy formation 1
1.2 Early-type galaxies 4
1.3 Globular clusters as trace particles 5
1.3.1 The globular cluster colour bimodality 5
1.3.2 Kinematic predictions 7
1.4 Globular clusters and supermassive black holes 7
1.5 Globular clusters and dark matter 10
1.5.1 The dark matter cusp/core problem 10
1.6 Thesis outline 13

2 Kinematics for over 2500 Globular Clusters in Twelve Early-type Galaxies 15

2.1 Introduction 15
2.2 The sample 16
2.3 Photometric observations and data analysis 19
2.3.1 Subaru data 19
2.3.2 HST data 21
2.3.3 Photometric GC selection 22
2.3.4 GC colour bimodality 25
2.3.5 GC spatial distribution 25
2.4 Spectroscopic observations and data analysis 27
2.4.1 Kinematic selection criteria 30
2.4.2 Repeated GC measurements 32
2.4.3 Kinematic analysis 32
2.4.4 Velocity-bias correction 40
2.5 Notes on individual galaxies 40

2.5.1 NGC 821 . . . 40
2.5.2 NGC 1400 . . . 43
2.5.3 NGC 1407 . . . 43
2.5.4 NGC 2768 . . . 44
2.5.5 NGC 3377 . . . 44
2.5.6 NGC 4278 . . . 49
2.5.7 NGC 4365 . . . 50
2.5.8 NGC 5846 . . . 51
2.5.9 NGC 7457 . . . 51
2.6 GC formation models . . . 53
2.7 Global results from our GC sample . . . 55
2.7.1 Spatial Distribution . . . 55
2.7.2 Rotation and velocity dispersion . . . 56
2.8 Including literature data . . . 57
2.8.1 Velocity Dispersion . . . 57
2.9 Results . . . 61
2.9.1 Correlations with host galaxy properties . . . 61
2.9.2 Rotation . . . 63
2.9.3 Kinematic misalignment . . . 68
2.9.4 The slope of the $V_{\rm rms}$ profile . . . 70
2.9.5 Kurtosis . . . 72
2.10 Discussion . . . 73
2.10.1 GC kinematic bimodality . . . 73
2.10.2 The star-GC system connection . . . 74
2.10.3 Orbital anisotropy . . . 75
2.10.4 NGC 7457: a case study for the formation of S0s . . . 76
2.11 Summary and Conclusions . . . 78

3 Globular clusters and supermassive black holes 81
3.1 Galaxy sample . . . 82
3.2 Method . . . 84
3.2.1 The globular cluster system velocity dispersion . . . 84
3.2.2 The $M_{\rm BH} - \sigma_{\rm GC}$ and $M_{\rm BH} - v_{\rm GC}$ relations for GC systems . . . 88
3.3 Results . . . 89
3.3.1 Radial trends . . . 90
3.3.2 Cores and bars . . . 92

3.3.3 Predicting $M_{\rm BH}$ in other galaxies 94
3.4 Discussion and conclusions 95

4 The dark matter content of NGC 1407 **97**
4.1 Introduction 97
4.2 Data 98
4.2.1 Distance and conventions 98
4.2.2 Stellar surface brightness 98
4.2.3 Stellar kinematics 100
4.2.4 Globular cluster surface density 101
4.2.5 Globular cluster kinematics 103
4.3 Jeans analysis 105
4.3.1 Dealing with kinematic substructures 106
4.4 Results 107
4.4.1 Stellar component 107
4.4.2 Globular clusters 110
4.5 Constructing the mass profile of NGC 1407 112
4.5.1 Deriving the "pinch radii" 112
4.5.2 The effect of the stellar mass-to-light ratio 115
4.5.3 The dark matter profile of NGC 1407 117
4.6 Discussion 119
4.6.1 The role of the IMF 119
4.6.2 Core formation 120
4.6.3 Comparison with previous studies 121
4.7 Conclusions 123

5 Conclusions **125**
5.1 Summary 125
5.2 Future directions 127

Bibliography **145**

List of Figures

1.1 The current galaxy formation paradigm 2
1.2 The halo of the elliptical galaxy NGC 1407 6
1.3 Correlations between SMHB mass and host galaxy properties. 9
1.4 Globular clusters and dark matter 11

2.1 Digitized Sky Survey (DSS) images of our galaxy sample 18
2.2 Accuracy of globular cluster radial velocity measurements 20
2.3 Colour-colour diagram of objects around NGC 1407 21
2.4 GC system colour-magnitude diagrams 24
2.5 Colour histograms of our galaxy sample 26
2.6 Surface density profiles of the GCs brighter than the turnover magnitude 28
2.7 GC radial velocity distributions with galactocentric radius 31
2.8 Comparison of our GC radial velocities with previous studies 33
2.9 Repeated GC radial velocity measurements 34
2.10 Rotation of NGC 3377 GC system with position angle in different radial bins . . 37
2.11 GC system kinematics compared to stellar data 45
2.12 GC kinematics as a function of colour 47
2.13 Two-dimensional smoothed velocity fields of our disky early-type galaxies 52
2.14 GC rotation velocities and velocity dispersions compared to the galaxy stars/PNe 58
2.15 Velocity dispersion profiles 59
2.16 Summary of GC system kinematics as a function of the host galaxy properties . . 62
2.17 GC system $V_{\rm rms}$ as a function of the host galaxy properties 64
2.18 Rotational dominance parameter of the stellar component λ_{R_e} versus the galaxy ellipticity ϵ_{R_e} 65
2.19 The rotational dominance parameter of GC systems 66
2.20 $(V_{\rm rot}/\sigma)$ radial profiles for our galaxy sample 67
2.21 GC system position angle misalignments 69
2.22 Log-slopes of the GC system $V^2_{\rm rms}$ profiles 71
2.23 GC system velocity kurtosis 72
2.24 GC rotation rate in NGC 7457 77

3.1 Difference between the rotation-subtracted velocity dispersion and the rotation-included velocity dispersion without any colour split 84
3.2 Black hole mass as a function of rotation-included GC system velocity dispersion 86
3.3 Cumulative root-mean-square velocity dispersion profiles 91

3.4 Best-fit $M_{\rm BH} - v_{\rm GC}$ relation within different radial bins 92
3.5 $M_{\rm BH} - v_{\rm GC}$ relation 93

4.1 Stellar data 99
4.2 Photometric GC system properties as a function of colour 102
4.3 Globular cluster data 104
4.4 Stellar component dynamical results 108
4.5 Best-fit parameters for stars and globular clusters 110
4.6 Globular cluster results 111
4.7 Cumulative mass profiles for stars and globular clusters 114
4.8 Uncertainty on the dark matter mass 115
4.9 Cumulative mass profile of NGC 1407 116
4.10 Best fit DM halo parameters 118
4.11 Comparison with literature studies 122

List of Tables

2.1 General properties of the SLUGGS galaxy sample 17
2.2 Summary of the ground-based imaging observations 22
2.3 KMM results 25
2.4 Summary of the spectroscopic observations for our twelve galaxies 29
2.5 Spectro-photometric catalogue of objects around NGC 3377 39
2.6 GC kinematic results for our galaxy sample 42
2.7 Kinematical properties of literature GC systems 60

3.1 Galaxy sample 83
3.2 Solutions to $\log(M_{\rm BH}/M_{\odot}) = \alpha + \beta \log(\sigma_{\rm GC}/200\,{\rm km\ s^{-1}})$ for different GC subsets 87
3.3 Black hole mass predictions 95

4.1 GC photometric parameters 102
4.2 Important dynamical quantities for different DM haloes in NGC 1407 119

1 Introduction

This thesis will focus on studying the formation of elliptical galaxies and their dark matter content through the use of extragalactic globular clusters.

A globular cluster is a gravitationally bound collection of millions of stars compressed within a few parsecs. As fossils, which allowed scientists to reconstruct the evolution of planet Earth over millions of years, so globular clusters can be thought of as the fossil record of galaxy evolution. Most globular clusters will remain attached to the parent galaxy for their whole existence, witnessing its metamorphosis with time. In this Chapter, I will first overview our current understanding of galaxy formation theory. I will then describe why the combination of old ages, chemical abundances and compactness of globular clusters is so important for our understanding of galaxy formation.

1.1 The current status of galaxy formation

The theory of galaxy formation is experiencing exciting times thanks to the imminent advent of new powerful telescopes and to the exponential rise in computing power. The need for these new technologies is motivated by the fact that although a clear picture of galaxy formation is slowly emerging, there are still many aspects that are not fully understood. After almost a century since the "great debate", which marked the beginning of extragalactic astronomy (Shapley & Curtis, 1921), it has been realized that galaxies form in different flavors at different cosmic times, with gravity being the undisputed leading force driving the various formation processes.

Galaxy mergerers and gravitational collapse are key most important processes in galaxy formation. They converge in the so called "two-phase" galaxy formation model, introduced by (Eggen et al., 1962) and (Searle & Zinn, 1978) and re-developed in the last few years (Oser et al., 2010; Gobat et al., 2011), The novelty of this model is that it accommodates the early "monolithic collapse" in which galaxies form via the collapse of a primordial gas cloud (Larson, 1975), and the

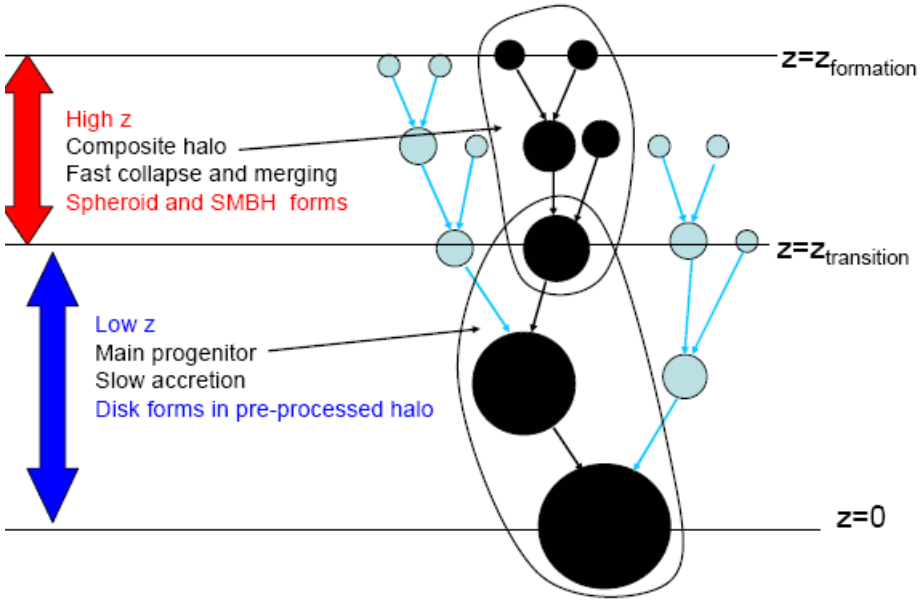

Figure 1.1 Cartoon showing the current galaxy formation paradigm. Galaxies form in dark matter haloes (cyan and black circles) on the top of the diagram, at high redshift. This is when the bulk of the star formation occurs, including processes such as the formation of supermassive black holes (SMBHs). During this phase, some haloes merge and some other haloes will evolve in isolation. As the redshift decreases $z \leq 2$, most of the mass is gathered through accretion of satellite galaxies into the halo outskirts. This phase is more quiescent with little or absent star-formation. Figure from Cook et al. 2009.

latest hierarchical scenario in which massive galaxies are created from merging of smaller structures (Toomre & Toomre, 1972). The idea behind the "two-phase" model is that compact "seed" galaxies form "in situ" at redshift $z > 2$ from dissipative cold gas collapsing toward the centre of the system. Galaxy haloes then grow from $z < 2$ to the present epoch, fed by "ex situ" minor mergers and accretion of lower mass systems (see Figure 1.1). Galaxy-galaxy mergers also occur, but their contribution to the mass budget of the final galaxy is still debated (e.g., Naab et al., 2007). Nowadays, the two-phase formation scenario is gaining acceptance by the scientific community and the first tests have returned encouraging results. It is important to state that even if the astronomical community is slowly converging towards a consensus galaxy formation theory, this is very different from saying that we really "understand" how all galaxies form. Each known galaxy appears to be unique, with its own history, which in turn depends on a variety of factors and physical processes, such as the environment and feedback.

Galaxy formation scenarios can be tested with two different observational approaches. One can study galaxies at different redshifts and observe how they the evolve with time (e.g., Bauer et al., 2013; Weinmann et al., 2011; Rodighiero et al., 2011; Guo et al., 2011). This approach is probably the most successful in current times, as shown by the imminent advent of telescopes such as ASKAP or JWST, designed to target the high redshift Universe. With this approach galaxies have been found to become more clumpy, turbulent and star forming as one moves to higher redshifts (Green et al., 2010).

The other approach to study galaxy formation is to observe galaxies as they are at the present time. Galaxies at redshift $z = 0$ are the product of all transformations they went through when they were younger. For instance, if a galaxy is surrounded by shells or it shows surface brightness substructures, it is likely that it has undergone a merger event even if we do not see the merging happening (Tal et al., 2009; Martínez-Delgado et al., 2010). This can also be done by looking for substructures into the kinematics of the galaxy (like rotation or velocity dispersion of the stars), because the long dynamical times of the halo preserves these structures. These observations can be conducted efficiently only for galaxies in the local universe for which the instrumental resolution and the signal-to-noise are both maximized. In this thesis we will only study nearby galaxies around 20 Mpc away or closer.

The other advantage of observing galaxies in the local Universe is that simulations make specific prediction about the physical properties of the Universe at the present time. In most cases, the important observational imprints of primordial evolution have to sought in the *halo* of galaxies. Here "halo" refers to galactocentric distances $R \gg R_e$, where R_e is the effective radius of the galaxy, which is the radius that encompasses half of the total luminosity of the galaxy. Therefore, this definition of halo alludes both to the luminous and to the dark matter haloes. Simulations

involving dark matter predict, for instance, that galaxy haloes at $z = 0$ should host a large number of satellite galaxies as the result of the intense accretion events they undergone at high redshift (Moore et al., 1999; Boylan-Kolchin et al., 2011). The role of dark matter in this puzzle will be discussed in detail in §1.5.

The importance of galaxy haloes holds true also for the two-phase formation scenario, which focuses more on baryonic rather than dark matter. Moreover, such a scenario predicts that the signatures of past accretion should be detected in the kinematics of the final galaxy even when the merger/accretion product is settled and relaxed (Hopkins et al., 2009). For instance the merger of two spiral galaxies would cause the angular momentum to be transported to the outer regions of the merger product and detected as rotation, even if the galaxy is not rotating in the inner regions.

1.2 Early-type galaxies

The theoretical framework discussed above is challenging to test especially for early-type galaxies (ETGs), a galaxy morphological type which includes both elliptical and lenticular galaxies (Hubble, 1926). The halos of ETGs have been hard to observe for decades, until the advent of new technologies and new observational techniques. The reason is that ETGs lack the extended neutral hydrogen (HI) which traces the potential of spiral galaxies halos (Sofue & Rubin, 2001). For ellipticals closer than a few Mpc, HST observations can resolve giant stars up to several R_e (Harris et al., 2007a). The problem arises for galaxies further than 10 Mpc. In this case the low surface brightness of galaxy outskirts makes observations of the integrated stellar light not feasible in short (< 10 h) exposure-time on 10-meter class telescopes. Moreover, to have a compelling view of the physics of the halo, multi-band imaging observations should be followed-up with spectroscopic observations, which provide a measure of the spectral metallicity and kinematics of the system. This is the idea behind the SAURON-project (Cappellari et al., 2006), recently updated to the ATLAS^{3D}-project (Cappellari et al., 2011), that exploited integral field unit (IFU) observations to measure, all in one, photometry, chemistry and kinematics for hundreds of ETGs in the local universe. This approach allows short exposure time of galaxy centres on a 4-meter telescope (~ 2 hours per galaxy) with active optics. However, IFU is only efficient at the centre of galaxies ($R \leq R_e$), where the signal from the galaxy light is stronger. The study of the central regions only, can lead to misleading results as shown by the novel approach to IFU introduced by Arnold et al. (2013).

Outside $3R_e$ galaxy haloes are usually studied with the so called "discrete tracers". These are unresolved stars or clusters of stars that can be observed up to tens of effective radii. An example is given by planetary nebulae (PNe), which are excellent discrete tracers of the galactic potential at large radii (Coccato et al., 2009).

1.3 Globular clusters as trace particles

In this challenge of observing as far as possible from the galaxy centre but, at the same time, finding a trade-off between the number of dimensions in the phase-space and a feasible observation time, globular clusters (GCs) play a starring role. Globular clusters are dense (10^6 $M_\odot$ compressed within few parsecs) agglomerates of coeval stars, formed in the early universe (> 10 Gyr, Strader et al. 2005). Some GCs are compact enough to survive violent galaxy mergers and to preserve the chemo-dynamical information of their parent galaxy. They are also very common (all giant ellipticals, spirals and some dwarf galaxies in local universe host GCs) and largely more extended than the galaxy diffuse light (Bassino et al., 2006). A representative example of the radial extent of a GC system is shown in Figure 1.2 for the galaxy NGC 1407.

Over the last ten years, the advent of 10 meter class telescopes, furnished with wide-field cameras (e.g. Gemini/GMOS, Subaru/S-Cam, CFHT/MagaCam) and multi-object spectrographs (e.g. VLT/FLAMES or Keck/DEIMOS), have made the spectro-photometric study of extragalactic GCs more and more feasible (see Chapter 2). For example, one dark night in photometric conditions at Subaru/S-Cam and Keck/DEIMOS returns, on average, thousands of GC candidates and 150 spectroscopically confirmed GCs. The versatility of these objects has made GCs, along with planetary nebulae, the leading "trace particles" of the galactic potential at large radii.

In the context of the two-phase galaxy formation model, the leverage of globular clusters can be qualitatively understood by thinking that if a large galaxy accretes a large number of dwarf galaxies, these will spread their GC systems in the halo of the large galaxy. This effect can be measured as a radial GC colour/metallicity gradient (Forbes et al., 2011). Another approach is to exploit the GC kinematics to "see" ongoing accretion (Romanowsky et al., 2011).

1.3.1 The globular cluster colour bimodality

What makes the study of GC systems even more interesting, is the bimodality seen in their colour distribution. A GC system can usually be divided into two subpopulations: blue GCs are metal-poor (Usher et al., 2012), big (with mean half-light radius $R_h \sim 3.2$ pc, Masters et al. 2010), usually associated with the halo of the host galaxy (Faifer et al., 2011; Forbes et al., 2012a) and therefore more numerous in the outer regions of the galaxy. Red GCs are metal-rich, they are smaller than the blues ($R_h \sim 2.8$ pc) and they are more centrally concentrated than the blue GCs because they trace the bulge/spheroid component of the host galaxy. The kinematics (such as rotation velocity and velocity dispersion) of the two GC subpopulations are also very different, as it will be shown in Chapter 2. Moreover, the mean colour of metal-poor and metal-rich are found to correlate with the general properties of their host galaxy as shown by the ACS Virgo Survey

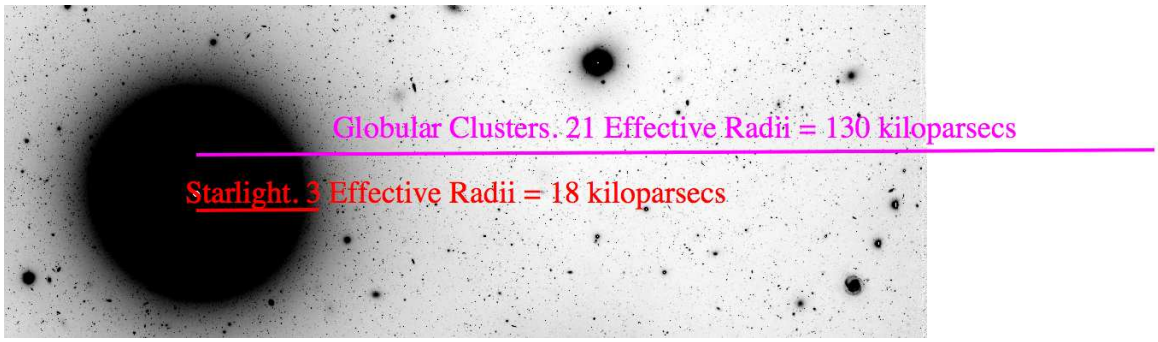

Figure 1.2 The halo of the elliptical galaxy NGC 1407. Shown is the radial extent of the globular cluster system (magenta) of NGC 1407 compared to the starlight (red). Most of the small point sources in the image are NGC 1407's GCs. Stellar light can map the galaxy kinematics up to ~ 3 R_e (Arnold et al., 2013), whereas GCs can probe the galaxy halo tens of kiloparsecs deep into the halo.

project (Peng et al., 2006).

As the GC colour bimodality will be a key topic of this thesis, it is worth discussing the proposed explanation for this dichotomy.

Thus far, the three leading scenarios are: (i) the *major merger scenario* (Ashman & Zepf, 1992), in which red GCs are formed during the merger between two gas-rich galaxies, while blue GCs come from the halos of the disk galaxies. (ii) *multiphase dissipational collapse scenario* (Forbes et al., 1997a), in which the two subpopulations would be the result of distinct star formation episodes of the collapsing primordial galaxy: blue GCs are formed in the first star formation phase, while the red GCs are formed subsequently after the gas in the galaxy is self-enriched; (iii) the *dissipationless accretion scenario* (Côté et al., 1998), in which red GCs are formed in a dissipational monolithic collapse of a primary protogalactic cloud, while the blue GCs are subsequently captured from less massive satellite galaxies through merger or tidal stripping. Beasley et al. (2002) joined the three classic scenarios, to explore GC bimodality in a cosmological context using the semi-analytic galaxy formation models. The key assumption of this simulation was that metal-poor GCs were assumed to form in the early universe in collapsing gas disks embedded in low mass dark matter haloes. In order to produce bimodality, Beasley and colleagues found it necessary to invoke the quenching of blue GC formation at high redshift ($z > 5$). Recently, Tonini (2013) simulated the formation of GC systems in the context of the two-phase galaxy formation scenario. She finds that metal-rich form in-situ at redshift $z \sim 2$, while the blue GCs were born at slightly higher redshift ($z \sim 3 - 4$) and were subsequently accreted into the halo of the larger galaxies. The fact that the formation mechanism of GC bimodality is a natural consequence of the two-phase formation model, suggests that GC bimodality can be an optimal tool to test this scenario.

1.3.2 Kinematic predictions

Under the assumption of a given GC formation scenario, we expect some sort kinematical distinction between the blue and the red GCs. Some numerical simulations which provide predictions on the kinematic properties of the GC systems in galaxies are either modeled on specific galaxies (Vesperini et al., 2003; Kravtsov & Gnedin, 2005) or do not provide predictions easily testable with observations (Diemand et al., 2005). A first attempt in simulating GC kinematics came from Bekki et al. (2005), that presented the results of a simulation of dissipationless major mergers of spiral galaxies with pre-existing metal-poor and metal-rich GCs having a spatial distribution similar to that of the Milky Way. The salient predictions of this simulation were that the rotation velocity (velocity dispersion) increases (decreases) both for metal-poor and metal-rich GCs and that the ratio of the maximum rotational velocities V to central velocity dispersions σ_0 in GC systems is expected to be large ($V/\sigma_0 > 0.5$). A few years later, Bekki et al. (2008) studied the origin of GCs using high-resolution cosmological N-body simulations combined with semi-analytic models of galaxy formation. Their main findings are: (i) the velocity dispersion of the metal-poor and metal-rich GCs increase according to the total luminosity of their host galaxy; (ii) the ratio of the velocity dispersion between the two subpopulations is almost one for a wide range of total luminosity of their host galaxy; (iii) the ratio of the rotation velocity to the velocity dispersion is expected to be low ($V/\sigma < 0.3$) for most of the galaxies.

Until the end of 2012, only an handful of galaxies with well studied GC kinematics existed (5 galaxies with more than 100 GC radial velocities, see Lee et al. 2010a for a summary). Moreover, these galaxies are all giant ellipticals (gEs), fairly easy to observe and representative of a galaxy cluster environment. In addition, the published radial velocities have typical uncertainties $40 < \delta V < 150$ km s^{-1}, which is too large to detect the rotation signal in a system expected to be pressure supported or any substructures.

All these points will be elaborated in detailed in Chapter 2, in which we will present the results of the largest spectro-photometric survey of GC systems to date. Our dataset, collected over a period of seven years, is three times larger and two times more accurate than the literature sample from the last twenty years.

1.4 Globular clusters and supermassive black holes

It has been so far discussed how galaxy haloes are important for our knowledge of galaxy formation. The very innermost regions of galaxies ($R \ll R_e$) can also retain signatures of their primordial evolution. Most large galaxies are known to host a supermassive black hole (SMBH) at their centres, which is several order of magnitude more massive than its stellar counterpart. SMBHs

can be detected by looking at the motion of stars or gas that surround them (see for instance the 'reverberation mapping technique' Peterson et al. 2004).

There are now well-established correlations between the mass of SMBHs $(M_{\rm BH})$ and the properties of the host galaxy (see Kormendy & Ho 2013 for a review). An important point is that galaxy-black hole connections involve only properties of galaxy bulges (in spirals) or of the galaxy overall (in the case of ellipticals). SMBH mass is known to correlate with dark matter mass (Baes et al., 2003; Ferrarese, 2002; Kormendy & Bender, 2011), luminosity (Merritt & Ferrarese, 2001; Marconi & Hunt, 2003; Graham & Driver, 2007; Gültekin et al., 2009b; Scott & Graham, 2013; McConnell & Ma, 2012) and stellar velocity dispersion of galaxy bulges (Ferrarese & Merritt, 2000; Tremaine et al., 2002; Ferrarese & Ford, 2005; Beifiori et al., 2012; Scott & Graham, 2013; McConnell & Ma, 2012). The last two correlations are shown in Figure 1.3. Theoretically, researchers have studied the relative tightness and slope of these relations, to infer what they mean in terms of galaxy formation and evolution (e.g., Croton, 2006; Johansson et al., 2009; Zhang et al., 2012). The current scenario is that primordial galaxy mergers are the driving processes which seeded the black hole in the first place, even at high redshift $(z \sim 7)$ when the Universe was less than a Gigayear old (Fan et al., 2006). Consequent gas-rich mergers and AGN feedback contributed to the co-evolution of bulge and SMBH, which results in the galaxy bulge – SMBH connection we observe today. Other formation scenarios also include the collapse of a primordial gas cloud at high redshift (Begelman et al., 2006), as well as core-collapse of a dense star cluster at the galaxy centre (Spitzer, 1987).

At high redshift, some of the oldest globular clusters were already in place and they may have witnessed the events which formed the black hole at the centre of their host galaxy. Although GCs fall too deep into the halo to feel the effect of the central black hole, there is a surprisingly good correlation between GC properties (total number of GCs per galaxy and GC system velocity dispersion) and the mass of the SMBH (e.g., Burkert & Tremaine, 2010; Harris & Harris, 2011; Rhode, 2012). However, this does not necessarily imply a primary correlation between GCs and SMBHs (Jahnke & Macciò, 2011). In fact, Snyder et al. (2011) argued this correlation to be indirect, as expected if it was a consequence of the debated black hole fundamental plane (Hopkins et al., 2007; Graham, 2008).

Even if secondary, the link between GCs and SMBHs can be used as a tool to test the current SMBH scenarios. For a given galaxy, one can study how the blue and the red GCs correlate with the host galaxy SMBH mass. A distinct correlation is expected because if the growth of SMBHs is primarily driven by recent merger events, we should observe a stronger correlation between red GCs and SMBHs. Conversely, if the properties of SMBHs were set during the primordial formation of their host galaxies, we might expect a stronger correlation with blue GCs (Omukai

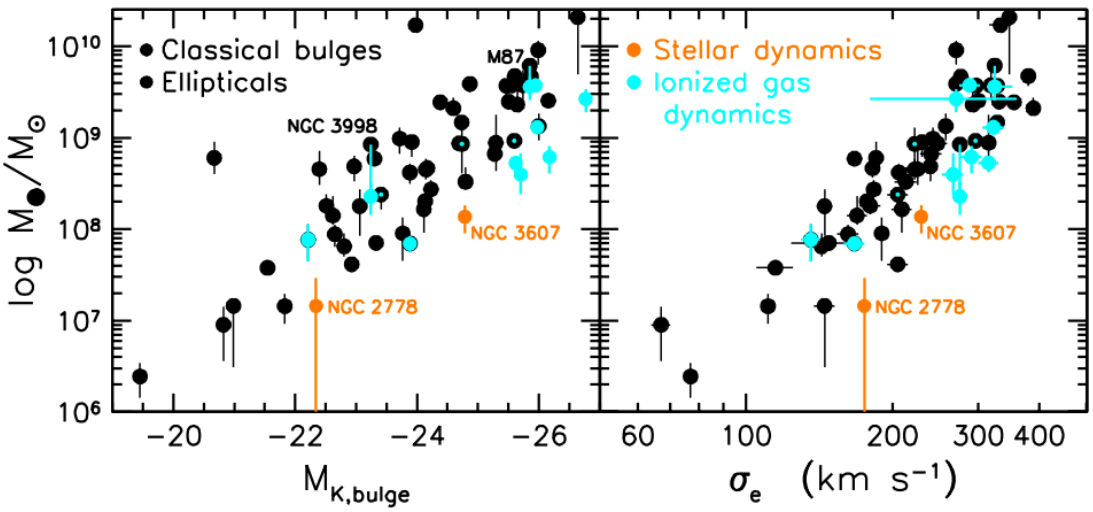

Figure 1.3 Correlations between SMHB mass (in this case $M_\bullet$) and host galaxy properties. The left and right panels show how $M_\bullet$ correlates with absolute magnitude M_K and stellar velocity dispersion within one effective radius σ_e, respectively. Orange and cyan datapoints represent galaxies with dubious $M_\bullet$ measurements (see Kormendy & Ho 2013 for details) . The correlation between $M_\bullet$ and σ_e is tightest. Figure from Kormendy & Ho (2013).

et al., 2008; Mayer et al., 2010; Debattista et al., 2013).

Studying SMBHs with globular clusters is not an easy task. Although the velocity dispersion of the stars is studied with well established techniques (such as long slit spectroscopy) and analysis software (such as the Penalized Pixel-Fitting algorithm), GC system properties have been measured with different approaches by different research groups. For instance, the number of photometric bands employed to select GCs or the model adopted to measure the GC kinematics will have an impact on the inferred GC system properties. Therefore, the *homogeneity* of the dataset is a crucial point and it must be taken into account before combining GC properties from different authors.

The topic of Chapter 3 will be centered on the correlation between $M_{\rm BH}$ and the GC system velocity dispersion. The latter is relatively easy to homogenize and it has the advantage of being directly comparable with the stellar $M_{\rm BH}$-velocity dispersion relation. With twenty-one GC system velocity dispersions re-analyzed with the same method (half of which come from the literature), we will try to answer the question: do the blue and red GCs correlate differently with $M_{\rm BH}$?

1.5 Globular clusters and dark matter

Astronomers believe that some sort of dark matter makes up most of the mass of the Universe. This type of matter is thought to be cold, non-baryonic, it does not emit any radiation, and it has been so far only detectable via indirect methods. The dark matter (DM) combined with the even more mysterious dark energy (Λ) give rise to the ΛCDM paradigm, which is the current consensus model for the formation of large scale structures. The reason why we need to invoke dark matter is because there are several astrophysical phenomena which cannot be explained without it. These include gravitational lensing (e.g., Kochanek, 1995) and the flat rotation curves of spiral galaxies (e.g., Rubin & Ford, 1970). It is very important to make clear that this mysterious dark matter is not the only theory aiming to explain certain physical processes. Theories such as MOND (Milgrom, 1983), and Extended Theories of Gravity (e.g., Buchdahl, 1970; Faraoni & Capozziello, 2011) are nowadays an active area of research. Although still in a pristine state, these alternative theories can also explain the Universe without the need of dark matter. Therefore they have been gaining increasing attention over the last few years. In this thesis we will assume that that dark matter exists, and we will want to study its properties at galactic scale.

1.5.1 The dark matter cusp/core problem

One of the reasons for studying dark matter at galactic scales is explained as follows. From comparing numerical simulations to observations, the emerging picture is that although the ΛCDM model can explain observables at large scale, it fails when it comes to galactic or sub-galactic scales. In the latter case, numerical simulations make predictions regarding the properties of galactic dark matter haloes, such as their mass (e.g., Springel et al., 2008), the amount of satellite galaxies they should host (Moore et al., 1999; Boylan-Kolchin et al., 2011) and their shape (Navarro et al., 1997, hereafter NFW). The latter, known as the "cusp/core problem", has become very popular in recent years because it can be tested with the increasing amount of high quality data. The ΛCDM model predicts that DM haloes follow a universal mass density profile, known as 'NFW' profile, which has density cusp at the galaxy centre, opposite to a flat or 'cored' profile.

The cusp/core problem is now relatively well studied in spiral galaxies (Chemin et al., 2011), dwarf ellipticals (Kuzio de Naray et al., 2008; Battaglia et al., 2008; Walker & Peñarrubia, 2011; Oh et al., 2011; Amorisco & Evans, 2012; Agnello & Evans, 2012; Cole et al., 2012; Amorisco et al., 2013; Richardson & Fairbairn, 2013) and galaxy clusters (Sand et al., 2004; Zitrin et al., 2010; Newman et al., 2013). At all these scales, results suggest that the inner slope of the DM profile is consistent with cores, rather than with cusps. Energetic baryonic feedback from supernovae (in dwarf ellipticals) and AGN (in giant ellipticals and clusters) are thought to be the physical

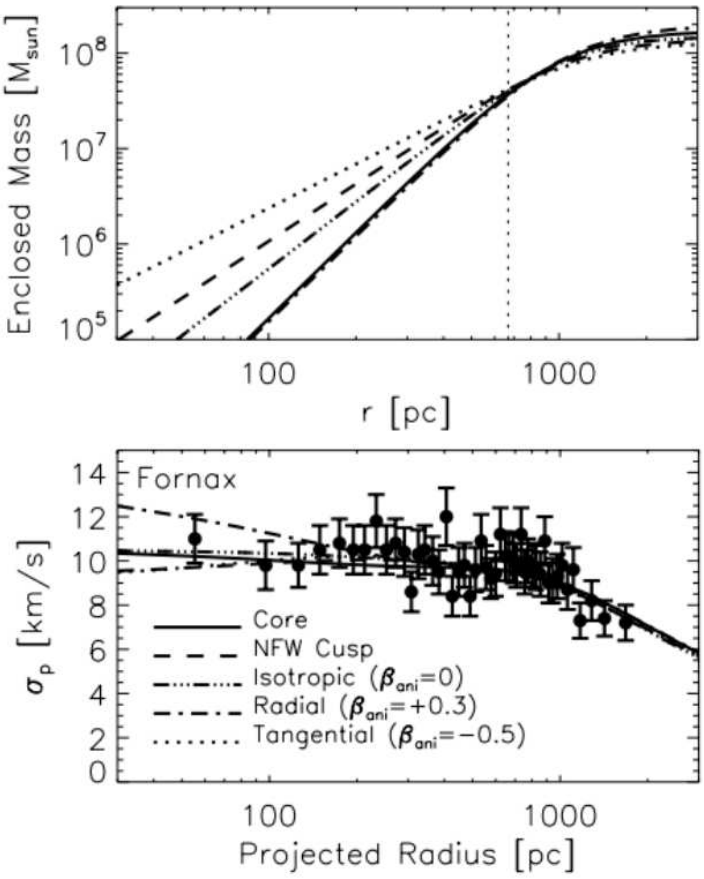

Figure 1.4 Left: Projected stellar velocity dispersion profile for the Fornax dwarf-spheroidal. Over- laid are spherical Jeans models which differ on the shape of dark matter halo and on the stellar orbits assumptions. Right: Enclosed-mass profiles corresponding to the same models, with the vertical line showing the radius within which the uncertainty from the modelling assumptions is minimized. Plot from Walker et al. (2009).

processes responsible for the removal of the DM cusp from the central regions (Peñarrubia et al., 2012; Governato et al., 2012; Pontzen & Governato, 2012; Teyssier et al., 2013; Martizzi et al., 2013). Computer simulations that do not specifically include AGN feedback in ellipticals, tend to produce DM halos which retain the primordial cusp (e.g., Di Cintio et al., 2013).

At the same time, little is known observationally about the shape of the dark matter profiles in giant elliptical galaxies. This is a serious limitation given the importance of elliptical galaxies (early-type galaxies in general) for the stellar mass budget of the Universe (e.g., Bell et al., 2003). As already explained in §1.2 the haloes of elliptical galaxies are hard to observe because they are optically faint. A way to get around with this, is to observe haloes with discrete tracers, such as planetary nebulae and globular clusters, or diffuse tracers, such as hot X-ray gas. Theoretically, the mass content of elliptical galaxies can be modelled through the Jeans equations (Jeans, 1915), which are relatively easy to solve, but they require assumptions on the shape of the DM halo and they are affected by the well-known mass-anisotropy degeneracy. These two factors, together with the notorious uncertainty on the stellar-mass-to-light ratio, make estimates of dark matter masses too uncertain to solve the cusp/core problem in giant ellipticals (e.g., de Lorenzi et al., 2008; Napolitano et al., 2011).

The latest developments in dynamical modeling have revealed that the final uncertainty on the total mass profile of a given galaxy is minimized at one particular galactocentric radius, that we dub the "pinch radius" (Walker et al., 2009; Wolf et al., 2010; Amorisco & Evans, 2011). At the pinch radius, which corresponds roughly to the half-light radius of the potential tracer, our ignorance of the orbital anisotropy and the shape of the DM mass profile contributes minimally to the galaxy mass uncertainty. This peculiar property, shown in Figure 1.4, is useful in stellar systems that contain physically distinct tracers within the same gravitational potential. In the Jeans formalism, this means having multiple kinematically and spatially distinct subpopulations which can be modelled independently, returning multiple pinch radii. Although this technique cannot reconstruct the mass profile in detail, the slope of the galaxy mass profile can be inferred. This method has been successfully applied to dwarf galaxies (Walker & Peñarrubia, 2011; Amorisco & Evans, 2012).

In Chapter 4 we will discuss the first attempt to measure the shape of the DM halo of an elliptical galaxy by independently modelling its stellar population and its globular cluster system. With three independent gravitational tracers (i.e. stars, blue GCs and red GCs) we can derive the mass within three pinch radii with an accuracy of $\sim$20%, which is an enormous improvement compared to the a classic error of $\sim 70\%$ (Napolitano et al., 2011). The main source of uncertainty for our results is the debated initial mass function (IMF), because it determines the amount of stellar mass we have to subtract off the total mass in order to obtain the dark matter mass.

1.6 Thesis outline

This thesis is divided into five chapters, including this Introduction. In Chapter 2 we will investigate the topics discussed in Section 1.1 regarding galaxy formation. We will use the GC systems of 12 early type galaxies with up to 2500 confirmed GCs to study their kinematic properties. We will focus on the kinematics of the two subpopulations and we will try to answer the question: is the bimodality seen in GC system colours also present in their kinematics? We will then supplement our results with literature data to study how the kinematics of these GC systems can trace back the formation history of their parent galaxies. Chapter 2 is also the part in which the dataset that will be used throughout this thesis is described. This includes details on observations, data reduction and data analysis.

In Chapter 3 we will use the results discussed Chapter 2 to study the supermassive black hole mass – GC velocity dispersion relation for twenty-one GC systems. This will allow us to test whether the blue and red GCs correlate differently with $M_{\rm BH}$ as expected from the current SMBH formation and GC formation scenarios.

In Chapter 4 we will model the dark matter halo of the galaxy NGC 1407, a giant elliptical at a distance of 21 Mpc. The spectroscopic and photometric dataset for this galaxy is among the most accurate in the literature to date. Nevertheless, baryonic mass will still be a crucial quantity for the stability of our results. We will apply the novel "pinch radius" technique discussed in Section 1.5 to the stellar component, the blue GCs and the red GCs separately. We will combine the results for each of them to infer whether NGC 1407 has a DM cusp or a DM core at its centre. This is the first-of-its-kind test on an elliptical galaxy and it is a crucial test for the trustworthiness of the ΛCDM paradigm at galactic scale.

Finally, in Chapter 5 we will overview the results of this PhD thesis and we will suggest future directions. We will discuss in what measure our results contributed to unravel the: (i) GC bimodality formation scenario, (ii) connection between SMBHs and GCs, and (iii) the cusp/core problem in elliptical galaxies.

The dataset presented in this thesis is the product of the SLUGGS project and it has been collected over almost a decade thanks to the efforts of the members of this international collaboration.

2

The SLUGGS Survey: Kinematics for over 2500 Globular Clusters in Twelve Early-type Galaxies

2.1 Introduction

Current spectroscopic studies of GC systems have shown that the kinematics (e.g. rotation directions and rotation amplitudes) of the two GC subpopulations are somewhat diverse. The kinematics of the red GCs is usually akin to that of the host galaxy stars (Schuberth et al., 2010; Strader et al., 2011), perhaps due to a similar formation history (Shapiro et al., 2010). Whereas, the velocity dispersion of the blue GCs is typically larger than that of the red GCs (e.g., Lee et al., 2008b). Also intriguing is the fact that rotation has been detected for both the blue and the red GCs, regardless the mass or morphology of the host galaxy (Foster et al., 2011; Arnold et al., 2011).

Interpreting this variety of GC kinematics in the context of galaxy and GC formation has been limited due to the low number of galaxies with large GC radial velocity datasets. To date, this set includes only a dozen GC systems, most of which are nearby very massive ellipticals (see Lee et al. 2010b, for a summary). On the other side, numerical simulations on this front have mainly focused on the origin of GC metallicity and colour bimodality (e.g., Weil & Pudritz, 2001; Kravtsov & Gnedin, 2005; Yoon et al., 2006, 2011b), rather than on GC kinematic properties (e.g., Bekki et al., 2005, 2008; Prieto & Gnedin, 2008).

This scenario has left open several questions regarding the kinematics of GC systems: does the colour bimodality also imply kinematic bimodality? If so, do the kinematical differences between the blue and red GC subpopulations found in the most massive ellipticals also hold for $\sim L^*$ galaxies over the whole early-type sequence of the Hubble diagram? Furthermore, do the blue and red GC subpopulations rotate faster in the outer regions, as predicted in a formation in a disk-disk merging scenario (Bekki et al., 2005)? Can GC kinematics contribute to our understanding of the

formation of lenticular galaxies (e.g., Barr et al., 2007)?

This Chapter will present a spectro-photometric survey of 2522 extragalactic globular clusters (GCs) around twelve early-type galaxies, nine of which have not been published previously. Combining space–based and multi–colour wide field ground–based imaging, with spectra from the Keck DEIMOS instrument, an average of 160 GC radial velocities per galaxy are obtained. We will discuss the photometric properties of these GC systems, such as their spatial and colour distributions, and then we will focus on the kinematics of metal-poor (blue) and metal-rich (red) GC subpopulations to an average distance of $\sim$ 8 effective radii from the galaxy centre. We will also supplement our galaxy sample with literature data, and we will compare the properties of this large sample with the existing numerical predictions.

We confirm that the GC kinematics are coupled with the host galaxy properties and find that the velocity kurtosis and the slope of their velocity dispersion profiles is different between the two GC subpopulations in more massive galaxies.

2.2 The sample

In this Chapter we discuss a subset sample from the SLUGGS survey. This includes nine new galaxies, in addition to other three galaxies already published: NGC 4494 (Foster et al., 2011), NGC 3115 (Arnold et al., 2011) and NGC 4486 (Strader et al., 2011). The analysis and the specific results for these three galaxies have been extensively discussed in the respective papers. Therefore, their overall results will be discussed together with the other nine starting from Section 2.7.

The physical characteristics of the twelve galaxies are listed in Table 2.1, with their optical images shown in Figure 2.1. This galaxy sample extends the study of extragalactic GC systems into a new regime, which spans a wide range of luminosity, morphological type (from lenticulars to giant ellipticals) and environment (from field to clusters), with a velocity resolution three times better than typical previous studies. The latter point is shown is shown in Figure 2.2, in which we compare the intrinsic properties of our dataset with previous GC studies (that have employed various instruments including VLT/FLAMES, VLT/FORS2, Keck/LRIS or Gemini/GMOS).

Galaxy ID	Hubble Type	$V_{\rm sys}$ [km s^{-1}]	$R_{\rm eff}$ [arcsec]	$(m-M)$ [mag]	D [Mpc]	$M_{\rm K}$ [mag]	$A_{\rm K}$ [mag]	$PA_{\rm K}$ [degree]	$(b/a)_{\rm K}$
(1)	(2)	(3)	(4)	(5)	(6)	(7)	(8)	(9)	(10)
NGC 0821	E6	1718	51	31.85	23.4	−24.0	0.040	31	0.62
NGC 1400	SA0	558	31	31.05	26.8	−23.8	0.024	29	0.90
NGC 1407	E0	1779	72	32.30	26.8	−25.4	0.025	70	0.95
NGC 2768	E6	1353	93	31.69	21.8	−24.7	0.016	91	0.46
NGC 3377	E6	690	46	30.19	10.9	−22.7	0.013	46	0.58
NGC 4278	E2	620	34	30.97	15.6	−23.8	0.010	219	0.91
NGC 4365	E3	1243	60	31.84	23.3	−25.2	0.008	41	0.74
NGC 5846	E0	1712	61	31.92	24.2	−25.0	0.020	233	0.92
NGC 7457	S0	844	52	30.55	12.9	−22.4	0.019	125	0.54
NGC 3115	S0	663	85	29.87	9.4	−24.0	0.017	43	0.45
NGC 4486	E0	1284	81	31.18	17.2	−25.3	0.008	151	0.86
NGC 4494	E1	1344	53	31.10	16.6	−24.2	0.008	173	0.87

Table 2.1 General properties of our galaxy sample. The galaxy name (1) and Hubble Type (2) are from the NED database. The galaxy systemic velocity (3) and ellipticity corrected effective radius (4) are from Cappellari et al. (2011), otherwise from NED and the RC3 catalogue (de Vaucouleurs, 1991) if not in Cappellari et al. (2011). The distance modulus (5) and the respective distance in Megaparsec (6) are from Tonry et al. (2001) with a -0.06 correction as advocated by Mei et al. (2007), respectively. If the galaxy is in the ACS Virgo Survey, we use the distances from Mei et al. (2007). We assume that NGC 1407 and NGC 1400 lie at the same distance, computed as the average of the respective Tonry et al. (2001) distances. The K band absolute magnitude (7) is from 2MASS apparent magnitude at the distances given in column 6 and corrected for the foreground Galactic extinction given in column 8 (NED database). The photometric position angle (9) and axis ratio (10) are from 2MASS (Skrutskie et al., 2006). The last three galaxies have been analysed in separate papers (see text).

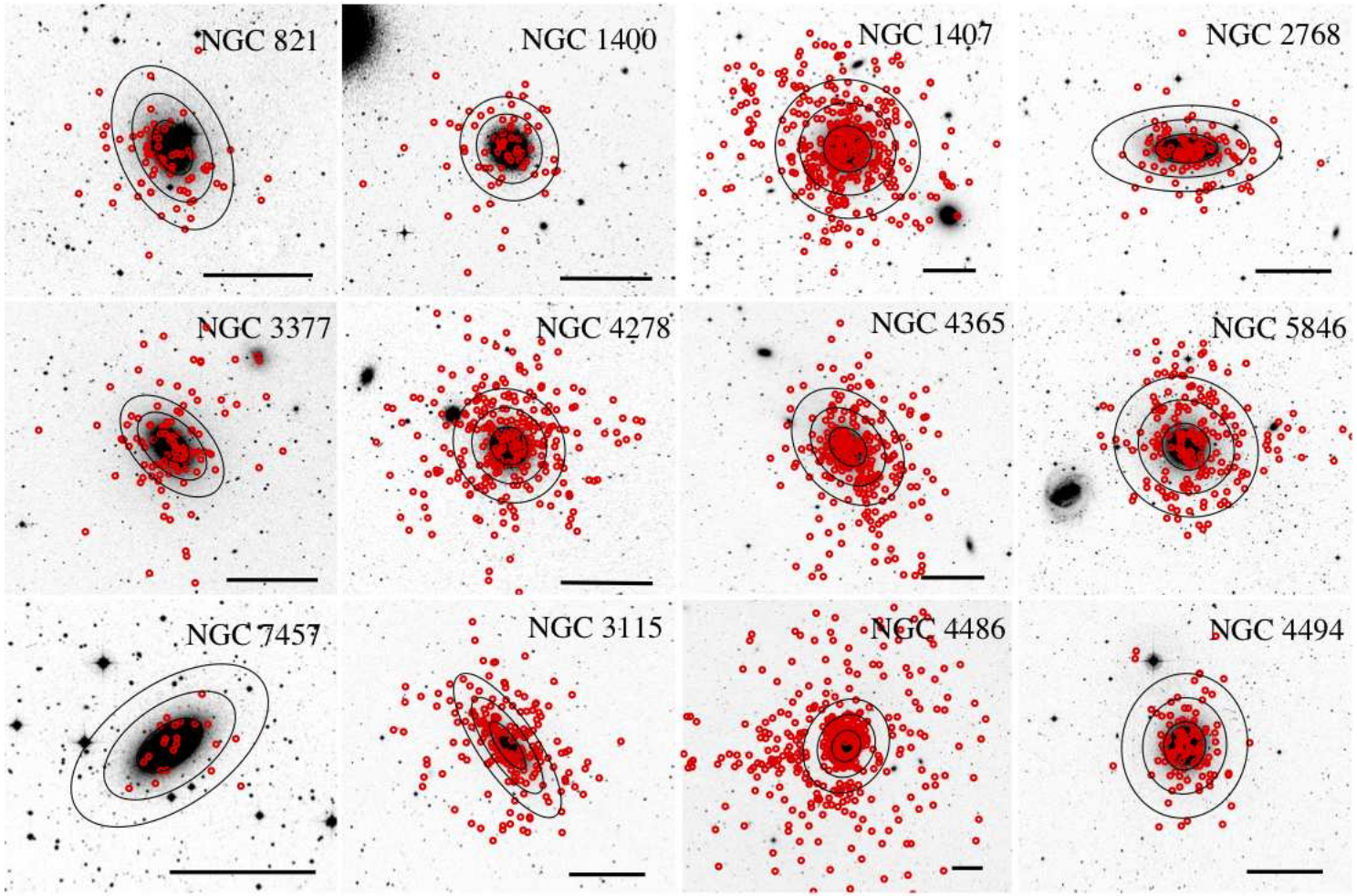

Figure 2.1 Digitalized Sky Survey (DSS) images of our galaxy sample. Red circles and black ellipses represent the spectroscopically confirmed GCs found in this work and the $2, 4, 6$ $R_{\rm eff}$ schematic isophotes corrected for the galaxy ellipticity respectively. The black line on the bottom-right spans 5 arcmin in length.North up and the East on the left. The elliptical galaxy south-west of NGC 1407 is NGC 1400 whose GC system is shown separately in this figure. The last three galaxies have been analysed in separate papers.

2.3 Photometric observations and data analysis

2.3.1 Subaru data

Multi-band photometric observations were carried out using the Subaru/Suprime-Cam instrument with a field of view of 34×27 arcmin^2 and a pixel scale of 0.202 arcsec (Miyazaki et al., 2002). The galaxy sample was observed in the period between 2005 and 2010 with a standard Sloan Digital Sky Survey (SDSS) gri filter set. NGC 2768 and NGC 4278 were both downloaded from the SMOKA archive (Baba et al., 2002) and were observed with a $R_{\rm C}iz$ and BVI filter set, respectively. For NGC 1407 and NGC 4365 we present existing Suprime-Cam photometry published in Spitler et al. (2012) (see also Romanowsky et al. 2009) and Blom et al. (2011), respectively. For these two galaxies both the imaging reduction and the catalogue extraction were performed with the methodology described in this Chapter. NGC 7457 is the only galaxy for which no Subaru imaging is available, and therefore we use WIYN/Minimosaic imaging in BVR filters presented in Hargis et al. (2011) and we refer to their paper for a description of the data reduction.

In Table 2.2 the imaging observations are summarized. The overall seeing conditions were mainly sub-arcsec. For NGC 821 (g band), NGC 5846 (g band) and NGC 4278 (B band) the data suffer from cloudy conditions and seeing (≥ 1 arcsec) slightly larger than the average value.

Subaru raw images were processed using the SDFRED data pipeline (Ouchi et al., 2004) that yields standard flat field corrected images for each of the three filters. Photometric point source catalogues were extracted using standard `IRAF/Daophot` aperture photometry routines. We summarise here the main steps of the data reduction and we refer to Section 3 of Blom et al. (2011) for a detailed description of the method.

We obtain a raw list of object positions by running `IRAF/Daofind` on galaxy subtracted images in order to optimise the finding algorithm. The extraction threshold was typically set between 2 and 4 times the background depending on the filter and on the seeing conditions. The galaxy light was modelled with `IRAF/Ellipse` set to allow the position angle and ellipticity to vary. Next, we perform aperture photometry using `IRAF/Phot` on the preselected objects for a certain number of circular apertures from 1 up to 15 pixels (equivalent to ~ 0.2 arcsec to 3 arcsec for the Suprime-Cam pixel scale). The extraction radius was chosen in order to maximise the signal of the source and minimise the sky contribution. The extracted magnitude was corrected for the computed aperture correction using `IRAF/Mkapfile`. Photometric zeropoints were estimated by boot-strapping the Suprime-Cam photometry to the Sloan Digital Sky Survey (SDSS) DR7 photometric system (Abazajian et al., 2009) using the brightest objects in common between the two datasets (typically with $17 < i < 21$). If not in SDSS, the zeropoints were calibrated using the flux

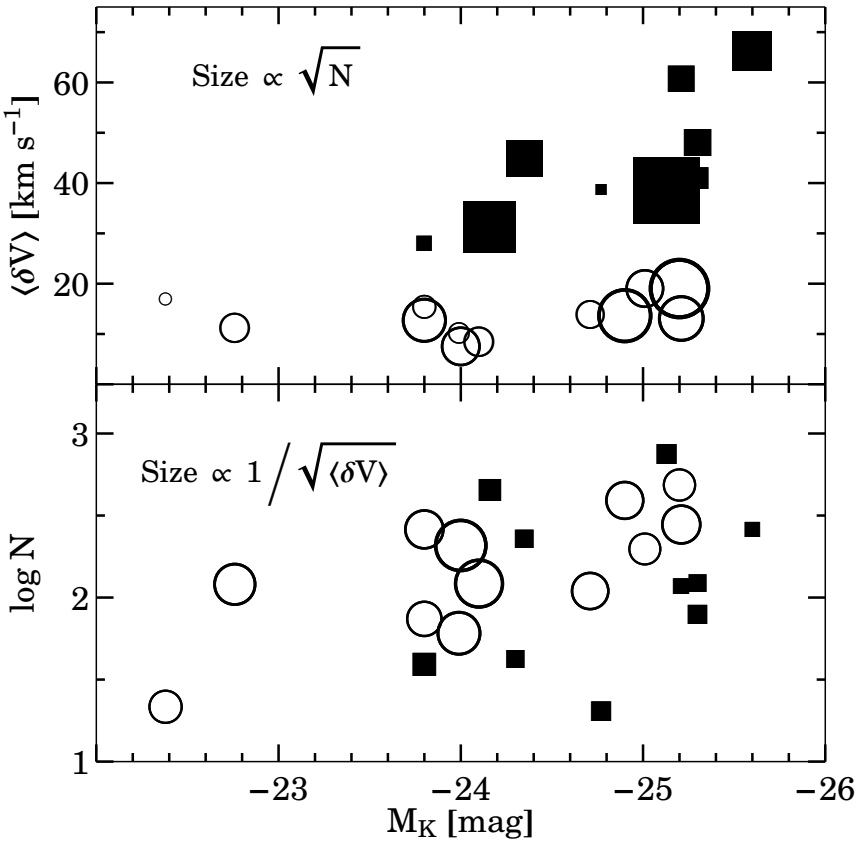

Figure 2.2 Accuracy of GC radial velocity measurements. Open circles and open boxes represent our GC data and literature data, respectively. Literature data will be discussed in Section 2.8. *Top panel*. The median velocity uncertainty $\langle \delta V \rangle$ per GC system are shown as a function of absolute magnitude in the K band. Symbol sizes are $\propto \sqrt{N}$, where N is the number of spectroscopically confirmed GCs per galaxy. *Bottom panel*. Log N is shown as a function of the absolute magnitude in the K band, where symbol sizes are $\propto 1/\sqrt{\langle \delta V \rangle}$. Our data extend the range of galaxy luminosity probed with three times better velocity accuracy.

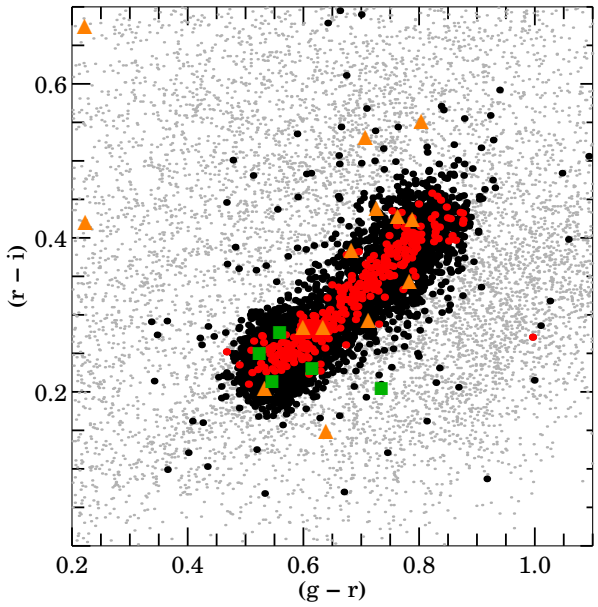

Figure 2.3 Colour-colour diagram of objects around NGC 1407. Grey and black points represent all the sources detected in the Suprime-Cam field of view and all the photometrically selected GCs with $i < 25$ and $i < 24$, respectively. Spectroscopically confirmed sources are shown as red points (GCs), green boxes (Galactic stars) and orange triangles (galaxies) respectively.

from standard stars observed over the same night. Finally, we use the reddening given in Table 2.1 and the conversion table of Schlegel et al. (1998) to derive the Galactic extinction correction in our photometric bands. Hereafter, all magnitudes and colours are extinction corrected.

2.3.2 HST data

We use *Hubble Space Telescope (HST)* archive images from the Advanced Camera for Surveys (ACS) and Wide Field Planetary Camera 2 (WFPC2) to improve the quality of the photometric selection in the central regions of our galaxies. For most of them, we exploit existing photometric GC catalogues and we refer to the following authors for a detailed description of the data reduction and analysis: Spitler et al. (2008) for NGC 821, Forbes et al. (2006) for NGC 1407 and NGC 1400, Forbes et al. (1996a) for NGC 5846, Chomiuk et al. (2008) for NGC 7457 and Blom et al. (2011) for NGC 4365.

We obtained, from the Hubble Legacy Archive, new *HST*/ACS imaging for NGC 3377, NGC 2768 and NGC 4278, respectively. The ACS camera has a pixel scale of 0.05 arcsec and a field of view of 3.36×3.36 arcmin^2.

The NGC 3377 imaging consists of one pointing in F475W ($\sim$ Sloan g) and F850LP ($\sim$ Sloan z) filters and it was observed as part of the *HST* project ID 10554. NGC 2768 (ID 9353)

Galaxy ID	Obs date	Filters	Exp. time [sec]	Seeing [arcsec]
NGC 0821	2008 Nov.	gri	$960, 350, 220$	$1.2, 1.0, 0.8$
NGC 1400	2008 Nov.	gri	$3240, 3600, 10800$	$0.6, 0.6, 0.6$
NGC 1407	2008 Nov.	gri	$3240, 3600, 10800$	$0.6, 0.6, 0.6$
NGC 2768	2005 Mar.	$R_{\rm C}iz$	$600, 100, 210$	$0.6, 0.6, 0.6$
NGC 3377	2008 Nov.	gri	$500, 450, 375$	$0.9, 0.7, 0.8$
NGC 4278	2002 Feb.	BVI	$600, 450, 360$	$1.4, 0.9, 0.9$
NGC 4365	2008 Apr.	gri	$650, 350, 300$	$0.8, 0.8, 0.8$
NGC 5846	2009 Apr.	gri	$2760, 1606, 1350$	$1.0, 0.6, 0.8$
NGC 7457	2009 Oct.	BVR	$6300, 6000, 7200$	$0.7, 0.8, 0.7$

Table 2.2 Summary of the ground-based imaging observations. The galaxy name, observation date, filters employed, together with the respective exposure time and seeing are listed. All the observations were performed using Subaru/Suprime-Cam, except for NGC 7457 observed with WIYN/MiniMo (Hargis et al., 2011).

was imaged in F435W, F555W, F814W filters, equivalent to a BVI configuration, respectively. Finally, the NGC 4278 (ID 10835) data consists of four pointings in F475W and F850LP filters that probe the galaxy up to ~ 6 arcmin from the centre (Usher et al. 2012, in preparation).

The *HST* imaging was reduced and analysed using a custom built pipeline to find point-like sources and measure their magnitudes and half light radii. For details on the methods used by the pipeline including point spread function determination, we refer to Strader et al. (2006) and to Spitler et al. (2006). The extracted magnitudes and sizes for GCs in NGC 3377 and NGC 4278 were compared with those published by Chies-Santos et al. (2011b) for objects in the NGC 3377 pointing and in the two NGC 4278 pointings. Both magnitudes and sizes show good agreement without any evidence of statistically significant offset from the published data.

2.3.3 Photometric GC selection

Once the point-source catalogues have been constructed, they are photometrically selected to avoid contamination, such as unresolved galaxies and Galactic stars. As far as our new Subaru data are concerned, this process involves the following steps: 1. selection in a colour-colour space; 2. selection in a colour-magnitude space; 3. a visual check. The GC selection in the ground-based imaging for NGC 7457 was carried out in Hargis et al. (2011) and we refer to this paper for a detailed description of their selection method. The steps listed above are subjected to variations in the procedures for the DEIMOS mask design.

GCs are known to populate a specific area of colour-colour diagrams (e.g., Rhode & Zepf, 2001; Faifer et al., 2011; Chies-Santos et al., 2011a). With a gri filter set, this is enclosed within $0.4 \lesssim (g-i) \lesssim 1.5, 0 \lesssim (r-i) \lesssim 0.6, 0.3 \lesssim (g-r) \lesssim 0.9$ where these boundaries run diagonally

to the colour axes, as shown in Figure 2.3 for the galaxy NGC 1407. To take into account the dependence of the colour boundaries on the quality of the data, we flag as GC candidates all the objects deviating by less than 2σ from these boundaries (Spitler et al., 2008).

Next, we apply a cut on the i band magnitude (I band for NGC 4278). Given the ongoing debate regarding the uncertain separation between GCs and ultra compact dwarfs (UCDs, Mieske et al., 2006; Brodie et al., 2011), we decided to set the upper brightness magnitude at $M_i \approx -11.6$ ($M_I \approx -12$), one magnitude brighter than the integrated magnitude of ω Cen, the brightest GC in the Milky Way. Nevertheless, in some cases we relax this criterion in order to include spectroscopically confirmed GCs that have magnitudes brighter than the set threshold. The separation between NGC 1407 and NGC 1400 objects will be discussed in Section 2.5.

Next, we calculate the radius at which the number of GC candidates per unit area flattens out (see §2.3.5 for the method), that is an estimate of the radius at which the contribution of the contaminants (Galactic stars and background galaxies) becomes dominant. Therefore, we count out of the GC selection all the objects outside this background radius. We have tested that the effect of the contaminants on the GC colour distribution is minimal (< 0.1) mag and that it does not affect considerably the GC colour bimodality (see also, Arnold et al., 2011).

Finally, we perform a visual check to make sure that no outliers, such as extended sources or image artefacts, contaminate the final GC catalogue. Most of the outliers turned out to be close to the galaxy (within 1 arcmin) where the galaxy light contamination and the crowded field makes the Subaru photometry unreliable. Within this radius, the contribution of the *HST* imaging becomes crucial.

As far as the *HST*/ACS imaging is concerned, it is worth noting that the diffraction limited quality of *HST* imaging has the advantage of making extragalactic GCs partially resolved for all of our galaxies. Therefore, the GC selection in our space-based imaging is also based on a size selection in addition to magnitude and colour-colour criteria (if available). In NGC 3377 and NGC 4278, for which only g and z imaging are available, we flag as GC candidates all the objects with colour $0.7 < (g - z) < 1.6$ and sizes $0.1 < r_h < 20$ pc. Such a choice is motivated by the clear drop off in the density of the objects outside the adopted colour cut, as observed in Blom et al. (2011). For NGC 2768, we adopt the same size-cut as above and select objects within $0.4 < (B - V) < 1.2$ and $0.8 < (V - I) < 1.4$ and an upper magnitude of $M_I \approx -12$. In Figure 2.4, the colour-magnitude diagrams of the GC candidates and of the spectroscopically confirmed GCs are shown.

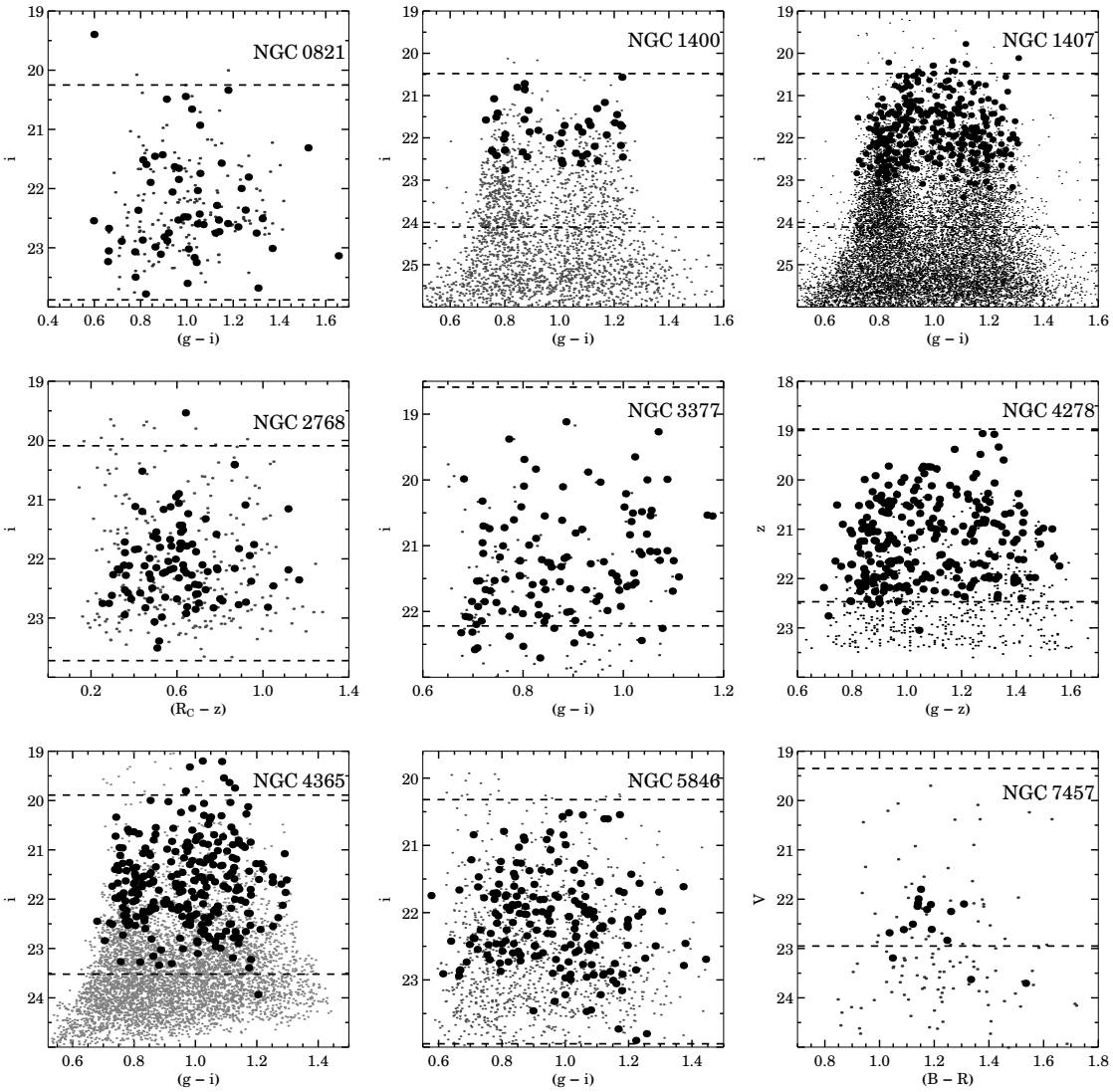

Figure 2.4 GC system colour-magnitude diagrams. Photometrically selected GCs and spectroscopically confirmed GCs are shown as small and large black points respectively. Upper and bottom dashed lines represent the ω Cen magnitude ($M_i \approx -11.6$) and the GC turnover magnitude ($M_{\rm TOM,i} \equiv -8$ mag) at the distances given in Table 2.1.

Galaxy ID	$\mu_{\rm blue}$	$\mu_{\rm red}$	$\sigma_{\rm red}$	$\sigma_{\rm red}$	p-value	dividing colour
NGC 0821	0.84	1.10	0.09	0.15	0.034	$(g-i)=1$
NGC 1400	0.79	1.05	0.05	0.11	10^{-10}	$(g-i)=0.98$
NGC 1407	0.85	0.77	0.05	0.1	10^{-10}	$(g-i)=0.98$
NGC 2768	0.41	1.10	0.15	0.22	10^{-5}	$(R_C-z)=0.57$
NGC 3377	0.73	0.93	0.05	0.08	10^{-6}	$(g-i)=0.88$
NGC 4278	0.93	1.31	0.10	0.16	10^{-10}	$(g-z)=1.1$
NGC 4365	0.78	1.04	0.05	0.13	10^{-10}	$(g-i)=0.91$
NGC 5846	0.74	1.00	0.15	0.06	10^{-5}	$(g-i)=0.95$
NGC 7457	1.12	1.36	0.13	0.17	0.311	$(B-R)$

Table 2.3 KMM results. For each galaxy, $\mu_{\rm blue}$ and $\mu_{\rm red}$ represent the mean of the blue and red peak respectively, whereas $\sigma_{\rm blue}$ and $\sigma_{\rm red}$ are the Gaussian σ for each peak. The second to last column gives the p-value, that is the confidence level with which the hypothesis of an unimodal colour distribution can be rejected (larger confidence for smaller p-values). The last column gives the colour used to divide the GC system into blue and red subpopulations. NGC 7457 is the only galaxy without significant bimodality detected.

2.3.4 GC colour bimodality

To probe bimodality, we use a Kaye's Mixture Model algorithm (KMM, Ashman et al. 1994) that returns colour peaks, variance and number of objects in the detected subpopulations. KMM was run on all the $(g-i)$ distributions of the Subaru GC candidates brighter than the turnover magnitude $M_{\rm TOM}$. In this work we adopt $M_{\rm TOM,i} \equiv 8.00 \pm 0.03$, derived using the $i-I$ transformation from Faifer et al. (2011) to calibrate the I band TOM given by Kundu & Whitmore (2001) into our photometric system.

For NGC 2768, NGC 7457 and NGC 4278, we study the $(R_{\rm C}-z)$, $(B-V)$ and $(g-z)$ colour distributions respectively. We perform a bisector fit (Feigelson & Babu, 1992) to the bright GCs in common between the *HST* and Subaru images, in order to convert *HST* magnitudes of the spectroscopically confirmed GCs into the respective Subaru photometric system. For NGC 4278, given the wide spatial coverage and better quality of its *HST* data, we transform Subaru magnitudes of the confirmed GCs into the *HST* photometric system. Results of the KMM analysis are presented in Table 2.3. We find that eight out of nine galaxies show significant GC colour bimodality. GCs are divided into blue and red according to the local minimum of the best fit Gaussians in Figure 2.5.

2.3.5 GC spatial distribution

We construct projected surface density profiles for the GC subpopulations of our galaxy sample. GC candidates brighter than the turnover magnitude were binned in circular annuli and corrected for areal incompleteness. The Subaru dataset was supplemented with *HST* photometry, in order to

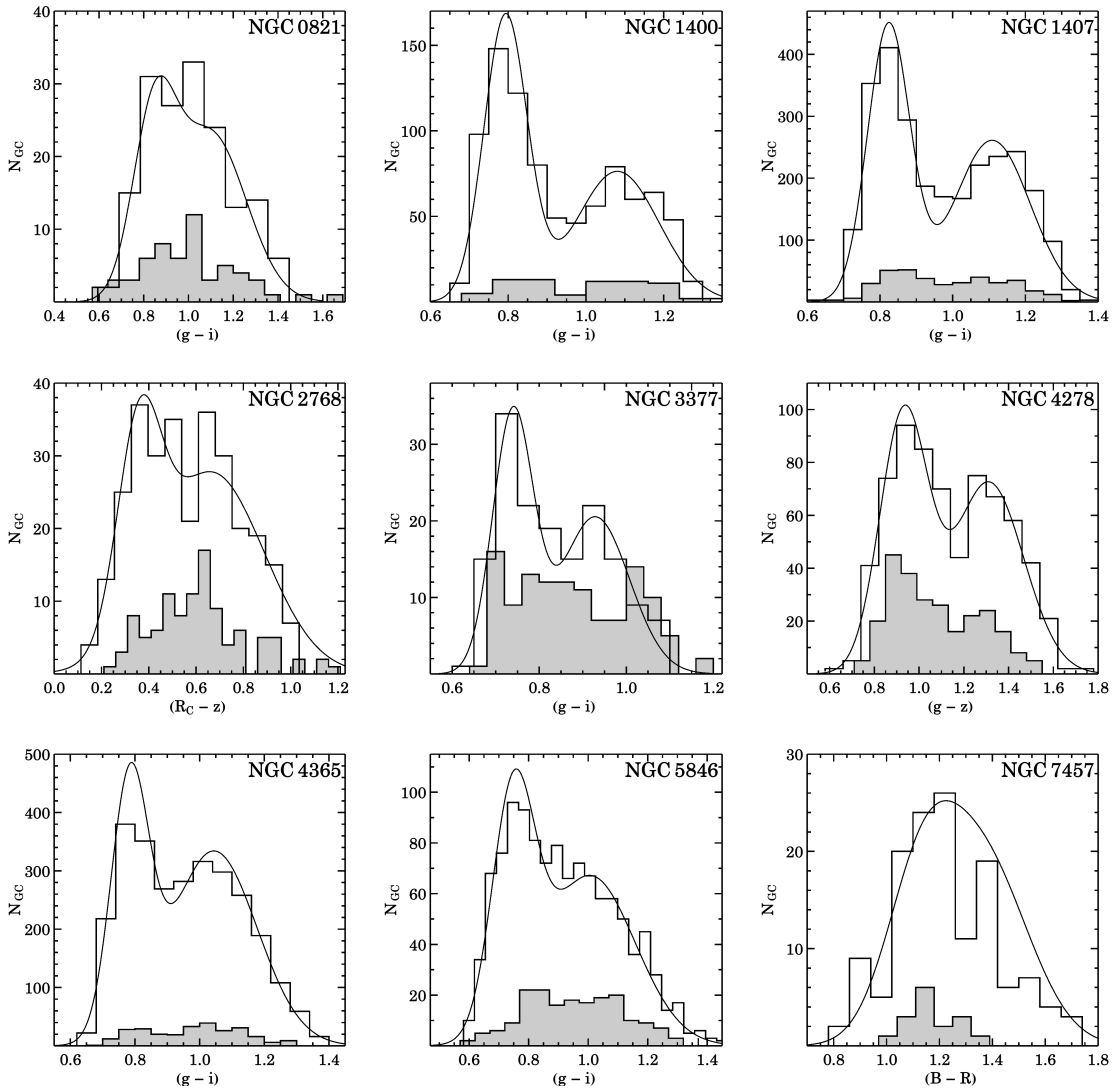

Figure 2.5 Colour histograms of our galaxy sample. GC candidates and spectroscopically confirmed GCs are shown as empty and grey filled histograms respectively. For NGC 1407, we only show GCs with $i < 23$. Solid lines show the sum of the KMM fits of the two subpopulations. No significant bimodality was detected in NGC 7457. The dearth of red GCs in NGC 3377 is due to the fact that we have excluded all the GC candidates within 1 arcmin from the centre. The magnitude of these objects turned out to be corrupted by the underlying diffuse stellar light.

probe the GC surface density in the inner regions. An important caveat to bear in mind is that we do not correct the Subaru dataset for magnitude incompleteness. This effect becomes important especially for objects fainter than $i \sim 23.5$ in the innermost regions ($\sim$ 1 arcmin) where the detection of sources is inhibited by the surface brightness contribution of the host galaxy (Faifer et al., 2011). Conversely, the completeness of the *HST* photometry in z (V) band is typically above 90 (70) per cent at the turnover magnitude even in the innermost regions, respectively (Larsen et al., 2001; Jordán et al., 2007). Therefore, we select all the GCs brighter than the turnover magnitude (see Figure 2.4) and we use circular radial bins in common between *HST* and Subaru to correct and adjust the Subaru GC surface density to that of the *HST* data. Although the matching between *HST* and Subaru data points is arbitrary, this approach preserves the relative slopes of the spatial distribution of the two subpopulations and allows us to verify whether or not blue and red GC subpopulations show different spatial distributions around the host galaxy as found from previous authors (e.g., Bassino et al., 2006).

Next, we fit the resulting (*HST* + Subaru) GC density profile $N(r)$ with a Sérsic law (Sérsic, 1963) similar to that commonly carried out for galaxy surface brightness profiles, but in practice we fit a variation of the Sérsic profile from Graham et al. (2005) in order to quantify the background level:

$$N(r) = N_e \exp\left(-b_n\left[\left(\frac{R}{R_{\rm eff}}\right)^{1/n} - 1\right]\right) + bg \tag{2.1}$$

where $b_n = 1.9992n - 0.3271$, n is the Sérsic index, $R_{\rm eff}$ is the effective radius of the GC system, N_e is the surface density at that radius and bg is the background contamination level. In case a Sérsic fit was not feasible due to small numbers we fit a power-law, i.e. $N(r) \propto r^{\alpha}$ that has been also used for similar analyses (Spitler et al., 2008). In Figure 2.6 the background subtracted GC surface density profiles for our galaxies are shown. As found in other galaxies, the red GCs are more centrally concentrated than the blue GCs (e.g., Geisler et al., 1996; Bassino et al., 2006; Faifer et al., 2011; Strader et al., 2011).

We also compare the GC surface density to the galaxy surface brightness for each galaxy, obtained from the Subaru images using `IRAF/Ellipse` as described in §2.3.1. The surface brightness profiles were corrected for the local galaxy ellipticity and then shifted by an arbitrary constant for comparison purposes (different for each galaxy). Figure 2.6 shows that, qualitatively, the slope of the red GC subpopulation agrees with that of the surface brightness of the host galaxy.

2.4 Spectroscopic observations and data analysis

Spectroscopic observations were performed with the DEep Imaging Multi-Object Spectrograph (DEIMOS, Faber et al. 2003) mounted on the 10 m Keck-II telescope. Galaxies were targeted

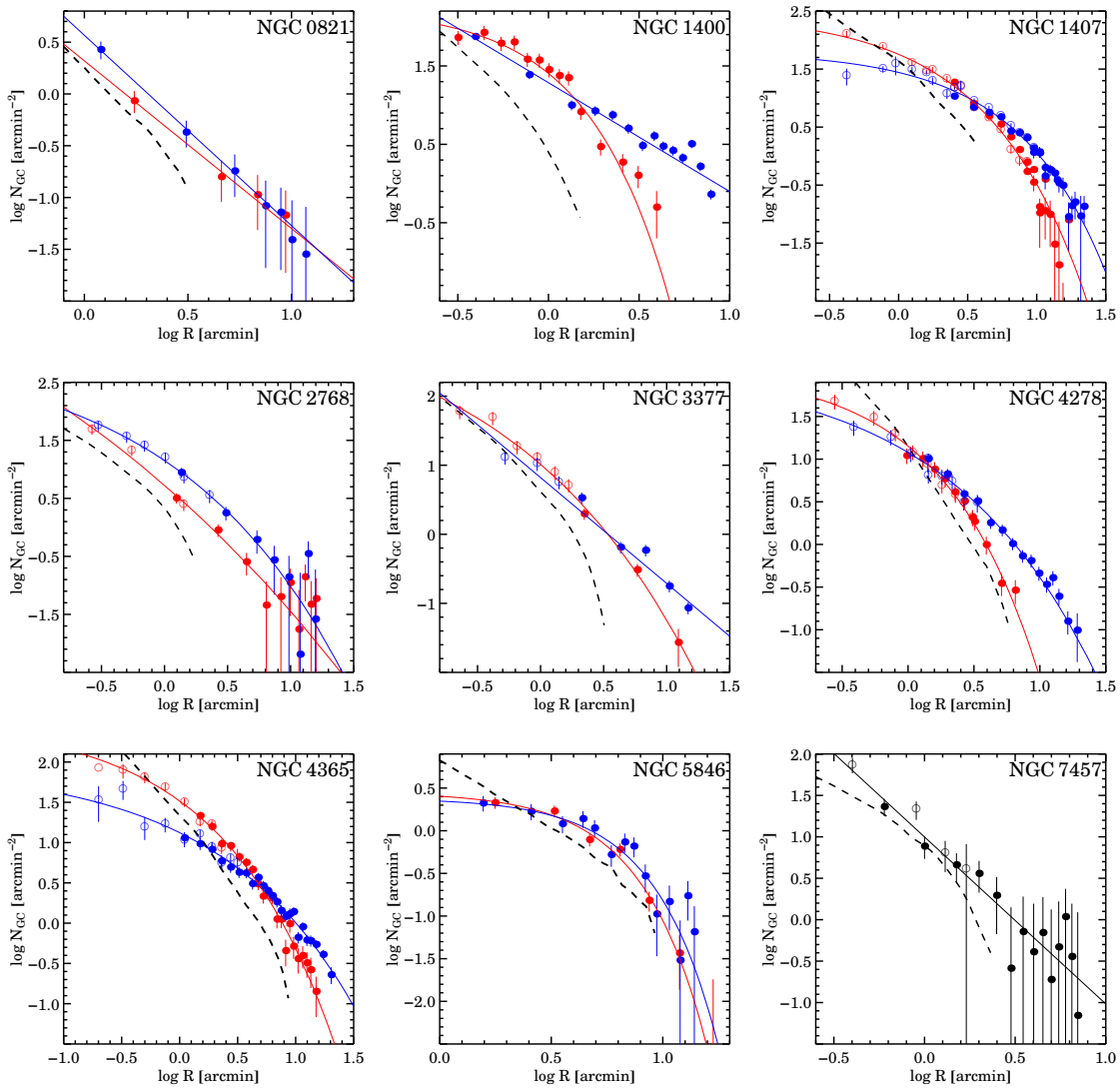

Figure 2.6 Surface density profiles of the GCs brighter than the turnover magnitude. Blue and red GC subpopulations are shown as blue and red filled points (if from Subaru imaging) and blue and red open circles (if from *HST* imaging) respectively. Sérsic fits or alternatively power-law fits to blue and red GC subpopulations are shown as blue and red lines respectively. For NGC 7457, the surface density and the fit to all GCs are shown as black points and black line respectively. Both the data points and the fits are background subtracted according to eq. 2.1. Also shown as dashed lines are the scaled and arbitrarily offset stellar surface brightness profiles obtained from Subaru imaging as described in §2.3.1 . For completeness, we also show the surface density profiles from Blom et al. (2011) for NGC 4365 and from Hargis et al. (2011) for NGC 7457, respectively.

Galaxy ID	Masks	Exp. time [hr]	N_{GCs}	N_{stars}	N_{gal}
NGC 0821	6	9.2	61	10	4
NGC 1400	4	9.0	72	6	27
NGC 1407	9	20	369	5	14
NGC 2768	5	12.7	109	57	9
NGC 3377	4	8.3	126	16	74
NGC 4278	4	8.8	256	44	33
NGC 4365	6	9.0	269	6	49
NGC 5846	6	9.1	195	32	4
NGC 7457	2	4.2	21	14	4
NGC 3115	5	14	190	29	0
NGC 4486	5	5.0	737	116	27
NGC 4494	5	4.6	117	34	108

Table 2.4 Summary of the spectroscopic observations for our twelve galaxies. The table lists the galaxy name and the total number of the DEIMOS masks used. To take into account the different seeing conditions over different nights, we show the total effective exposure time weighted by the mean seeing conditions during the observation time as done in Coccato et al. (2009). Also shown are the total number of spectroscopically confirmed GCs (including marginal GCs), Galactic stars and background galaxies respectively. The datasets for NGC 3115 and NGC 4486 also include GCs from external datasets as described in Arnold et al. (2011) and Strader et al. (2011) respectively.

in the period between 2006 and 2011, employing a different number of masks for each galaxy depending on the richness of the GC system. Objects selected for spectroscopic follow-up were chosen according to their likelihood of being GCs, i.e. giving priority to the objects selected with methods as Section 2.3.3. The spectroscopic observations are summarized in Table 2.4.

The large collecting area of the 10-meter Keck primary mirror combined with the $\sim 16 \times 5$ arcmin^2 of DEIMOS is the ideal combination to investigate the outskirts of galaxies where GCs are expected to be one of the best tracers of the total galaxy potential. For all the galaxies, DEIMOS was set up with the 1200 l/m grating centred on 7800 Å together with 1 arcsec wide slits, allowing coverage of the region between ~ 6500 – 8700 Å with a resolution of $\Delta\lambda \sim 1.5$ Å. Raw spectra were reduced using the DEIMOS/spec2d reduction pipeline provided online, that produces calibrated and sky subtracted spectra for each slit (Newman et al., 2012; Cooper et al., 2012).

We estimate the radial velocity of the GCs by measuring the Doppler shift of Calcium Triplet (CaT) absorption lines that characterises the infrared part of their spectra at 8498 Å, 8542 Å, 8662 Å, respectively. We measure radial velocities with `IRAF/Fxcor` that performs a cross-correlation between the Fourier transformed science spectrum and 13 template Galactic star Fourier transformed spectra. The template spectra were observed with the same DEIMOS setup used for scientific spectra and they cover a wide range of spectral type, luminosity and metallicity (from F

to M type). Fxcor was configured to have all the science and template spectra in the same wavelength range from 8300 to 8900 Å with the same DEIMOS spectral resolution. The radial velocity for each object was estimated as the mean of the radial velocity resulting from the correlation with each template star. The respective errors were evaluated by adding in quadrature the default error given by fxcor as described in Tonry & Davis (1979) to the standard deviation among the stellar templates, which is an estimate of the systematics.

2.4.1 Kinematic selection criteria

Once the final radial velocities of the GC candidates are obtained, we redshift-correct the spectra and perform a visual check to verify that the CaT lines are real and that they lie at the expected rest wavelength. Our selection criteria require the presence of at least two "visible" CaT lines (typically the brightest 8542 Å and 8662 Å lines) and of the Hα absorption line at 6563 Å, if probed in the redshift corrected spectra. The visual analysis is performed by at least two members of the team and it produces a final spectroscopic consensus catalogue. Spectra that show a radial velocity consistent with a GC, but for which it was not possible to reach a consensus, were flagged as "marginal" and are not included in the kinematic analysis. These objects have usually low signal-to-noise spectra or suffer from bad sky-line subtraction making the line identification subjective.

Besides background galaxies that can be usually spotted by the emission lines in their spectra, the main outliers of our spectroscopic selection are Galactic stars because they show a stellar spectrum with radial velocity $V_{\rm rad} \approx 0 \pm 500\,{\rm km\,s^{-1}}$. In most cases GCs and Galactic stars are well-separated in velocity, but for galaxies with $V_{\rm sys} < 1000\,{\rm km\,s^{-1}}$ Galactic stars might introduce a low velocity tail in the observed GC candidate velocity distribution. We decided to use a friendless algorithm introduced in Merrett et al. (2003) that flags objects deviating by more than $n \times \sigma$ from the velocity distribution of their N nearest neighbours. We use $n = 3$ and $10 < N < 20$ (depending on the galaxy) to exclude both stars and possible outliers that lie outside the 3σ envelope from the kinematic analysis.

In Figure 2.7 we show the distribution of all the spectroscopically confirmed GCs and Galactic stars in a radius-velocity phase space. In this plot and hereafter, galactocentric distances are expressed as a equivalent radius, that is defined as:

$$R = \sqrt{qX^2 + \frac{Y^2}{q}}, \tag{2.2}$$

where q is the axis ratio defined as the ratio of minor over the major axis of the galaxy (see Table 2.1), X and Y are Cartesian coordinates of an object in the galaxy rest frame, with the origin at the galaxy centre, and with X and Y aligned along the photometric major axis and minor axis

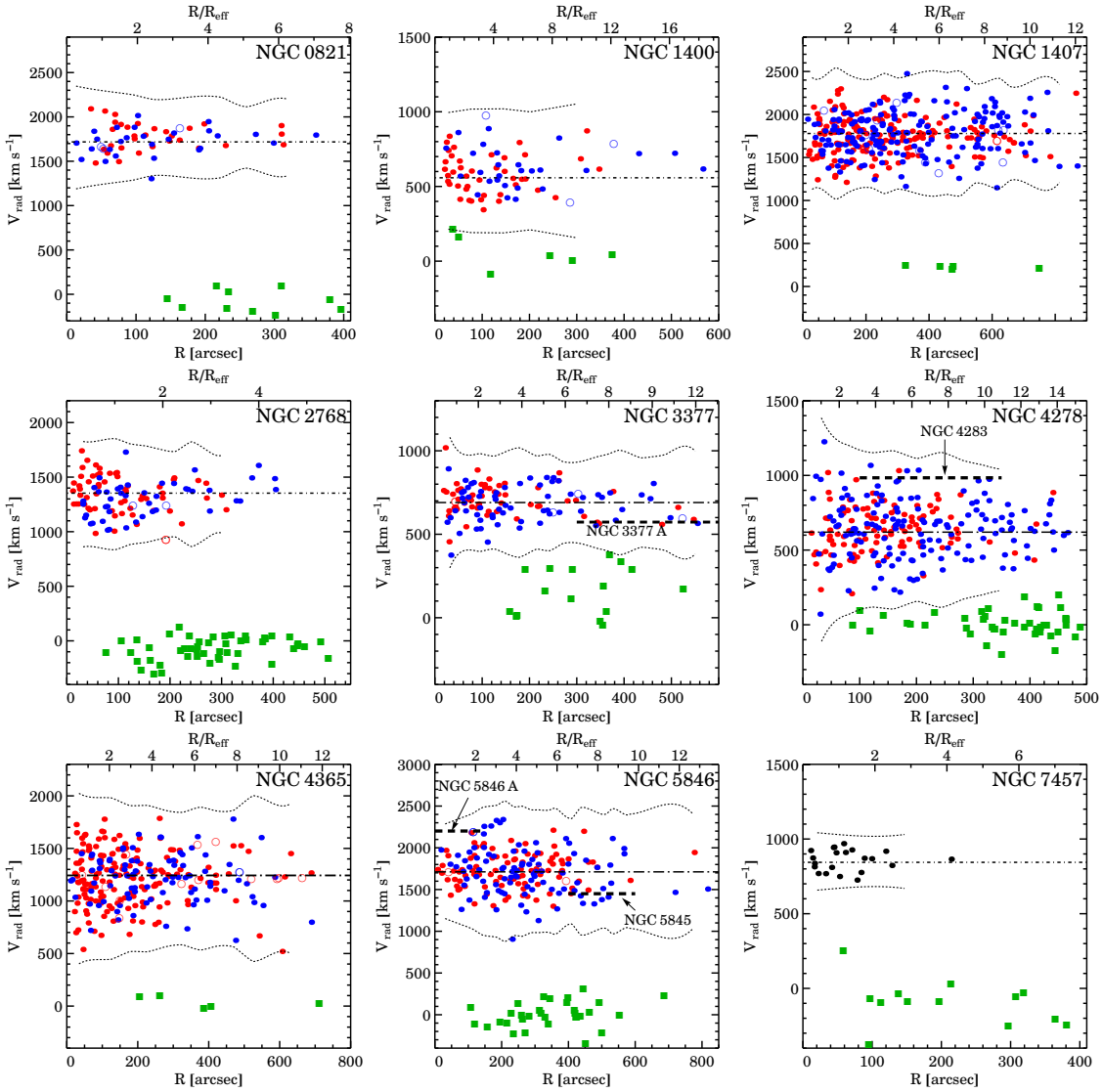

Figure 2.7 GC radial velocity distributions with galactocentric radius. Confirmed GCs, marginal GCs and Galactic stars are shown as filled points, open points and green boxes respectively. GCs are colour coded according to their subpopulation (blue or red) membership. Galactocentric radii have been translated into effective radii on the top axis. Dotted curves and dot-dashed lines are 3σ envelopes and the galaxy systemic velocities from Table 2.1, respectively. Also shown as thick dotted lines are the systemic velocities of the galaxies that might contaminate the GC system of the target galaxy. GCs have a mean velocity similar to the galaxy systemic velocity.

respectively. The final spectro-photometric catalogues of our galaxy sample are available on-line and they include spectroscopically confirmed GCs, "marginal" GCs, Galactic stars and galaxies.

2.4.2 Repeated GC measurements

We searched through the literature for GCs observed in our surveyed galaxies, finding existing datasets for three galaxies. In summary, we have re-observed: 1. 6 GCs of the 26 GCs confirmed by Puzia et al. (2004) in NGC 5846 using VLT/FORS2; 2. 7 GCs of the 13 GCs found by Chomiuk et al. (2008) in NGC 7457 using Keck/LRIS ; 3. 24 GCs of the 33 GCs resulting from the combination of the Brodie et al. (2005) and Larsen et al. (2003) catalogues of NGC 4365, both observed with Keck/LRIS.

In Figure 2.8 we compare our DEIMOS dataset with literature studies. There is a rough agreement between external datasets and our DEIMOS radial velocities, although the root-mean-square of the velocity difference between the two datasets is larger than what was found with DEIMOS repeated measurements.

We supplement our GC catalogues with external GC radial velocities corrected for the mean offset between the literature and our DEIMOS measurements. This offset is $-15\,\mathrm{km\ s^{-1}}$ for both NGC 7457 and NGC 5846. In NGC 4365, the offset between DEIMOS radial velocities and Larsen et al. (2003) is effectively zero, and we only correct the dataset of Brodie et al. (2005) by $-41\,\mathrm{km\ s^{-1}}$.

We test the reliability of our spectroscopic measurements by comparing the radial velocity of two or three GCs observed over different nights. Overall, we have collected 118 repeated GC radial velocities and these are shown in Figure 2.9. One-third of the total repeated sample is from a NGC 2768 mask that was observed twice with a one night offset. We find that repeated GC measurements are in good agreement in all the galaxies. The root-mean-square (rms) of the velocity difference between two observations is $\delta V_{\mathrm{rms}} = 15 \pm 1\,\mathrm{km\ s^{-1}}$.

2.4.3 Kinematic analysis

We study the kinematic properties of our GC systems using a maximum likelihood approach. We summarize here the main points of this analysis and refer to Foster et al. (2011) for the details. We divide the data in radial bins and then we fit the amplitude of the rotation (V_{rot}), the velocity dispersion (σ) and the kinematic position angle (PA_{kin}) simultaneously. The bin size varies from galaxy to galaxy (wider for larger datasets) and it was set to have roughly the same number of

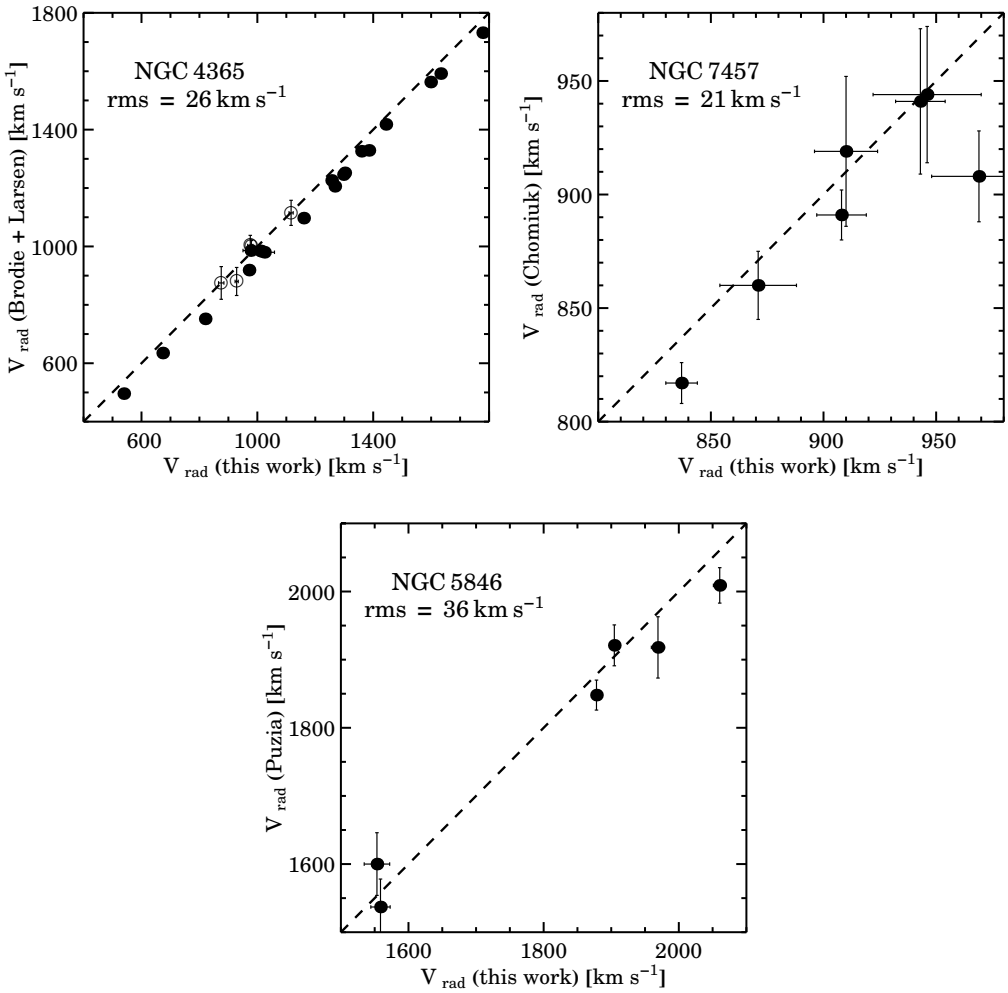

Figure 2.8 Comparison of our GC radial velocities with previous studies. For each galaxy the root-mean-square of the velocity difference between the two samples is also shown. Literature datasets come from Brodie et al. (2005) (black points) and Larsen et al. (2003) (open circles) for NGC 4365; Chomiuk et al. (2008) for NGC 7457; Puzia et al. (2004) for NGC 5846. The one-to-one line is shown as a dashed line.

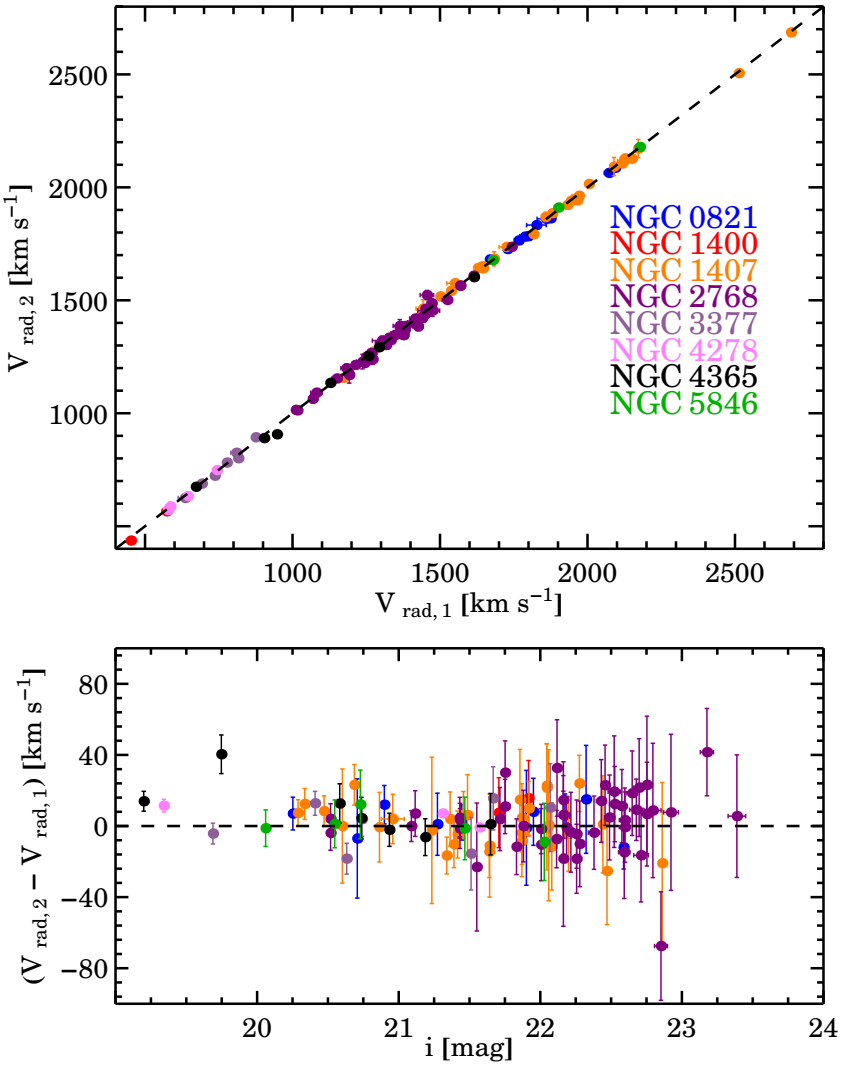

Figure 2.9 Repeated GC radial velocity measurements. In the *top panel* we show the radial velocity of a GC $V_{\rm rad,1}$ against the radial velocity of the same GC observed in a different night $V_{\rm rad,2}$. Data points are colour coded according their host galaxy membership listed on the right. The dotted line is a one-to-one line. In the *bottom panel* we show the difference $V_{\rm rad,1} - V_{\rm rad,2}$ as a function of the i band magnitude of the object. The dotted line shows the constant $V_{\rm rad,2} - V_{\rm rad,1} = 0$ to guide the eye. Radial velocities from different nights are in good agreement with each other, with an overall root-mean-square (rms) of $15 \pm 1\,{\rm km\ s^{-1}}$. No significant trend is seen as a function of GC magnitude.

objects per bin. For the $j^{\rm th}$ radial bin we minimise the χ^2 function:

$$\chi^2_j \propto \sum_{i=1}^{i=N_j} \left[\frac{(V_{{\rm rad},i} - V_{{\rm mod},i,j})^2}{(\sigma_j^2 + (\Delta V_{{\rm rad},i})^2)} + \ln(\sigma_j^2 + (\Delta V_{{\rm rad},i})^2) \right], \tag{2.3}$$

where:

$$V_{{\rm mod},i,j} = V_{\rm sys} \pm \frac{V_{{\rm rot},j}}{\sqrt{1 + \left(\frac{\tan(PA_i - PA_{{\rm kin},j})}{q_{{\rm kin},j}} \right)^2}}. \tag{2.4}$$

In eq. 2.4, PA_i, $V_{{\rm obs},i}$ and $\Delta V_{{\rm obs},i}$ are the position angle, recession velocity and uncertainty on the recession velocity for the $i^{\rm th}$ GC, respectively. The axis ratio of GC systems is challenging to derive directly because of low number statistics, but it has been constrained in galaxies with large photometric datasets (Kissler-Patig et al. 1997, Strader et al. 2011, Blom et al. 2011). Therefore, the kinematic axis ratio $q_{\rm kin}$ of the GC system was assumed to be equal to the respective photometric axis ratio of the galaxy light (see Table 2.1). The galaxy systemic velocity $V_{\rm sys}$ was fixed to the values given in Table 2.1 because the GC mean velocity is in good agreement with the galaxy systemic velocity itself. Uncertainties on the fits to the GC kinematics are obtained using a bootstrapping method similar to that used by Côté et al. (2001). We obtain 1000 "mock" GC kinematic samples for each galaxy, by sampling with replacement from our measured distribution. This kind of kinematic modelling tends to overestimate the rotation amplitude when the kinematic position angle is a free parameter. By way of example, the best fit to eq. 2.4 for the GCs in NGC 3377 and its kinematic dataset are shown in Figure 2.10 and Table 2.5, respectively. Moreover, Table 2.6 lists the important kinematic quantities for all our twelve galaxies.

The kinematic method described above was used to investigate the kinematic properties of our surveyed galaxies in two different ways:

- First, the kinematic properties of each GC system were calculated as a function of the galactocentric radius. This approach allows us to compare the kinematics of a given GC system to different kinematic probes (e.g., long-slit spectroscopy and/or PNe kinematics). We generally use between 20 and 30 GCs per bin depending on the galaxy. These results are shown in Figure 2.11.

- Secondly, the confirmed GCs were sorted by their colour to study the GC kinematics as a function of colour. Here we use moving colour bins of equal width (with usually 20 GCs per bin) to investigate the effect of each GC on the final fit. This analysis is independent of the photometric dividing colour and it has the advantage of testing whether or not there is a transition in the kinematics between the two subpopulations. These results are shown in Figure 2.12.

To better appreciate the global kinematic properties of our GC systems, we also construct a 2D smoothed velocity field for our elongated early-type galaxies (i.e., galaxies with $(b/a)_K < 0.6$: NGC 821, NGC 2768, NGC 3377, NGC 7457). These galaxies are all part of the ATLAS^{3D} sample (Krajnović et al., 2011) and are indeed good candidates to compare their moderate–fast stellar rotation in the innermost regions with the kinematics of their GC system. For each of the four galaxies, we will consider only the subpopulation with non-zero rotation, which is the red GC subpopulation for NGC 3377 and NGC 2768, the blue GCs for NGC 821 and all GCs for NGC 7457, respectively. At every position (x, y) on the sky we compute the local radial velocity $\hat{v}(x, y)$ via interpolation of the weighted average radial velocities of the N nearest neighbours, similar to the technique used in Coccato et al. (2009):

$$\hat{v}(x,y) = \frac{\sum_{i=1}^{N} V_{\rm rad,i}/d_i^2}{\sum_{i=1}^{N} 1/d_i^2} \tag{2.5}$$

with the weights being the reciprocal of the square distance d between two neighbour GCs. The 2D velocity field was smoothed using a Gaussian filter kernel of variable width for each galaxy on a regularly spaced grid. The kernel size was arbitrarily set between 2 and 5 kpc depending the sampling of the GC system and on the size of the galaxy. For the sake of comparison, we analysed the SAURON data-cubes (Emsellem et al., 2007) of the same four early-type ellipticals in order to reproduce their 2D stellar velocity fields using our technique. These results are shown in Figure 2.13.

We also compute the root-mean-square velocity:

$$V_{\rm rms}^2 = \frac{1}{N}\sum_{i=1}^{N}(V_{\rm rad,i} - V_{\rm sys})^2 - (\Delta V_{\rm rad,i})^2. \tag{2.6}$$

This quantity coincides with the velocity dispersion in eq. 2.4 if the contribution of the rotation is negligible. The uncertainty on the $V_{\rm rms}$ is estimated with the formulae provided by Danese et al. (1980).

A final caveat to bear in mind concerns the different kinematic axes convention. Based on the fit of the GC radial velocities with the position angle (Figure 2.10), we define the kinematic position angle as the angle between the direction of maximum rotation amplitude and North, that is 90 degrees away from the angular momentum vector. Some previous studies have instead defined the kinematic position angle as the direction around which the rotation is occurring. In other words, our kinematic major axis would correspond to the kinematic minor axes quoted by Lee et al. (2010b). Our convention is in line with that used in other galaxy kinematic studies (e.g. ATLAS^{3D}). For the galaxy properties of the literature sample we use the same sources quoted in

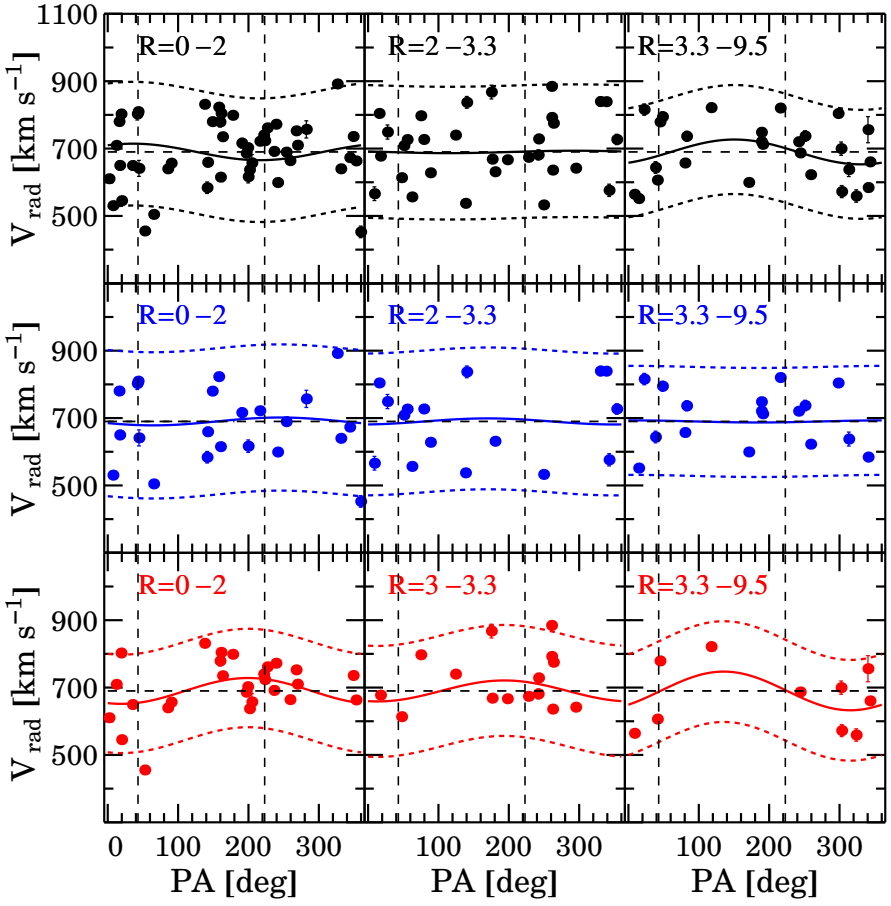

Figure 2.10 Rotation of NGC 3377 GC system with position angle in different radial bins. From the top to the bottom, panels show the rotation for all, blue and red GC subpopulations respectively. Whereas from the left to the right, panels show the rotation in the radial bin reported on the top left for each panel. The photometric major axis and the systemic velocity of the galaxy are both from Table 2.1 and represented with dashed vertical and dashed horizontal lines respectively. The best fit to eq. 2.4 and $\pm 2\sigma$ envelope are shown as filled and dotted lines respectively.

Table 2.1.

ID	RA	Dec	V_{rad}	δV_{rad}	g	δg	r	δr	i	δi
	[Degree]	[Degree]	[km s^{-1}]	[km s^{-1}]	[mag]	[mag]	[mag]	[mag]	[mag]	[mag]
(1)	(2)	(3)	(4)	(5)	(6)	(7)	(8)	(9)	(10)	(11)
NGC3377_GC1	161.94713	14.00741	810	8	21.387	0.019	20.855	0.013	20.606	0.014
NGC3377_GC2	161.90719	13.96616	724	10	22.295	0.032	21.588	0.021	21.223	0.021
NGC3377_GC3	161.89561	13.97022	729	13	22.596	0.032	21.962	0.021	21.671	0.021
NGC3377_GC4	161.92600	14.01391	453	17	22.610	0.034	22.048	0.023	21.864	0.025
NGC3377_GC5	161.89744	13.97086	681	14	22.789	0.037	22.037	0.023	21.691	0.022
NGC3377_GC6	161.93466	13.96388	779	15	22.546	0.034	21.948	0.023	21.653	0.025
NGC3377_GC7	161.91688	13.96030	617	18	22.919	0.046	22.286	0.031	22.073	0.036
NGC3377_GC8	161.88981	13.95709	754	5	20.002	0.009	19.411	0.006	19.116	0.005
NGC3377_GC9	161.94103	14.03665	804	6	20.150	0.009	19.632	0.006	19.378	0.006
NGC3377_GC10	161.87097	13.91145	820	7	20.895	0.013	20.305	0.008	20.094	0.008
...	...	...	...	...	...	...	...	...	...	...
NGC3377_star1	162.03633	14.02335	185	11	22.174	0.026	21.750	0.017	21.581	0.017
NGC3377_star2	161.86723	13.90198	289	18	22.547	0.003	20.090	0.020	21.887	0.002
...	...	...	...	...	...	...	...	...	...	...
NGC3377_gal1	161.83237	13.92902	–	–	22.250	0.025	21.595	0.015	21.370	0.015
NGC3377_gal2	161.95037	14.08945	–	–	24.188	0.069	24.214	0.062	24.290	0.087
...	...	...	...	...	...	...	...	...	...	...

Table 2.5 Spectro-photometric catalogue of objects around NGC 3377. The horizontal lines divide the sample into spectroscopically confirmed GCs, spectroscopically confirmed Galactic stars and background galaxies. The first column gives the object ID, composed of the galaxy name and the object identification. Columns 2 and 3 give position in right ascension and declination (J2000), respectively. Columns 4 and 5 are the observed heliocentric radial velocities and uncertainties respectively. The remaining columns are the Subaru photometry in *gri* and respective uncertainties. For the full table for all the surveyed galaxies see the on-line version of Pota et al. (2013).

2.4.4 Velocity-bias correction

A feature of the kinematic modelling used in this work (equation 2.4) is that the rotation amplitude is biased to higher values when the kinematic position angle is unconstrained. This effect becomes important in systems with $V_{\rm rot} \ll \sigma$, because the rotation (and its direction) is fully embedded in the dispersion. There are two ways to approach this issue: numerically, via a Monte Carlo simulation, or analytically, using the Box's bias measure in non-linear model theory (Box, 1971). The first method is the most straightforward, whereas the latter is computationally more complicated. Here we adopt a similar approach to Strader et al. (2011) and correct for the bias via a Monte Carlo simulation.

In practice, for each data bin containing N GCs (see Figure 2.11), we compute the best fit rotation by minimizing equation 2.3. We then generate 1000 artificial datasets, of the same size N, drawn from the best-fit model. We repeat the fit for each generated dataset using the original best-fit model as starting point. We define the velocity bias as the median difference between the computed and the simulated (known) rotation amplitude. This approach is adopted to correct for the bias also in Figure 2.12, Table 2.6 and Table 2.7.

We find that the magnitude of the bias correction depends both on the bin size and on the $(V_{\rm rot}/\sigma)$. In the case of $(V_{\rm rot}/\sigma) \gtrsim 1$, the bias is negligible regardless the bin size. For bins with $(V_{\rm rot}/\sigma) \sim 0.4\,(0.6)$ and $N \leq 20$, the bias can be up to $\sim 50\,(40)$ km s^{-1}. Within the same $(V_{\rm rot}/\sigma)$ values, the bias can decrease down to $\sim 30(20)$ km s^{-1} for $N \approx 50$. This agrees with the rule of the thumb of Strader et al. (2011) to identify the severity of the bias, i.e. the bias is small if $(V_{\rm rot}/\sigma) \geq 0.55 \times \sqrt{20/N}$. If this condition is satisfied, we find that the bias is of the order of (or less then) our nominal median uncertainty of 15 km s^{-1}.

2.5 Notes on individual galaxies

In this section we briefly discuss the kinematic results for our new nine GC systems that are presented in Figure 2.11, Figure 2.12 and Figure 2.13.

2.5.1 NGC 821

NGC 821 is an isolated E6 galaxy (de Vaucouleurs, 1991) with photometric and kinematic signatures of an edge-on stellar disk (Emsellem et al. 2007; Proctor et al. 2009). The dark matter content of this galaxy has been debated in the literature. Romanowsky et al. (2003), and recently Teodorescu et al. (2010) found that the velocity dispersion of the PNe decreases with radius. In contrast, Weijmans et al. (2009), Forestell & Gebhardt (2010) and Proctor et al. (2009) found a flat velocity dispersion for the stellar component within 100 arcsec. A photometric study of

the GC system of NGC 821 was carried out by Spitler et al. (2008) using wide-field WIYN and *HST* observations. They were able to detect significant colour bimodality only after combining ground-based and space-based observations.

Our Subaru observations suffer from moderate g band seeing (~ 1.2 arcsec). However, we detect significant GC colour bimodality, although the blue and the red peaks are not clearly visible. We confirm that the surface density profile of the GC system extends up to 4 arcmin, as suggested from the WIYN imaging.

The combination of the poor g band seeing, and the presence of the 10th magnitude star 2 arcmin from the galaxy centre, resulted in a low return rate of spectroscopically confirmed GCs. In total, we obtained radial velocities for 61 GCs over 6 DEIMOS masks. We adopt a colour split at $(g-i) = 1.0$. This value was used to analyse the kinematics of blue and red GC subpopulations separately.

We detect significant rotation only for the blue GCs and for a small group of red GCs. The blue GCs are found to rotate at ~ 85 km s^{-1} along $\mathrm{PA_{kin}} = 85^{+26}_{-27}$ deg, consistent with the photometric minor axis and in agreement with that found by Coccato et al. (2009) using PNe. Such a peculiarity is clearly visible in Figure 2.12. We will discuss this feature and its implications in more detail later. Interestingly, we note that the direction of the GC and PNe rotation coincides with an elongated jet/outflow structure detected in the X-ray (Pellegrini et al., 2007). With the adopted colour split, the kinematic position angle of the red GCs is generally unconstrained, except the outer red GCs that counter rotate with respect to the host galaxy stars. The velocity dispersion of both the red and the blue GCs declines with radius with a slope similar to that of the PNe and host galaxy stars.

Galaxy ID	$V_{\rm sys,GC}$ [km s^{-1}]	$V_{\rm rms,A}$ [km s^{-1}]	$V_{\rm rms,B}$ [km s^{-1}]	$V_{\rm rms,R}$ [km s^{-1}]	$(V_{\rm rot}/\sigma)_{\rm A}$	$(V_{\rm rot}/\sigma)_{\rm B}$	$(V_{\rm rot}/\sigma)_{\rm R}$	PA$_{\rm kin,A}$ [deg]	PA$_{\rm kin,B}$ [deg]	PA$_{\rm kin,R}$ [deg]
(1)	(2)	(3)	(4)	(5)	(6)	(7)	(8)	(9)	(10)	(11)
NGC 821	1750	158^{+17}_{-13}	145^{+28}_{-18}	154^{+26}_{-17}	$0.11^{+0.18}_{-0.18}$	$0.60^{+0.33}_{-0.30}$	$0.09^{+0.27}_{-0.22}$	80^{+183}_{-90}	85^{+26}_{-27}	252^{+94}_{-137}
NGC 1400	612	137^{+14}_{-11}	140^{+22}_{-15}	135^{+19}_{-14}	$0.07^{+0.17}_{-0.13}$	$0.10^{+0.25}_{-0.15}$	$0.54^{+0.27}_{-0.26}$	39^{+49}_{-48}	200^{+55}_{-60}	30^{+21}_{-20}
NGC 1407	1774	224^{+9}_{-8}	232^{+14}_{-12}	216^{+12}_{-11}	$0.17^{+0.07}_{-0.08}$	$0.03^{+0.10}_{-0.08}$	$0.32^{+0.10}_{-0.10}$	285^{+30}_{-29}	224^{+120}_{-101}	299^{+18}_{-19}
NGC 2768	1338	165^{+13}_{-11}	173^{+23}_{-17}	160^{+17}_{-13}	$0.39^{+0.13}_{-0.11}$	$0.34^{+0.21}_{-0.23}$	$0.43^{+0.15}_{-0.14}$	97^{+22}_{-24}	121^{+32}_{-34}	79^{+28}_{-27}
NGC 3377	685	100^{+7}_{-6}	100^{+12}_{-9}	85^{+10}_{-7}	$0.19^{+0.13}_{-0.14}$	$0.09^{+0.15}_{-0.14}$	$0.58^{+0.20}_{-0.20}$	197^{+40}_{-40}	275^{+77}_{-108}	181^{+21}_{-19}
NGC 4278	637	177^{+9}_{-7}	182^{+12}_{-10}	152^{+12}_{-10}	$0.17^{+0.08}_{-0.08}$	$0.16^{+0.11}_{-0.13}$	$0.25^{+0.15}_{-0.14}$	200^{+26}_{-26}	194^{+32}_{-38}	207^{+39}_{-42}
NGC 4365	1210	248^{+12}_{-10}	230^{+20}_{-16}	258^{+16}_{-13}	$0.11^{+0.09}_{-0.10}$	$0.17^{+0.18}_{-0.14}$	$0.26^{+0.11}_{-0.12}$	129^{+37}_{-42}	307^{+29}_{-40}	121^{+26}_{-26}
NGC 5846	1706	238^{+13}_{-11}	266^{+22}_{-18}	207^{+17}_{-14}	$0.02^{+0.15}_{-0.12}$	$0.19^{+0.14}_{-0.10}$	$0.12^{+0.14}_{-0.15}$	157^{+60}_{-79}	259^{+60}_{-71}	107^{+43}_{-56}
NGC 7457	847	68^{+12}_{-9}	–	–	$1.68^{+0.37}_{-0.40}$	–	–	324^{+10}_{-10}	–	–
NGC 3115	710	164^{+9}_{-8}	166^{+13}_{-11}	161^{+13}_{-10}	$0.66^{+0.09}_{-0.09}$	$0.74^{+0.12}_{-0.13}$	$0.61^{+0.14}_{-0.13}$	35^{+11}_{-12}	47^{+13}_{-13}	20^{+16}_{-17}
NGC 4486	1336	328^{+14}_{-12}	296^{+28}_{-22}	337^{+16}_{-14}	$0.07^{+0.05}_{-0.04}$	$0.09^{+0.07}_{-0.08}$	$0.29^{+0.17}_{-0.17}$	105^{+40}_{-38}	92^{+49}_{-48}	123^{+39}_{-43}
NGC 4494	1338	99^{+14}_{-12}	98^{+9}_{-7}	99^{+15}_{-11}	$0.60^{+0.12}_{-0.11}$	$0.65^{+0.15}_{-0.15}$	$0.43^{+0.21}_{-0.23}$	174^{+16}_{-17}	167^{+16}_{-1}	195^{+33}_{-31}

Table 2.6 GC kinematic results for our galaxy sample. Column (2) shows the systemic velocity of the host galaxy obtained from the weighted average of the GC radial velocities of the azimuthal-complete innermost region. The remaining columns are the overall root-mean-square velocity $V_{\rm rms}$, the rotational dominance parameter $(V_{\rm rot}/\sigma)$ and kinematic position angle PA for all, blue and red GC subpopulations respectively.

2.5.2 NGC 1400

NGC 1400 has been classified both as a face-on S0 (Jarrett et al., 2003) and as an E0 (e.g., da Costa et al. 1998). It is the second brightest galaxy in the Eridanus group after NGC 1407. We have assumed that NGC 1407 and NGC 1400 lie at the same distance of 26.8 Mpc. NGC 1400 is characterised by a uniformly old stellar age up to $\sim 1.3R_{\rm eff}$ (Spolaor et al., 2008b) and by an unusually low systemic velocity ($V_{\rm sys} = 558\,{\rm km\ s^{-1}}$) for its distance. Forbes et al. (2006) studied the GC system of this galaxy using Keck/LRIS in imaging mode, detecting significant bimodality.

The photometric GC selection was performed within 8 arcmin from the galaxy centre to minimise the contamination from NGC 1407 GC system, resulting in a clear bimodal distribution, with the colour separation occurring at $(g-i) = 0.98$. The GC surface density was corrected for the local NGC 1407 contribution. This galaxy shows the steepest red surface density profile among our galaxies, similar to the slope of the galaxy surface brightness. In contrast, the profile of the blue GC subpopulation is more radially extended and also requires a power-law fit, because a Sèrsic function does not return a satisfactory solution.

We present here radial velocities for 34 blue and 37 red GCs respectively, for a total of 71 spectroscopically confirmed GCs. Despite their small angular separation ($\sim$ 10 arcmin), NGC 1407 and NGC 1400 also have a large peculiar velocity difference (~ 1200 km s^{-1}), assuring a reliable separation of their spectroscopically confirmed GCs. The red GCs mimic the rotation of the stars in the inner regions, whereas the rotation of the blue GCs is consistent with zero with a marginal signature of counter-rotation in the inner radial bin. The velocity dispersion of the red GCs is in agreement with long–slit data in the region of overlap, with a slightly increasing trend towards the outer regions. Conversely, the velocity dispersion of the blue GCs decreased with the radius.

2.5.3 NGC 1407

NGC 1407 is a massive E0 galaxy at the centre of the dwarf galaxy dominated Eridanus A group (Brough et al., 2006). It shows moderate rotation along the photometric major axis and has a weak central AGN (Zhang et al., 2007). The stellar population analysis of Spolaor et al. (2008a) found the galaxy to possess a uniformly old age within $\sim 0.6R_{\rm eff}$. A dynamical analysis of NGC 1407 was given by Romanowsky et al. (2009). They used Suprime-Cam imaging and DEIMOS spectra for 172 GCs and found a massive dark halo.

In this work, we use the photometric results presented in Romanowsky et al. (2009) in which the Suprime-Cam imaging was reduced and analysed with the same methodology described in their paper. The colour distribution shows clear bimodality with the colour separation occurring at $(g-i) = 0.98$. We supplement the spectroscopic sample of Romanowsky et al. (2009) with 6 additional DEIMOS masks, that make NGC 1407, with a total of 369 spectroscopically confirmed

GCs, the most populous spectro-photometric dataset in our galaxy sample.

We detect rotation along the photometric major axis for both GC subpopulations. The blue GCs rotate in the innermost radial bin along the photometric minor axis and between 3 and 5 $R_{\rm eff}$ along the photometric major axis. Similarly, the rotation of the red GCs occurs along the photometric major axis directions, but in this case the rotation signal is generally larger and better constrained than that of the blue GCs. Both GC subpopulations appear to rotate in the outermost regions of the galaxy along the major axis of the galaxy. The velocity dispersion of the red GC subpopulation in the inner regions is consistent with stellar data from Spolaor et al. (2008b) and Proctor et al. (2009) showing a decreasing profile up to 10 $R_{\rm eff}$. Conversely, the velocity dispersion of the blue GCs increases with radius.

2.5.4 NGC 2768

NGC 2768 is classified as E6 in de Vaucouleurs (1991) and as $S0_{1/2}$ in Sandage & Bedke (1994). Spectroscopic studies of the very central regions (McDermid et al., 2006) have also suggested a young (2.5 Gyr) stellar population associated with the disk, as supported by the recent supernova SN2000ds (Filippenko & Chornock, 2000). Kundu & Whitmore (2001) studied the *HST*/WFPC2 photometry for 113 GC candidates in this galaxy, finding a statistically significant probability of it having a bimodal colour distribution.

In this work, NGC 2768 was imaged with $R_{\rm C}iz$ filters, in good seeing conditions but with the lowest exposure time among our sample of galaxies. Using KMM we found the colour distribution to be bimodal, with the blue and red peaks at $(R_{\rm C} - z) = 0.41 \pm 0.01$ and 0.70 ± 0.02 respectively. Bimodality was also found in the *HST*/ACS West pointing used to design the DEIMOS masks in the central region. The colour peaks occur at (F435W $-$ F814W) $= 1.77 \pm 0.03$ and 2.17 ± 0.01 respectively.

We find 109 spectroscopically confirmed GCs over 5 DEIMOS masks observed in sub-arcsec seeing conditions. Using a colour split at $(R_{\rm C} - z) = 0.57$ and excluding the marginal GCs, we investigate the kinematics of the resulting 60 blue and 42 red GCs respectively.

We find significant rotation only for the red GCs, which rotate roughly along the photometric major axis in agreement with the host galaxy stars. The 2–D velocity field of the red GCs is akin to that of ATLAS$^{\rm 3D}$ in the inner regions (Figure 2.13). The blue GCs have a marginally higher velocity dispersion profile than the red GCs.

2.5.5 NGC 3377

NGC 3377 is a classical E6 elliptical in the Leo I group and the closest galaxy in our sample. The resolved stellar properties of NGC 3377 have been studied by (Harris et al., 2007b) that found no

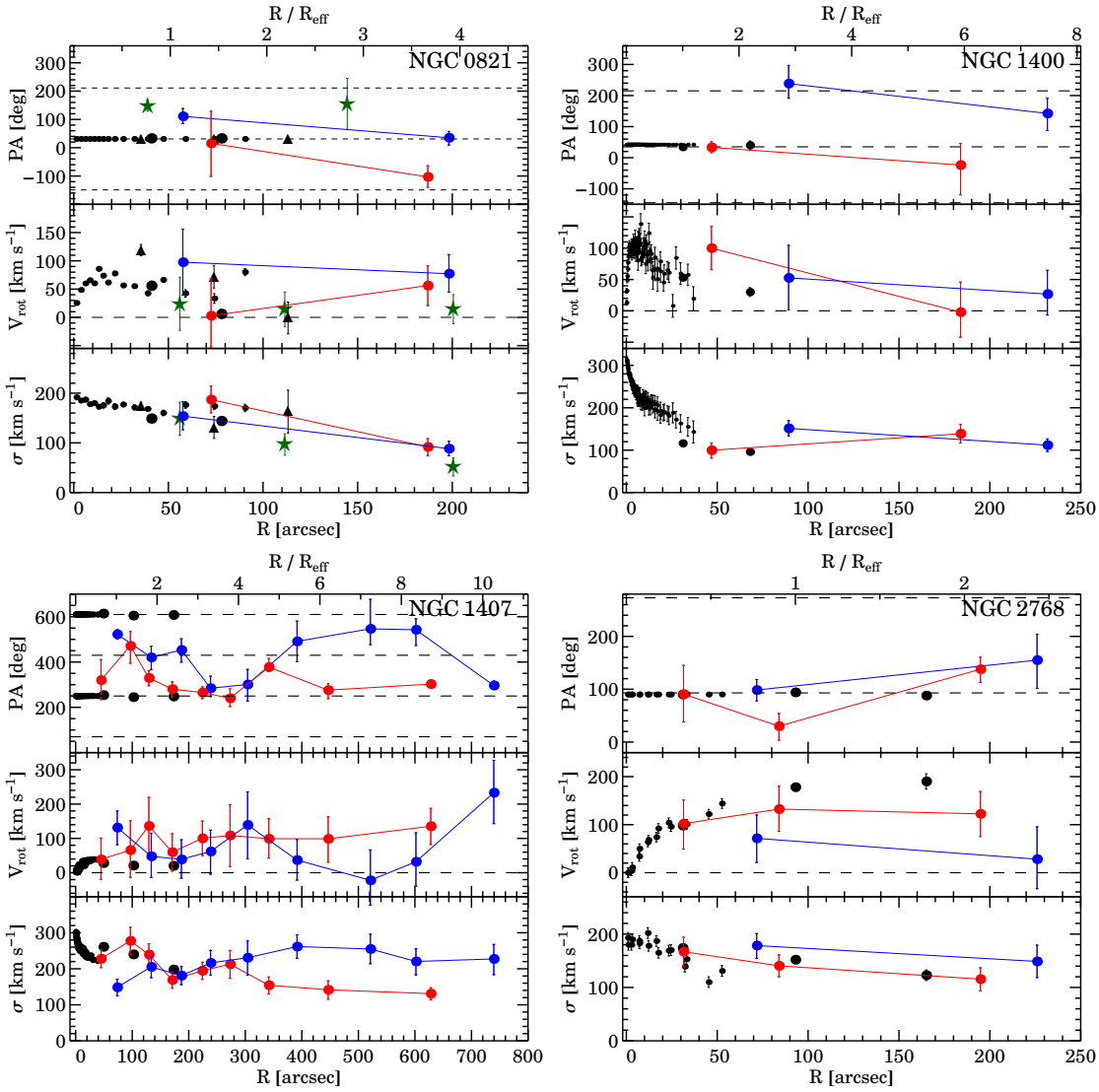

Figure 2.11 GC system kinematics compared to stellar data. For each galaxy (labeled on the top right of each panel) the plots represent the set of parameters $(PA_{\rm kin}, V_{\rm rot}, \sigma)$ that minimise eq. 2.3 as a function of the radius. Data points are joined for clarity, with the error bars representing the 68 per cent confidence intervals. The dashed horizontal lines in top and middle panels represent the photometric $PA \pm 180$ deg from Table 2.1 and $V_{\rm rot} = 0$, respectively. All the PNe data (green stars) are from Coccato et al. (2009). Integrated stellar light data are shown as small black points (if from long–slit) and large black points (if from Proctor et al. 2009). References for long–slit data are: Forestell & Gebhardt (2010) for NGC 821; Proctor et al. (2009) for NGC 1400 and NGC 1407; Fried & Illingworth (1994) for NGC 2768; Coccato et al. (2009) for NGC 3377; van der Marel & Franx (1993) for NGC 4278; Bender et al. (1994) for NGC 4365; Kronawitter et al. (2000) for NGC 5846; Simien & Prugniel (2000) for NGC 7457. Black trangles in NGC 821 are SAURON-IFU data from Weijmans et al. (2009). For NGC 7457, because of the low number statistics, we only show the total GC kinematic profile in black. Continues to next page.

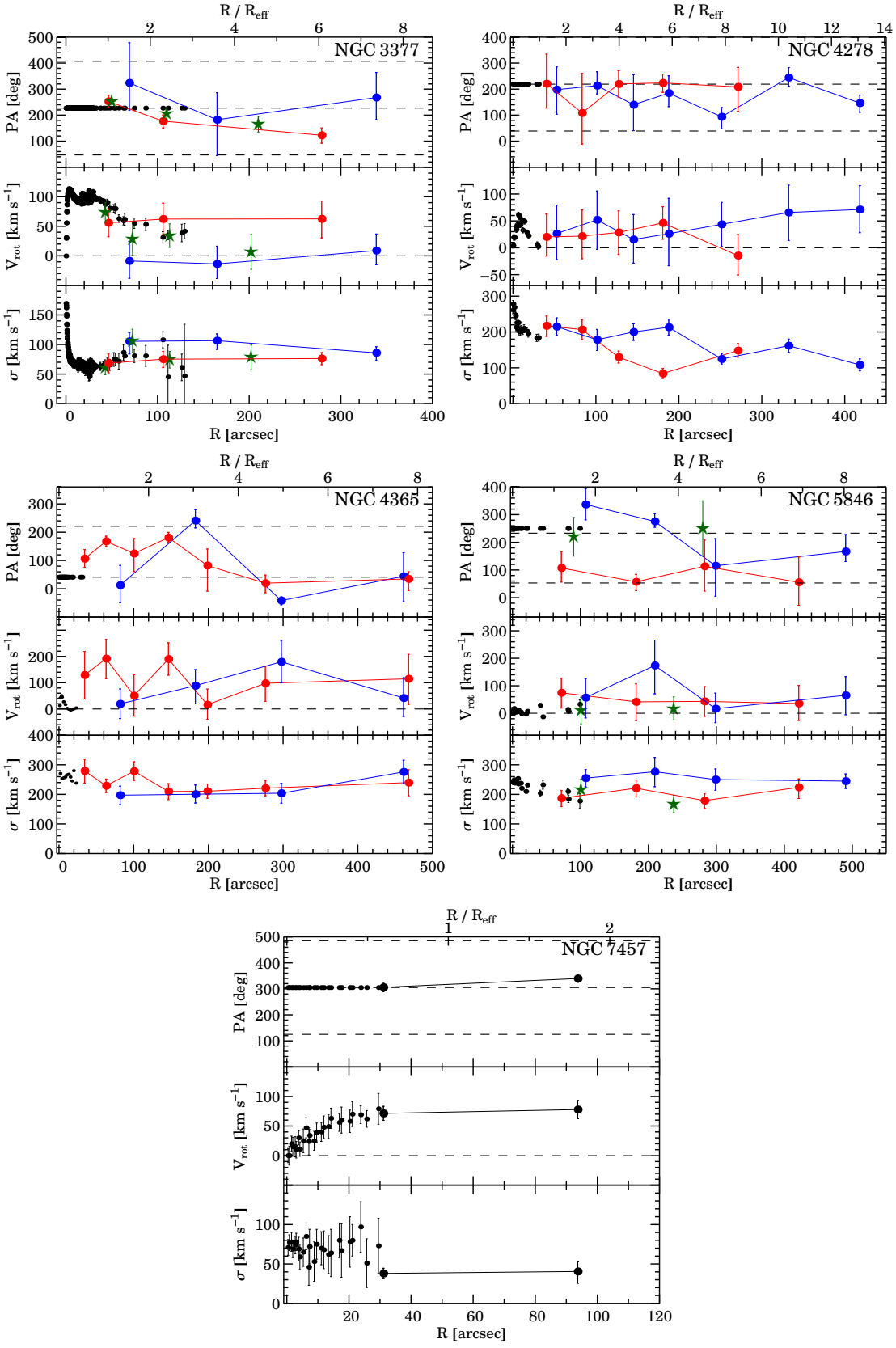
NGC 3377
NGC 4278
NGC 4365
NGC 5846
NGC 7457
R / R_eff
PA [deg]
V_rot [km s^-1]
σ [km s^-1]
R [arcsec]

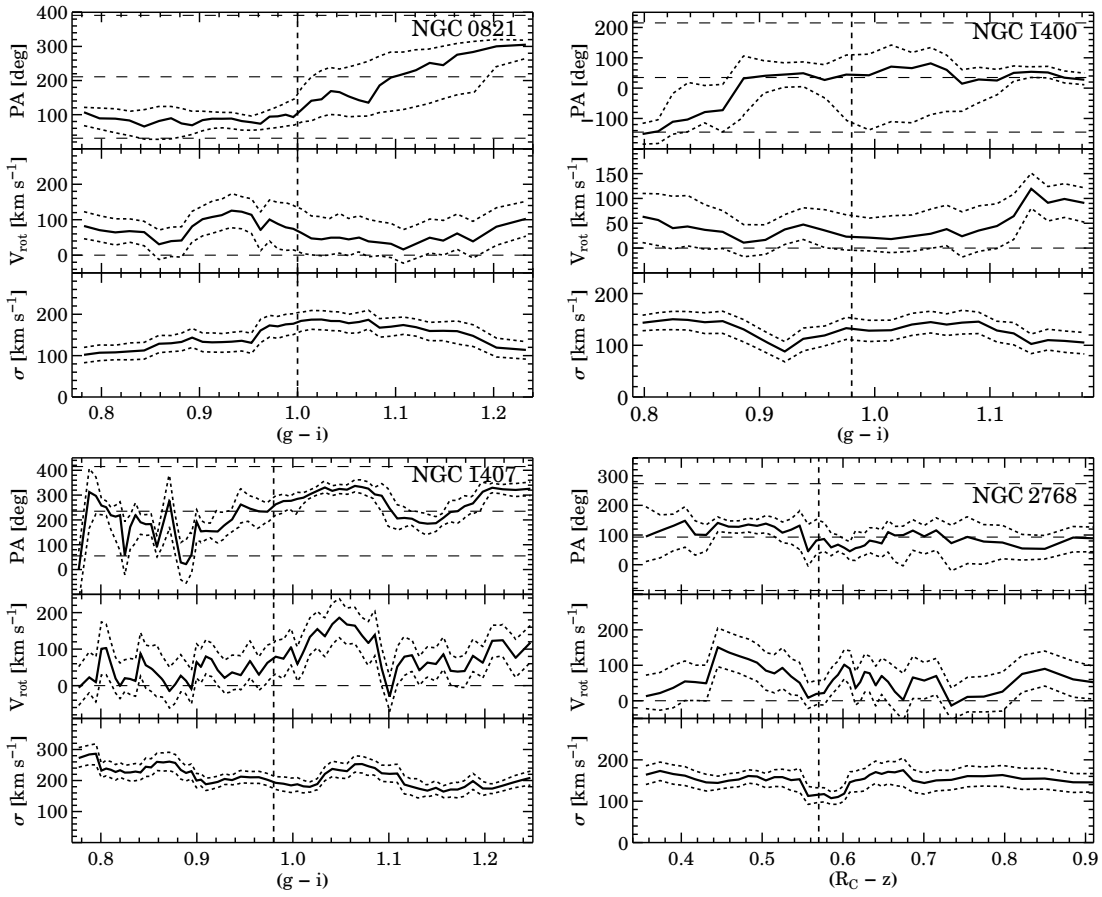

Figure 2.12 GC kinematics as a function of colour. Kinematic position angle, rotation velocity and velocity dispersion are shown in the top, central and bottom panel respectively. Dotted lines represent 68 per cent confidence intervals. Also shown are the photometric major axis (horizontal dotted lines) from Table 2.1 and the colour split between blue and red GC subpopulations (vertical dashed line) as derived from the KMM analysis. Continues to next page.

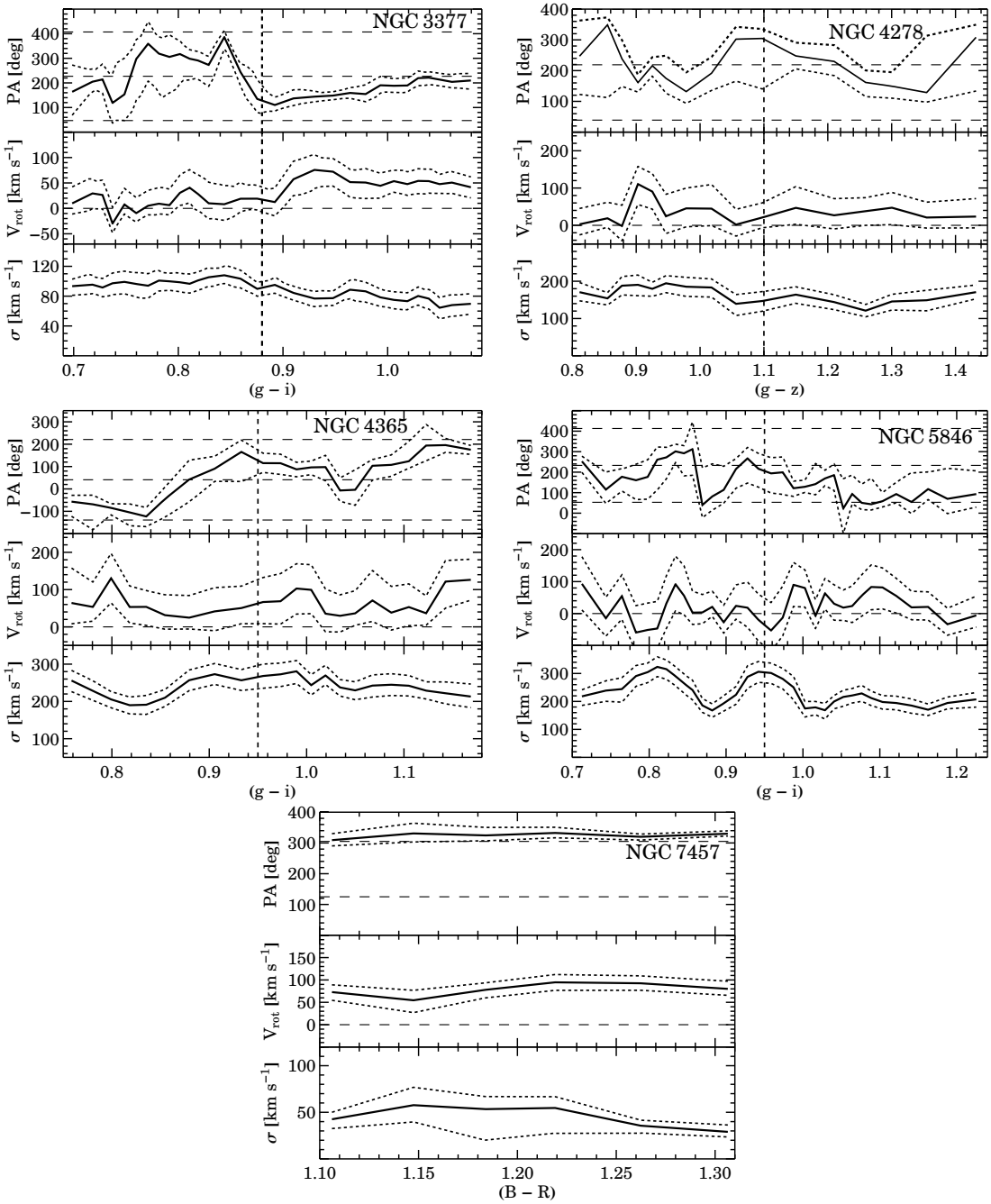
NGC 3377
NGC 4278
NGC 4365
NGC 5846
NGC 7457
PA [deg]
V_{rot} [km s^{-1}]
σ [km s^{-1}]
(g − i)
(g − z)
(B − R)

evidence for any young (< 3 Gyr) stellar population. Coccato et al. (2009) studied 159 PNe in this galaxy, detecting significant rotation within 2 arcmin and a kinematic major axis twist of ~ 80 deg from the major towards the minor axis. Kundu & Whitmore (2001), Chies-Santos et al. (2011b) and Cho et al. (2012) studied the GC system of this galaxy using *HST* imaging, finding the colour distribution to be likely bimodal.

NGC 3377 was imaged with gri filters and gz filters for ground based and space based observations respectively. We found a high probability for the colour distribution to be bimodal, both in our Suprime-Cam and in the supplementary ACS archive imaging, as already found in Chies-Santos et al. (2011b).

In this work, we present radial velocities for 126 GCs, observed in 4 DEIMOS masks. It is worth noting that we extend the kinematics of this galaxy to 8 $R_{\rm eff}$ $\sim$ 25 kpc, two times further than the PNe studies. We rule out two GCs that are likely to belong to the spiral galaxy NGC 3377A ($V_{\rm sys}$ $\sim$ 573 km s^{-1}) that lies $\sim$ 8 arcmin North-West from NGC 3377. With a colour split at $(g-i) = 0.88$ we study the kinematics of 57 blue and 60 red GCs, respectively.

We detect significant rotation for the red GC subpopulation along the photometric major axis in agreement with PNe and long–slit data (Coccato et al., 2009). As found for the PNe, we discover that the kinematic position angle of the red GC subpopulation twists with radius from 250 deg to 150 deg (see also Figure 2.10). The 2–D velocity field of the red GCs is consistent with ATLAS$^{\rm 3D}$ in the inner regions (Figure 2.13). The position angle of the blue GC subpopulation is unconstrained, implying an overall null rotation with radius. The velocity dispersion of the red GC subpopulation is very flat and it matches the stellar and the PNe. The blue GCs have an overall higher velocity dispersion profile than the red GC subpopulation.

2.5.6 NGC 4278

NGC 4278 is an elliptical (E1–2) member of the Coma I cloud. It has been extensively studied at different wavelengths: in radio, Nagar et al. (2005) detected two sub-parsec jets; in X-rays, a long (months) time scale variability (Ho et al., 2001) and a dominant nuclear source (Younes et al., 2010) were detected. It has long been known for its massive ($\sim 10^8$ M$_\odot$) H I disc extending beyond 10 $R_{\rm eff}$ (Gallagher et al., 1977) and used to infer the dark matter content at large radii (Bertola et al., 1993). The bimodality of the GC system of NGC 4278 has been under debate. Both Forbes et al. (1996b) and Kundu & Whitmore (2001) investigated the GC system of NGC 4278 with *HST*/WFPC2, finding a marginal or "likely" probability for the $(V-I)$ distribution to be bimodal. Recently, Chies-Santos et al. (2011b) combined *HST*/ACS and WHT/LRIS imaging, finding evidence for bimodality in space-based but not ground-based datasets.

In this work we present new wide field BVI Suprime-Cam imaging (with the B band in poor

seeing conditions), combined with four g and z *HST*/ACS pointings downloaded from the Hubble Legacy Archive (see Section 2.3.2). We find statistically significant bimodality both in our ground-based and space-based observations, with the colour separation occurring at $(B-I) \sim 1.9$ and $(g-z) = 1.1$, respectively.

We spectroscopically confirm 256 GCs over four DEIMOS masks observed in good seeing conditions. Given the wide field coverage of the four *HST* pointings, we decided to use *HST* magnitudes to divide the kinematics of blue and red GC subpopulations, converting $(V-I)$ colours into $(g-z)$ if only Subaru photometry was available. As for other group members, we exclude from the kinematics analysis GCs that might be associated with other galaxies. We select and remove three GCs whose position and radial velocity are consistent with the galaxy NGC 4283 ($V_{\rm sys} = 984\,{\rm km\ s^{-1}}$) that lies 3.6 (~ 15 kpc) arcmin from NGC 4278.

We find no clear evidence for red GC rotation, but there is a hint that the blue GCs rotate in the outer regions along a direction intermediate between the major and the minor axis. The velocity dispersion of the red and blue GCs seem to be in good agreement with long–slit data in the inner regions although there is no direct overlap between the two datasets. The blue GCs have an overall higher velocity dispersion at intermediate radii.

2.5.7 NGC 4365

NGC 4365 is a massive elliptical (E3) behind the Virgo cluster with signs of an ongoing merger (Mihos et al. 2012, in preparation). It has a kinematically distinct core (Krajnović et al., 2011) and an unusual stellar rotation along the photometric minor axis (Bender et al., 1994). Its GC system is mainly known for an odd GC colour distribution that seems to suggest the presence of three, instead of the classic two, subpopulations (Larsen et al., 2003, 2005; Brodie et al., 2005; Blom et al., 2011).

We make use of the photometric results presented in Blom et al. (2011) based on gz *HST*/ACS and gri Suprime-Cam imaging. In this work, we will treat the GC system of NGC 4365 as made up of two classic subpopulations and we refer to Blom et al. (2012, in preparation) for a detailed study of the kinematics of the three subpopulations. We use a colour split at $(g-i) \sim 0.91$ that includes the "green" GCs as part of the red subpopulation. We represent here the surface density profile published in Blom et al. (2011) that shows that red GCs is more centrally concentrated than the blue GC subpopulation, with a trend similar to that of the galaxy stellar light (Figure 2.6).

We spectroscopically confirm 269 GCs over 6 DEIMOS masks. We study the kinematics of 87 blue and 164 red GCs respectively. We also add 9 GCs from the combined dataset of Larsen et al. (2003) and Brodie et al. (2005) as described in §2.4.2. We find that the red GCs rotate within $R < 200$ arcsec along the photometric minor axis, mimicking the kinematics of the stars. The

rotation of the blue GCs is only significant at intermediate radii. The velocity dispersion profile is identical for the blue and the red GCs.

2.5.8 NGC 5846

NGC 5846 is the brightest member of a galaxy group. The dynamics of NGC 5846 has been modelled within $1R_{\rm eff}$ (Cappellari et al. 2007; Kronawitter et al. 2000). Recently, Das et al. (2008) derived the mass of this galaxy up to $11R_{\rm eff}$ exploiting X-ray and PNe observations. An *HST*/WFPC2 analysis of the NGC 5846 GC system was given in Forbes et al. (1997b) and then revisited by Chies-Santos et al. (2006). In addition to the classic bimodality, they also discovered that the GC system is better aligned with the galaxy's minor axis than its major axis and that this galaxy has an unusually low specific frequency compared to similar dominant ellipticals in groups or clusters.

In this work we present new Subaru photometry in gri filters, with the g band in moderate seeing conditions ($\sim$ 1 arcsec). Although the red peak is not clearly visible (Figure 2.5), KMM returned a high probability for the colour distribution to be bimodal with a colour split at $(g-i) = 0.95$.

We spectroscopically confirm 195 GCs over 6 DEIMOS masks. We also note that some radial velocities might be associated with other bright members of the group as NGC 5846A ($V_{\rm sys} = 2200\,{\rm km\,s^{-1}}$) and NGC 5845 ($V_{\rm sys} = 1450\,{\rm km\,s^{-1}}$). However the similar systemic velocities of these galaxies with NGC 5846 ($V_{\rm sys} = 1712\,{\rm km\,s^{-1}}$) makes any attempt to distinguish their GC populations problematic. We also supplement our DEIMOS catalogue with 22 GCs from the dataset of Puzia et al. (2004) as described in §2.4.2. In summary, we study the kinematics of 104 blue and 108 red GCs.

We detect rotation only for the blue GCs, which rotate between 150 and 300 arcsec close to photometric major axis. This feature might be caused by the GCs of NGC 5846A, which contaminates our sample within 300 arcsec. The velocity dispersion of the red GCs is flat with radius and consistent with other studies, although the PNe seem to suggest a slightly decreasing slope. The blue GCs have a systematically higher velocity dispersion than the red GC subpopulation.

2.5.9 NGC 7457

NGC 7457 is an isolated S0 with a pseudo-bulge detected both photometrically (Tomita et al., 2000) and kinematically (Pinkney et al., 2003) that shows an unusually low central velocity dispersion for its luminosity. Emsellem et al. (2007) revealed that this galaxy has a small counter rotating core that might be the result of a merger. Chomiuk et al. (2008) gave an overview of the GC system of NGC 7457 using *HST* observations and Keck/LRIS spectra for 13 GCs. They

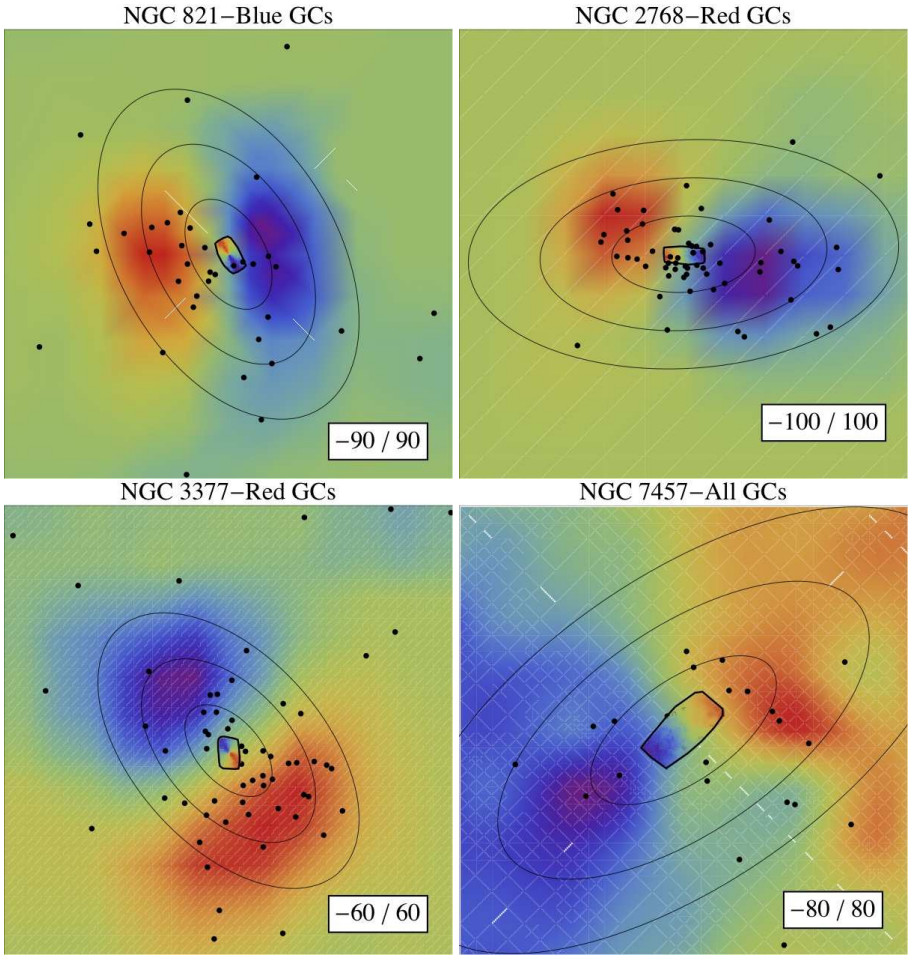

Figure 2.13 Two-dimensional smoothed velocity fields of our disky early-type galaxies. Black points and ellipses represent the locations of the spectroscopically confirmed GCs for a given population and the $2, 4, 6$ $R_{\rm eff}$ isophotes corrected for the galaxy ellipticity respectively. The white boxes are the maximum red-shifted and minimum blue-shifted velocities in the galaxy rest frame in unit of km s^{-1}. The SAURON stellar velocity maps are also shown in the innermost region of the galaxies. The agreement between the two datasets (except for NGC 821) is extremely good.

find evidence for a third intermediate population of GCs sharing the same age (2 –2.5 Gyr) as the young nuclear (radius of 1.5 arcsec) stellar population discovered by Sil'chenko et al. (2002).

NGC 7457 is the only galaxy in our sample not observed with Suprime-Cam. We have instead used the photometric results of Hargis et al. (2011) to design our DEIMOS masks, and we refer to their paper for a detailed description of the data reduction and analysis. They provide wide field WIYN/Minimosaic photometry of the GC system of this galaxy, finding that the colour distribution is not bimodal and showing the total population to be made up of 210 ± 30 GCs with a radial extent of 12 ± 2 kpc.

We find 21 spectroscopically confirmed GCs in two DEIMOS masks observed in average 0.9 arcsec seeing conditions. We also obtained spectra for 7 of the 13 GCs already observed by Chomiuk et al. (2008), finding their LRIS and our DEIMOS radial velocities to be consistent within the errors, but with a mean difference of $\sim 12\,\mathrm{km\,s^{-1}}$ (see §2.4.2). Therefore, we add the remaining 6 Chomiuk GCs corrected for the velocity offset to our GC sample. The final GC catalogue consists of 27 GC radial velocities.

Our confirmed GCs appear to be distributed within 2 arcmin ~ 7.7 kpc from the galaxy centre, reflecting the expected poor extent of the underlying GC subpopulation. The mean velocity of the system ($V_{\rm sys} = 847 \pm 20\,\mathrm{km\,s^{-1}}$) is in good agreement with both Chomiuk et al. (2008) and literature data. As this galaxy appears to be unimodal in colour, we fit the kinematics of all the GCs without any split in colour and we compare the results with the long-slit data of Simien & Prugniel (2000). We find that the GC system of NGC 7457 is rapidly rotating along the photometric major axis, with a flat rotation curve at $\sim 80\,\mathrm{km\,s^{-1}}$ up to $2R_{\rm eff}$. In contrast, the velocity dispersion is low ($< 50\,\mathrm{km\,s^{-1}}$) at all radii. The agreement with the ATLAS$^{\rm 2D}$ velocity map is also very good (Figure 2.13). We will discuss the implication of these results in more detail in §2.10.4.

2.6 GC formation models

Having determined the photometric and kinematic properties of our GC sample, in the following sections we will discuss these results as a whole. We look for common kinematic features that might retain key information about the formation history of the galaxies themselves and then we compare these results to theoretical models. In order to do so, it is first worth giving a brief summary of the main GC formation scenarios proposed in the literature, focusing on their kinematic predictions.

To date, the formation of GC bimodality has been investigated both in a cosmological context (Kravtsov & Gnedin, 2005; Diemand et al., 2005; Moore et al., 2006) and at smaller scales, with models fine tuned to reproduce the properties of specific galaxies (see Vesperini et al. 2003 for NGC 4486 or Deason et al. 2011 for the Milky Way and M31). The challenge of producing simu-

lations of GC bimodality formation is intertwined with our poor understanding of how GC systems formed in the first place (e.g., Beasley et al., 2002; Elmegreen et al., 2012). As a consequence, the three classic formation scenarios proposed in the literature and summarized below have few, if any, theoretical predictions directly comparable with the observations. In particular, there is a general dearth of GC kinematics predictions.

In the *major merger scenario* (Ashman & Zepf, 1992) two or more gas-rich disk galaxies with pre-existing blue and red GC subpopulations merge to form an elliptical galaxy. New red GCs may form from the star formation induced by the merger (Bekki et al., 2002).

This scenario has been simulated by Bekki et al. (2005) (hereafter B+05). In this simulation the pre-existing blue and red GCs are assumed to have a Milky Way-like spatial distribution, but they are both pressure-supported. This is a reasonable assumption for the blue but not for the red GCs of the Milky Way that are known to be rotation-supported (Côté, 1999; Deason et al., 2011). B+05 predicted that a merger with even mass-to-mass ratio produces strong rotation for both GC subpopualtions in the outer regions of the remnant. This result is independent of the orbital configuration of the merger. The velocity dispersion profile is predicted to decrease with radius, but it would be flatter in case of multiple mergers. Also, the blue GCs are expected to show a larger central velocity dispersion than red GCs. Finally, the ratio of the maximum rotational velocity $V_{\rm m}$ to the central velocity dispersion σ_0 of the GC systems ranges from 0.2 to 1.0 within $6R_{\rm eff}$ for both the blue and red GC subpopulations, but most GC systems, viewed from various angles, have $(V_{\rm m}/\sigma_0) < 0.5$. Bekki & Peng (2006) carried out a simulation similar to that of B+05 (with the rotation of the disk in the spiral progenitors included), fine tuned to study the dynamics of the planetary nebulae (PNe) in elliptical galaxies. They found that the effect of the residual spin disk (additional to the initial orbital angular momentum) on the final PNe kinematics enhances the rotation at all radii, making the merger remnant rotation-supported.

In the *multiphase dissipational collapse scenario* (Forbes et al., 1997a), GCs are the result of an early two phase collapse, and hence two main star formation episodes, that the galaxy undergoes. The blue GCs form during the first star formation episode in a metal-poor cloud, whereas red GC subpopulation form in a second phase after the gas in the galaxy is self-enriched. In this scenario, a fraction of blue GCs might also come from accreted satellite galaxies, similar to the most recent two-phase galaxy formation model (Oser et al., 2010). No numerical simulations have been performed so far to test this model. Since the red GCs are coeval with the galaxy stellar component, Forbes et al. (1997a) infer that they should share the same kinematic properties as the galaxy stars, and hence also the same spatial distribution. No significant rotation is expected for the blue GC subpopulation.

In the *dissipationless accretion scenario* (Côté et al., 1998), the red GCs form from the mono-

lithic collapse of a giant protogalactic cloud, whereas the blue GCs are accreted from low mass galaxies due to mergers or tidal stripping. To date, simulations based on similar scenarios have been performed (e.g., Oser et al., 2010) but they do not include GC particles, and they have not made kinematic predictions. In addition to the observation of infalling co-moving groups, Côté et al. (1998) also infer that we should expect to observe blue GCs with radially biased orbits without overall rotation.

Bekki et al. (2008) (hereafter B+08) performed a high resolution N-body cosmological simulation combined with semi-analytic models. They found that almost half of the simulated 10^5 galaxies show clear bimodality in their GC metallicity distribution. The majority of GCs form in low-mass galaxies at redshift greater than 3 with the blue GCs being slightly older (< 1 Gyr) than the red GC subpopulation. B+08 also made predictions for the overall kinematics of each GC system, whereas current spectroscopic observations only sample a smaller fraction of it. They find that the velocity dispersion of blue and red GC subpopulations increases with the total luminosity of the host galaxy and that the ratio of the velocity dispersion of the blue to red GC subpopulation is $(\sigma_{\rm B}/\sigma_{\rm R}) \sim 1$ for a wide range of luminosity. Finally, they also predicted that the GC systems of most galaxies are mainly pressure supported with $(V_{\rm rot}/\sigma) < 0.3$. This is in contrast with the wider range of $V_{\rm rot}/\sigma$ found by B+05.

2.7 Global results from our GC sample

In this section we summarize the results for the GC systems presented in this work, including the three galaxies previously published by us (i.e., NGC 3115, NGC 4486, NGC 4494). Section 2.8 will incorporate other literature data, and tackle topics not covered here.

2.7.1 Spatial Distribution

Significant colour bimodality was detected in all the GC systems, except for NGC 7457. All GC system formation scenarios, as well as numerical simulations, predict that this bimodality should be reflected in different spatial distributions of the two subpopulations around the parent galaxy. A glance at Figure 2.6 reveals that this is also the case for our galaxy sample. Generally speaking, the red GCs are more centrally concentrated than the blue GCs, as already found in other studies (e.g., Schuberth et al., 2010; Faifer et al., 2011; Strader et al., 2011).

The advent of wide field imaging has shown that the radial distribution of the red GC subpopulation matches that of the host galaxy light, suggesting that they might have shared a similar formation history (Bassino et al., 2006). Here we have exploited the 34×22 arcmin^2 field of view of our Suprime-Cam imaging to compare the GC surface density to the surface brightness

of the respective host galaxy (shifted by an arbitrary constant). Qualitatively speaking, the galaxy starlight has a similar slope to that of the red GC subpopulation. The discrepancies between the surface brightness and the GC spatial distribution in innermost regions (e.g., see NGC 4365 and NGC 1407 in Figure 2.6) is due to the core-like distribution of the GCs, that makes the GC density profile flatter. This feature is interpreted as the effect of the GC disruption, stronger in the central regions (Baumgardt, 1998; Baumgardt & Makino, 2003).

2.7.2 Rotation and velocity dispersion

We find a large variety of GC rotation profiles. Both the blue and red GCs show some degree of rotation, but there does not seem to be a clear correlation between the rotation patterns and the property of the host galaxy. A glance at Figure 2.11 reveals that the red GCs rotate more consistently with the photometric major axis than the blue GC subpopulation does. For our galaxy sample the photometric position angle coincides with the photometric major axis of the galaxy stars (except for NGC 4365), which means that the rotation velocity of the red GC subpopulation is similar to that of the galaxy stars. This is also true for the overall GC system of NGC 7457.

To quantify this phenomenon, in Figure 2.14 we compare the major axis rotation velocity of the blue and the red GC subpopulations within $3R_{\rm eff}$ to the rotation velocity of the stars and PNe (if available) at the same galactocentric distance. The exact extraction radius was set to $2R_{\rm eff}$, but in some cases this was relaxed by $\pm 1R_{\rm eff}$ to maximise the overlap between the GCs and the stars. The rotation velocity of the host galaxy stars was extracted along the photometric major axis for all the galaxies, except for NGC 4365 in which the bulk of the stellar rotation is occurring along the photometric minor axis. The red GC rotation for our galaxies is similar to those of the host galaxy stars, at least for galaxies with a conspicuous amount of stellar rotation. On the other hand, the star-GC system coupling is also evident for only blue GC subpopulations, such as in NGC 4494, NGC 821 and NGC 3115.

The rotation of the blue GCs is more puzzling than the red GCs. Overall the rotation of the blue GCs is lower than the red GCs and often consistent with zero, yet we also detect minor axis rotation in NGC 821, also seen in PNe, in contrast with integrated starlight.

We detect GC rotation at large galactocentric radii for some galaxies. This feature is only significant in NGC 1407, NGC 4486 and only marginal in NGC 4278. The outer rotation occurs in the same direction for both the blue and the red GC subpopulations and it usually coincides with the photometric major axis.

Our results show that the velocity dispersion profiles are quite flat for most of the galaxies, both as a function of radius (Figure 2.11) and as a function of the colour (Figure 2.12). The slope of the velocity dispersion profiles (including the contribution of the rotation) will be discussed

below.

As for the rotation, we study how the velocity dispersion of the two GC subpopulations compares to the velocity dispersion of the host galaxy stars. We extract the velocity dispersion at the same galactocentric distances as done with the rotation. Figure 2.14 shows that the velocity dispersion of the red GC is very similar to that of the host galaxy stars in the region of overlap. Conversely, the blue GC subpopulations seem to avoid the one-to-one line. The standard deviation from the one-to-one line is $22\,\mathrm{km\ s^{-1}}$ and $50\,\mathrm{km\ s^{-1}}$ for the red and the blue GC subpopulations respectively.

To quantify the differences between the velocity dispersion profiles of the two GC subpopulations, in Figure 2.15 we plot the ratio of the velocity dispersion of the blue GCs to the velocity dispersion of the red GCs ($\sigma_{\rm B}/\sigma_{\rm R}$) normalised to 3 $R_{\rm eff}$ as a function of the effective radius. In this case we show the velocity dispersion using rolling radial fits to appreciate the details of the profiles. Figure 2.15 shows that the ratio ratio $(\sigma_{\rm B}/\sigma_{\rm R})/(\sigma_{\rm B}/\sigma_{\rm R})_{3\,R_{\rm eff}}$ is generally consistent with 1, but it increases towards the outer regions for some galaxies, as already observed for more massive galaxies (Lee et al., 2010b).

The overall velocity dispersion profiles are in rough agreement with their merger remnants assembled via multiple mergers, with the velocity dispersion of the blue GCs being larger or equal to that of the red GCs. However, the model fails in reproducing the irregularity of some dispersion profiles (e.g., NGC 1407 and NGC 4278).

2.8 Including literature data

We examined the literature for galaxies with a reasonable number of GC radial velocity measurements. We require at least 20 spectroscopically confirmed GCs for a galaxy to be included in the literature sample. We use the same friendless algorithm as described in §2.4.1 to clip outliers in radius-velocity space. This selection returned ten GC systems, which are summarized in Table 2.7. Most of these galaxies are dominant group/cluster galaxies discussed in Lee et al. (2010b), whereas the less massive galaxies are part of the survey of Puzia et al. (2004). We also include NGC 3923 from Norris et al. (2012) which shows strong signatures a recent interaction. A first comparison between our GC dataset and external datasets was already given in Figure 2.2 in which we showed that we cover a wider range of mass with three times better velocity accuracy than previous studies.

2.8.1 Velocity Dispersion

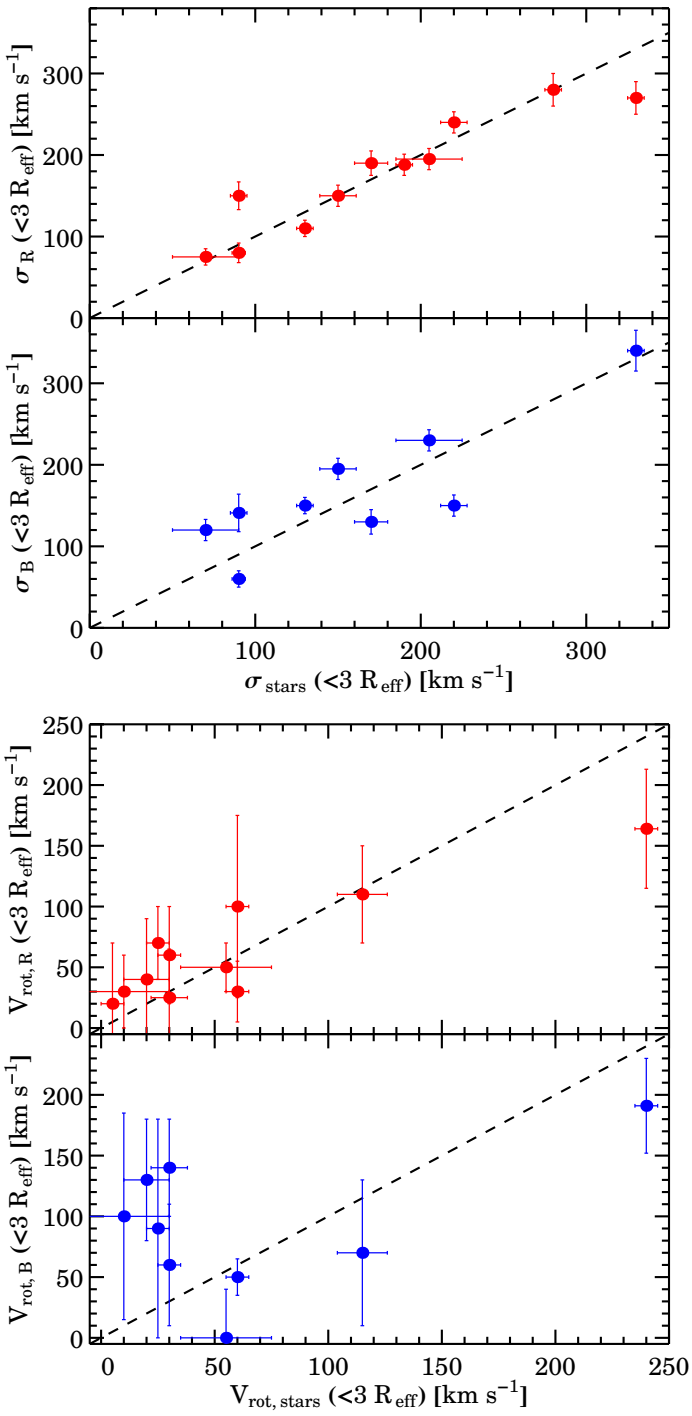

Figure 2.14 GC rotation velocities and velocity dispersions compared to the galaxy stars/PNe. Rotation velocities (*bottom*) and velocity dispersions (*top*) are extracted within $3R_{\rm eff}$. The exact extraction radius is usually set to $2R_{\rm eff}$ but this threshold is arbitrarily adjusted by $\pm 1R_{\rm eff}$ in case the GCs do not overlap with the stellar data. The blue and the red GC subpopulations are shown in the *bottom* and *upper sub-panel* respectively. Dashed lines represent a one-to-one relationship. Blue GC data for NGC 4365 and NGC 4278 are not shown due to limited radial range. NGC 7457 is not shown. The red GC subpopulation shows better agreement with stars than the blue GCs.

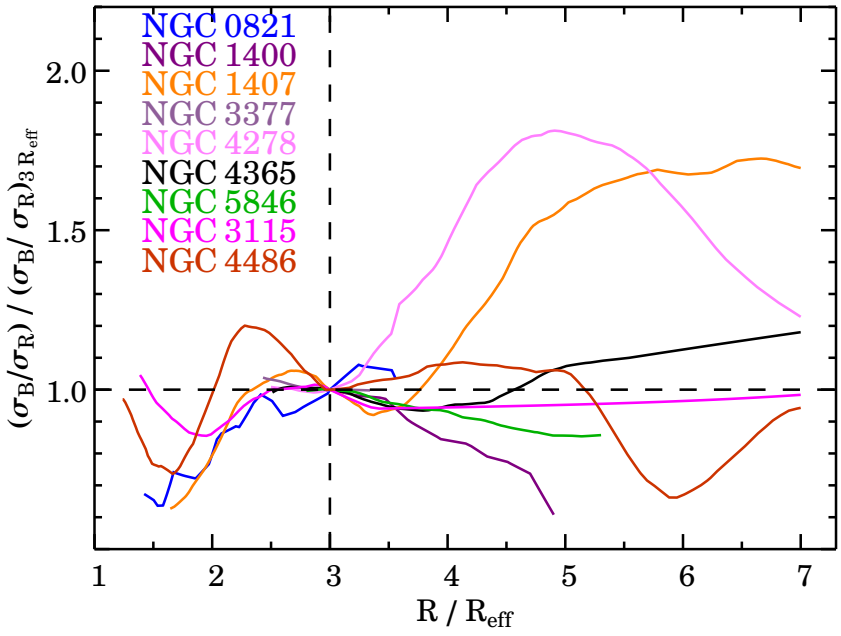

Figure 2.15 Velocity dispersion profiles. For each galaxy, we show the ratio of the velocity dispersion of blue to red GC subpopulations normalised to 3 $R_{\rm eff}$ (vertical dashed line) as a function of the effective radius. Different colours correspond to different galaxies. The horizontal and vertical lines show $(\sigma_{\rm B}/\sigma_{\rm R}) = (\sigma_{\rm B}/\sigma_{\rm R})_{3\,R_{\rm eff}}$ and $R = 3R_{\rm eff}$, respectively. NGC 7457 and NGC 4494 are not shown.

Galaxy ID	Hubble Type	$M_{\rm K}$ [mag]	D [Mpc]	$N_{\rm GCs}$	$V_{\rm rms,A}$ [km s^{-1}]	$V_{\rm rms,B}$ [km s^{-1}]	$V_{\rm rms,R}$ [km s^{-1}]	$(V_{\rm rot}/\sigma)_{\rm A}$	$(V_{\rm rot}/\sigma)_{\rm B}$	$(V_{\rm rot}/\sigma)_{\rm R}$	Ref.
(1)	(2)	(3)	(4)	(5)	(6)	(7)	(8)	(9)	(10)	(11)	(12)
NGC 1380	SA0	-24.3	17.1	42	160^{+23}_{-17}	142^{+38}_{-25}	170^{+32}_{-22}	$0.39^{+0.25}_{-0.35}$	$0.32^{+0.79}_{-0.54}$	$0.05^{+0.30}_{-0.22}$	P+04
NGC 1399	E1	-25.1	19.4	738	292^{+8}_{-8}	325^{+13}_{-12}	266^{+10}_{-9}	$0.19^{+0.04}_{-0.05}$	$0.28^{+0.06}_{-0.06}$	$0.07^{+0.06}_{-0.08}$	S+10
NGC 3311	cD	-25.2	46.7	116	653^{+48}_{-40}	–	–	$0.03^{+0.14}_{-0.12}$	–	–	M+11
NGC 3379	E1	-23.7	10.2	39	171^{+24}_{-18}	–	–	$0.08^{+0.22}_{-0.15}$	–	–	P+06; B+06
NGC 3585	E6	-24.7	19.5	20	159^{+35}_{-23}	–	–	$0.43^{+0.28}_{-0.31}$	–	–	P+04
NGC 3923	E4	-25.3	22.3	79	273^{+42}_{-29}	273^{+42}_{-29}	200^{+26}_{-19}	$0.24^{+0.12}_{-0.16}$	$0.31^{+0.26}_{-0.27}$	$0.00^{+0.14}_{-0.22}$	N+12
NGC 4472	E2	-25.6	16.7	225	305^{+15}_{-14}	334^{+22}_{-19}	256^{+22}_{-19}	$0.19^{+0.09}_{-0.10}$	$0.27^{+0.10}_{-0.10}$	$0.08^{+0.14}_{-0.07}$	C+03
NGC 4636	E2	-24.3	14.2	259	212^{+11}_{-10}	226^{+18}_{-15}	200^{+15}_{-12}	$0.05^{+0.07}_{-0.11}$	$0.09^{+0.14}_{-0.12}$	$0.18^{+0.13}_{-0.10}$	L+08
NGC 4649	E2	-25.3	16.3	121	225^{+17}_{-14}	209^{+20}_{-16}	257^{+37}_{-26}	$0.61^{+0.12}_{-0.12}$	$0.59^{+0.16}_{-0.15}$	$0.70^{+0.24}_{-0.25}$	H+08
NGC 5128	S0	-24.1	4.1	449	115^{+5}_{-5}	113^{+7}_{-6}	117^{+7}_{-7}	$0.26^{+0.08}_{-0.05}$	$0.25^{+0.10}_{-0.11}$	$0.28^{+0.09}_{-0.11}$	W+10

Table 2.7 Kinematical properties of literature GC systems. The host galaxy name (1) and Hubble Type (2) are from NED database. K band absolute magnitude (3) is from 2MASS apparent magnitude at the distances given in column 4 and corrected for the foreground Galactic extinction from NED database. The distance in Megaparsec (4) was obtained by subtracting 0.06 mag (Mei et al., 2007) from the distance modulus from Tonry et al. (2001), except for NGC 3311 for which we adopt the distance of the Hydra I cluster of $(m - M) = 33.37$ mag (Mieske et al., 2006). The number of spectroscopically confirmed GC system (5) is after the outliers filtering as described in the text. Columns (6), (7) and (8) are the root-mean-square velocity $V_{\rm rms}$ for all, blue and red GC subpopulations respectively. Columns (9), (10) and (11) are the (V/σ) value for all, blue and red GC subpopulations respectively. The data references are: P+04 (Puzia et al., 2004); S+10 (Schuberth et al., 2010); M+11 (Misgeld et al., 2011); P+06 (Pierce et al., 2006); B+06 (Bergond et al., 2006); N+12 (Norris et al., 2012); C+03 (Côté et al., 2003); H+08 (Hwang et al., 2008); L+08 (Lee et al., 2008b); W+10 (Woodley et al., 2010).

We ran the kinematic likelihood code on the literature galaxies to get the *overall* best fit values to eq. 2.4, but we do not show the kinematic radial profiles for the literature sample. We investigate the kinematics of blue and red GC subpopulations for seven out of ten galaxies using the dividing colour quoted in the respective papers. For consistency with the kinematic analysis of our galaxies, we do not exclude UCD candidates from the literature data. We find that our likelihood-method tends to reduce both the velocity dispersion (by $\sim$ 10 km s^{-1}) and the rotation amplitude (up to $\sim$ 30 km s^{-1}) if the contribution of the rotation is low ($V_{\rm rot}/\sigma < 0.4$). We attribute this discrepancy to the fact that some previous GC kinematics studies have employed error-weighted least-square rotation fittings that are less appropriate for a system with an intrinsic dispersion. Another explanation might be that, to our knowledge, previous studies have never explicitly taken into account the bias introduced by an unconstrained position angle (see §2.4.3), which has an important effect at lower velocities. It is important to note that the maximum-likelihood approach does not alter the general results of previous works.

2.9 Results

In this section we analyze the extended sample of 22 GC systems (literature plus our own galaxies), 18 of which have kinematics for both GC subpopulations. We carry out a number of tests to compare the kinematic properties of the two subpopulations with each other and with host galaxy properties.

2.9.1 Correlations with host galaxy properties

In Figure 2.16 we show the GC system kinematics as a function of the general properties of the host galaxies. We now have the chance to better constrain some relations examined by Lee et al. (2010b) that were uncertain because of their limited sample size of six galaxies (see their figure 12).

The upper panels of Figure 2.16 show that, as found from previous studies, a correlation exists between $V_{\rm rms}$ of the GC systems and their respective host galaxy X-ray luminosity L_X, central velocity dispersion of the stars σ_0 and absolute K-band magnitude M_K. We find that these correlations also hold for less massive galaxies. The correlations with galaxy properties are always tighter for our GC dataset as consequence of the improved reliability of our velocity measurements.

The correlation of $V_{\rm rms}$ with galaxy properties holds when we plot the $V_{\rm rms}$ of the blue and red GC subpopulations separately (see Figure 2.17).The main difference here is that the two subpopulations scatter differently with respect to the best fit lines. The rms of this difference for the

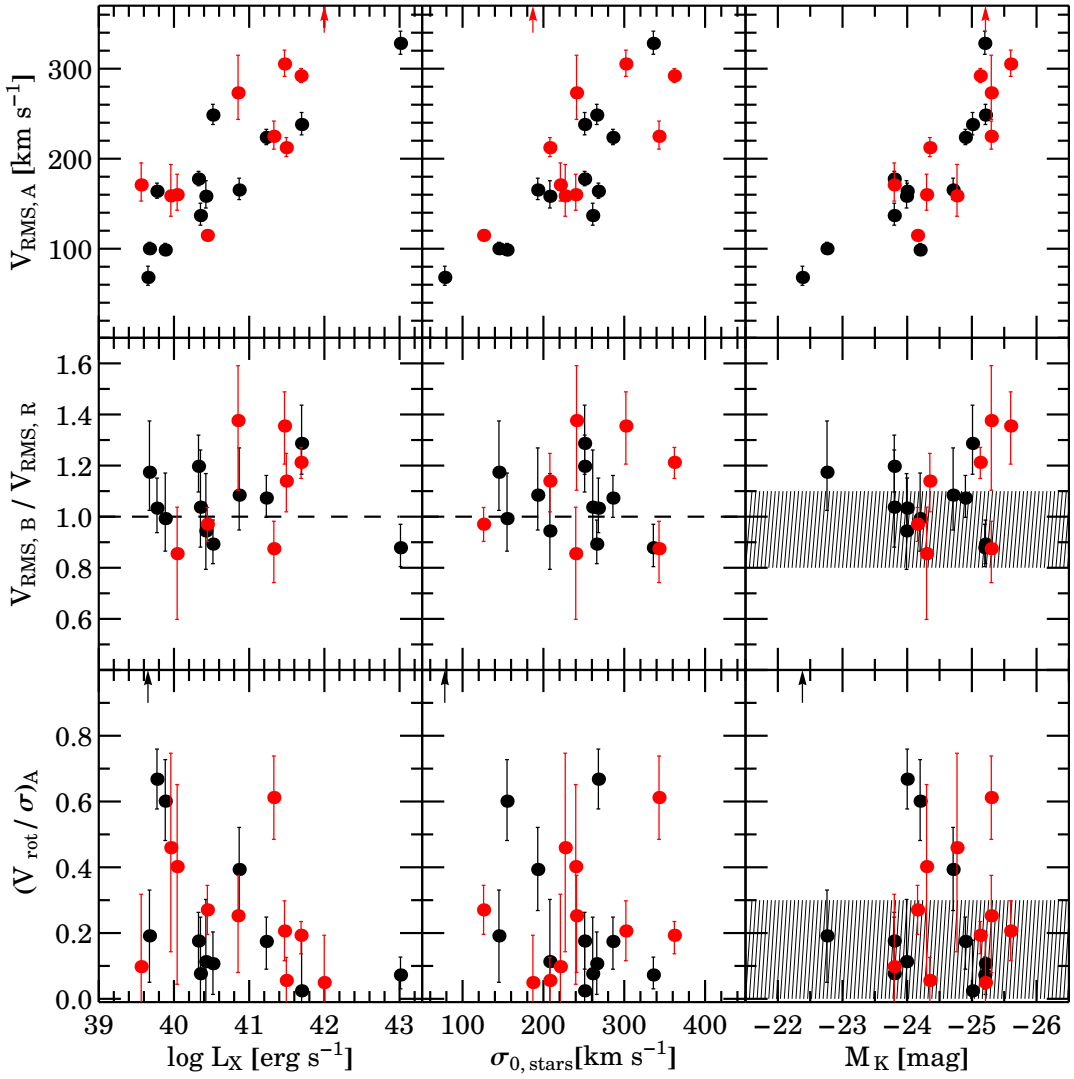

Figure 2.16 Summary of GC system kinematics as a function of the host galaxy properties. Literature data and our sample are shown as red and black points respectively. From the top to the bottom: root-mean-square velocity for the overall GC system ($V_{\rm rms,A}$), ratio of the $V_{\rm rms}$ of the blue to the red GC subpopulation ($V_{\rm rms,B}/V_{\rm rms,R}$), ratio of the rotation velocity to the velocity dispersion for the overall GC system $(V_{\rm rot}/\sigma)_{\rm A}$. From the left to the right: X-ray luminosity (log L_X) from O'Sullivan et al. (2001) at the distance given in Table 2.1 and Table 2.7, central stellar velocity dispersion ($\sigma_{0,\rm stars}$) from Prugniel & Simien (1996) and total K-band magnitude (M_K) from 2MASS. The black and red arrows indicate the position of NGC 7457 at $(V_{\rm rot}/\sigma)_{\rm A} = 1.68$ and of NGC 3311 at $V_{\rm rms,A} = 653\,{\rm km\,s^{-1}}$, respectively. The horizontal dashed line marks $V_{\rm rms,B}/V_{\rm rms,R} = 1$ to guide the eye. The grey shaded shaded region represents the theoretical predictions from the cosmological simulation of Bekki et al. (2008).

blue GCs is systematically larger for the red GCs.

In Figure 2.16, the middle panel shows that most of the GC systems have $V_{\rm rms,B}/V_{\rm rms,R} \geq 1$. This is seen more clearly as a function of the X-ray luminosity which is larger in galaxies with an extended massive halo to which most of the blue GCs are thought to belong (Forbes et al., 2012b). These results are in general agreement with the cosmological simulation of B+08 that predicted the $V_{\rm rms,B}/V_{\rm rms,R}$ ratio to be slightly ≥ 1 for a wide range of host galaxy magnitudes. We also tested the significance of the apparent correlation between $V_{\rm rms,B}/V_{\rm rms,R}$ and M_K finding a Spearman's rank correlation coefficient of $r_s = 0.35$, implying that a correlation is unlikely.

In the bottom panel of Figure 2.16 we quantify the GC system rotation by studying the overall $(V_{\rm rot}/\sigma)$, which estimates the contribution of the GC rotation over its random motions. We find that galaxies are spread between $0 < (V_{\rm rot}/\sigma)_{\rm A} < 0.8$ except for NGC 7457 with $(V_{\rm rot}/\sigma)_{\rm A} = 1.68$. It also appears that galaxies with lower L_X and lower σ_0 are more rotation-supported than other galaxies. The bulk of GC systems with $(V_{\rm rot}/\sigma) \leq 0.3$ is consistent with cosmological simulation of B+08. However, as previously discussed, trends of rotation with radius and colour are also important to examine.

2.9.2 Rotation

To make things clearer we divide the host galaxies into two kinematic groups that will be used throughout this section. After considering various possibilities, we finally decided to divide the GC systems according to the rotation dominance parameter of their host galaxy. We use the $\lambda_{R_{\rm eff}}$ parameter within $1R_{\rm eff}$ as defined in Cappellari et al. (2007) with a threshold of $0.31 \times \sqrt{\epsilon}$ to discriminate between slow and fast-rotators, where $\epsilon_{R_{\rm eff}} = 1 - (b/a)$ is the galaxy ellipticity. For our sample, we use $\lambda_{R_{\rm eff}}$ from Emsellem et al. (2011) if the galaxy is in ATLAS$^{\rm 3D}$, whereas we use the conversion formulae provided by the same authors to convert $V_{\rm max}/\sigma_0$ into $\lambda_{R_{\rm eff}}$, where $V_{\rm max}$ and σ_0 are the maximum rotation amplitude and the central velocity dispersion of the host galaxy respectively (Figure 2.18). This separation has the advantage of being independent of the galaxy inclination. It also allows us to test if the slow-fast rotator separation in the inner regions persists in the outer regions. The first group of galaxies is composed of slow-rotator galaxies and includes mostly round massive galaxies at the centre of groups or clusters. The second group includes fast-rotators but it covers a wide range of galaxy masses and morphologies, from E0 to S0. Fast-rotator galaxies with $\lambda_{R_{\rm eff}} > 0.25$ have stellar disky-like structures (photometric and/or kinematic) in the inner regions.

In Figure 2.19 we compare the *overall* rotational dominance parameter $(V_{\rm rot}/\sigma)$ of the blue and red GC subpopulations colour-coded according to their fast/slow rotator classification. We find that a dichotomy exists between the GC systems in slow and fast rotators. Most of the GC

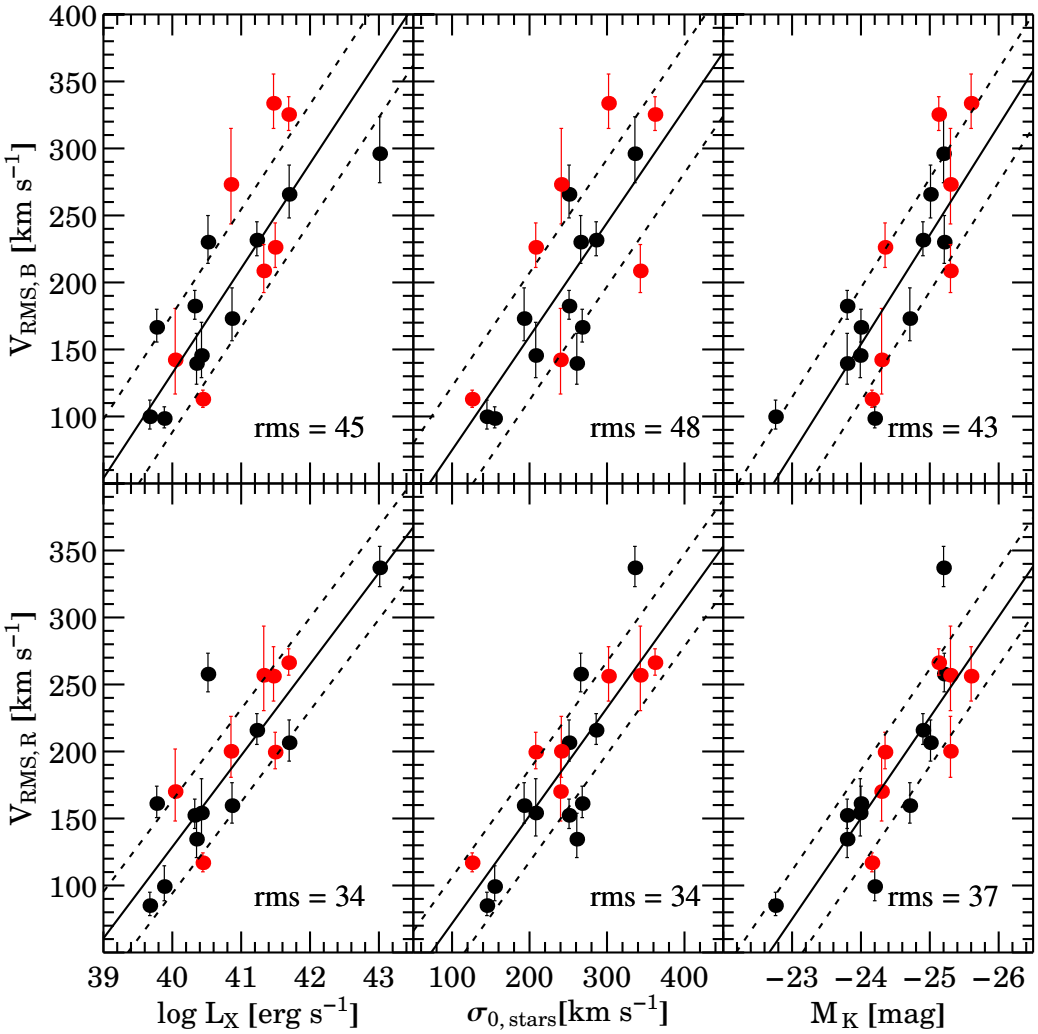

Figure 2.17 GC system $v_{\rm rms}$ as a function of the host galaxy properties. Literature data and our sample are shown as red and black points, respectively. The top and the bottom panels represent the velocity dispersion of the red and blue GC subpopulations as a function of the X-ray luminosity (log L_X), central stellar velocity dispersion ($\sigma_{0,\rm stars}$) and total K-band magnitude (M_K), respectively. The solid and dashed lines represent the weighted linear fit to the data and its rms in km s^{-1} quoted on the bottom right of each panel, respectively. The dependence of red GC subpopulation on the galaxy properties is tighter than for the blue GCs.

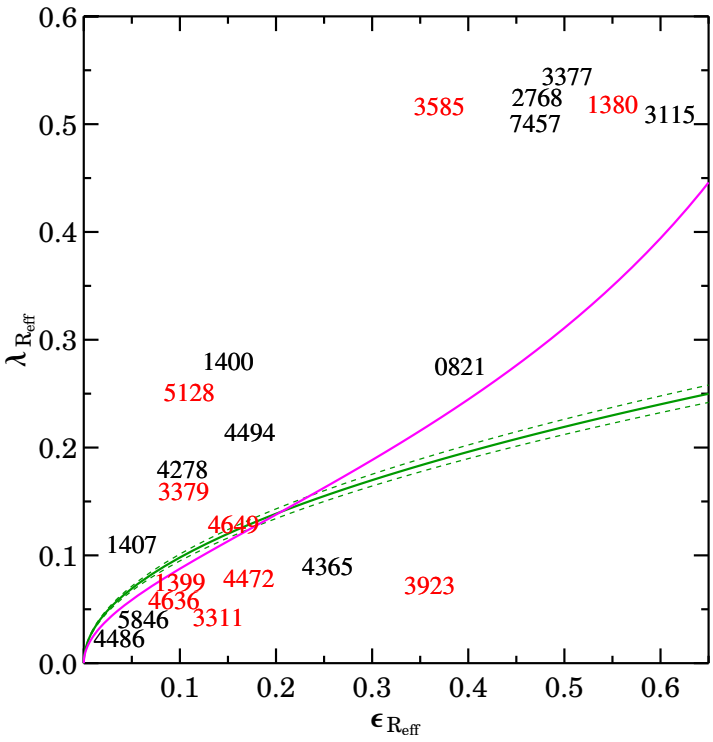

Figure 2.18 Rotational dominance parameter of the stellar component $\lambda_{R_{\rm eff}}$ versus the galaxy ellipticity $\epsilon_{R_{\rm eff}}$. Both quantities are measured within $1R_{\rm eff}$. Data points are represented by the NGC number of our galaxy sample (black) and literature data (red). Measurements are from Emsellem et al. (2011) if the galaxy is in ATLAS$^{\rm 3D}$. If not they are estimated from literature data (see text). The magenta curve is the inferred edge-on average relation for nearby fast-rotators. The solid green curve is $(0.31 \pm 0.01) \times \sqrt{\epsilon_{R_{\rm eff}}}$, with the dashed lines representing its uncertainties. Galaxies are divided into fast-rotators and slow-rotators if they are above or below the green curve respectively.

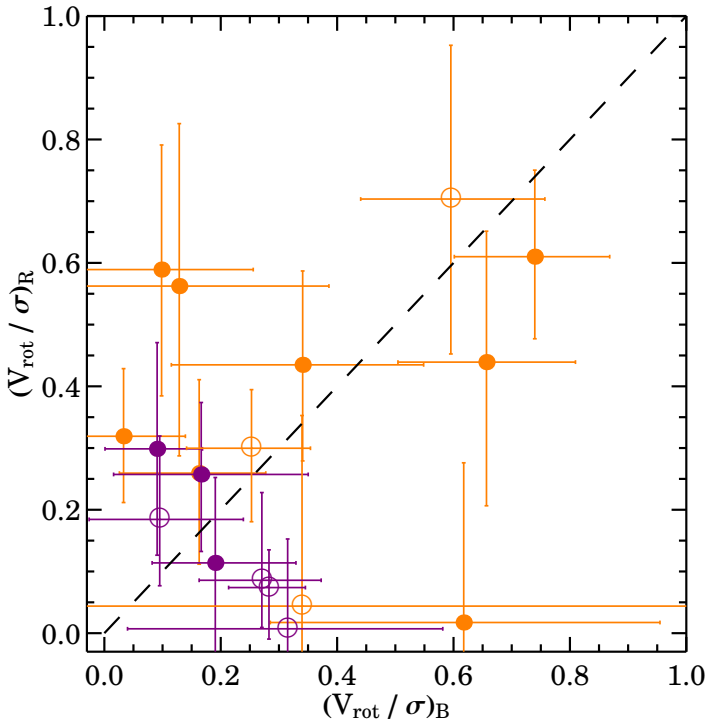

Figure 2.19 The rotational dominance parameter of GC systems. The plot compares the $(V_{\rm rot}/\sigma)$ parameter of the blue GCs $(V_{\rm rot}/\sigma)_{\rm B}$ to that of the red GCs $(V_{\rm rot}/\sigma)_{\rm R}$. The dashed line marks a one-to-one line. GC systems are colour coded according to the kinematics of the host galaxy: purple if slow-rotators and orange if fast-rotators. Filled and open circles represent our GC systems and the data from the literature, respectively.

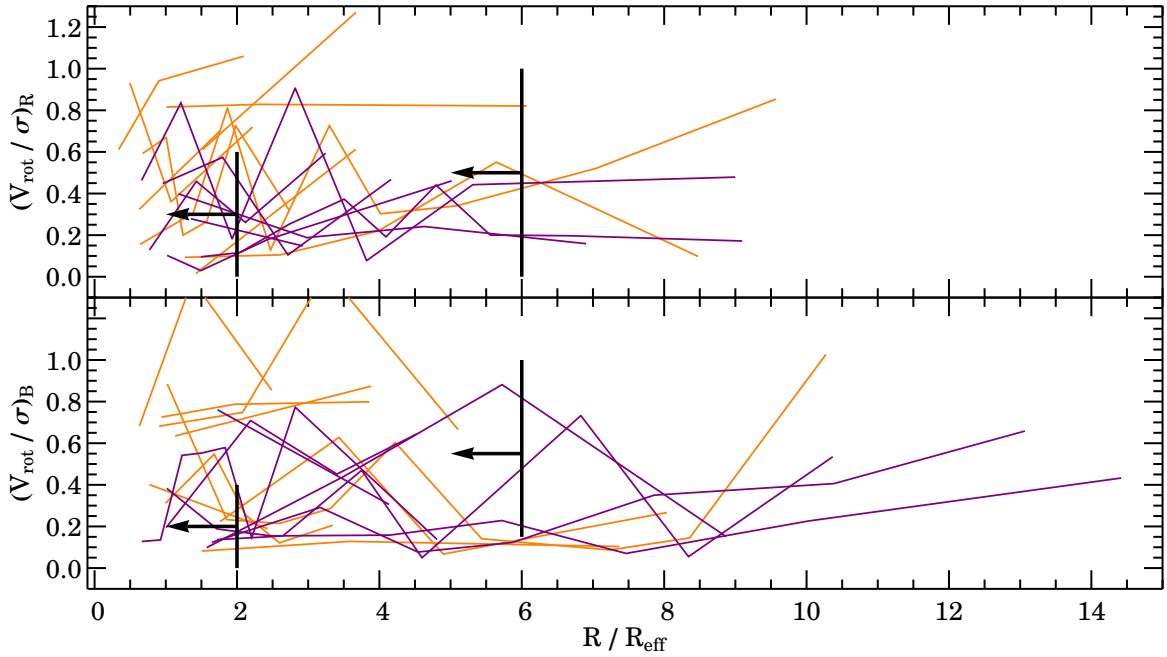

Figure 2.20 $(V_{\rm rot}/\sigma)$ radial profiles for our galaxy sample. Colours are as in Figure 2.19. The top and bottom panels show the rotational dominance parameter for the red and blue GC systems respectively. The black lines and arrows are predictions from Bekki et al. (2005) and represent the range of $(V_{\rm max}/\sigma_0)$ within 2 and 6 $R_{\rm eff}$ respectively. There is no clear trend of $(V_{\rm rot}/\sigma)$ with radius as predicted from B+05.

systems in the slow-rotator galaxies have $0 < (V_{\rm rot}/\sigma) < 0.3$. Again, we want to emphasise that this does not necessarily imply that these systems lack rotation because if their rotation occurs only in a limited radial range, it may have been smeared out in the overall $(V_{\rm rot}/\sigma)$. The GC systems in fast-rotator galaxies are more rotation-supported and in general at least one GC subpopulation has a conspicuous amount of rotation. There is a group of galaxies with $(V_{\rm rot}/\sigma) \sim 0.6$ which includes the fast-rotator galaxies with large $\lambda_{R_{\rm eff}}$, but it also includes NGC 4649 with $\lambda_{R_{\rm eff}} \sim 0.12$.

In Figure 2.20 we compare the radial $(V_{\rm rot}/\sigma)$ profiles for the blue and red GC systems with the numerical simulations of B+05. We note that B+05 quote the ratio of the maximum rotation velocity to the central velocity dispersion $(V_{\rm max}/\sigma_0)$ within 2 and 6 $R_{\rm eff}$, whereas we plot the overall $(V_{\rm rot}/\sigma)$ in each radial bin. Therefore, the predictions plotted in Figure 2.20 are typically upper limits. Another caveat is that B+05 simulate dry mergers, which leads to a systematic mismatch with the observed rotation in the galaxy centers. However, this effect is small for $R \gtrsim 2R_{\rm eff}$ (Hoffman et al., 2010), which is the radial range with better GC coverage and the most relevant for this study.

We find that for galaxies in the fast-rotator group, at least one GC subpopulation has $(V_{\rm rot}/\sigma) \neq$

0. Slow-rotator galaxies have generally slower rotating GC systems. Although the comparison with B+05 suggests an overall agreement of our results with their predictions, the scatter in both $(V_{\rm rot}/\sigma)$ and in the simulations is too large to draw any strong conclusions. In more detail, the simulations predict $(V_{\rm rot}/\sigma)$ increasing monotonically with radius but we see no evidence for this feature in our data. Moreover, a direct comparison with B+05 simulations is not possible because they did not publish the $(V_{\rm rot}/\sigma)$ profiles to $6R_{\rm eff}$. Figure 2.20 also shows that many GC systems are characterized by significant rotation spikes. These features might be partly caused by spatial incompleteness, outliers or projection effects. Alternatively, one speculative possibility is that these rotation spikes are the imprints of minor mergers. These events are expected (e.g., Vitvitska et al., 2002; Hetznecker & Burkert, 2006), and observed (e.g., Romanowsky et al., 2011), to perturb the halo kinematics of massive galaxies. Detailed studies of GC system phase-space for each galaxy are needed to quantify this effect. Norris et al. (2012) also suggested that the missing outer rotation could be explained if the reservoir of angular momentum was located beyond the radii mapped by current GC system studies. This idea would be supported by the large rotation $(V_{\rm rot}/\sigma \sim 1.0)$ we observe at $\sim 10R_{\rm eff}$ for both GC subpopulations of NGC 1407. However, at such galactocentric distances, results are uncertain because of spatial incompleteness and low number statistics. The same concerns were addressed by Strader et al. (2011) on the suspicious outer rotation $(V_{\rm rot}/\sigma \sim 0.6)$ observed in NGC 4486.

2.9.3 Kinematic misalignment

It is also important to study how the rotation of the GC systems aligns with respect to the host galaxy isophotes. An eventual position angle misalignment might contain information about the triaxiality of the system (Krajnović et al., 2011).

In Figure 2.21 we compare the PA misalignment of the blue and red GC subpopulations. For clarity, we have removed from the plot galaxies for which neither the $PA_{\rm kin}$ of the blue nor of the red GC subpopulation was constrained. A caveat here is that we study *overall* $PA_{\rm kin}$ that will be biased by kinematic twists with radius. Broadly speaking, we note that most of the galaxies are located in the bottom-left quadrant of Figure 2.21 towards $|\Delta PA| = 0$, suggesting that the red GC subpopulation rotates more consistently with the photometric major axis than the blue GC subpopulation. We do not see a sharp separation between the GC systems in fast and slow-rotator galaxies. The GC rotation in fast-rotator galaxies seems to be equally consistent with the photometric major axis for both GC subpopulations.

The B+05 simulations also predicted kinematic misalignments with respect to the galaxy isophotes, albeit with an amplitude smaller than our findings. Depending on the orbital configuration, these authors can also reproduce the minor-axis rotation for the blue and red GC subpop-

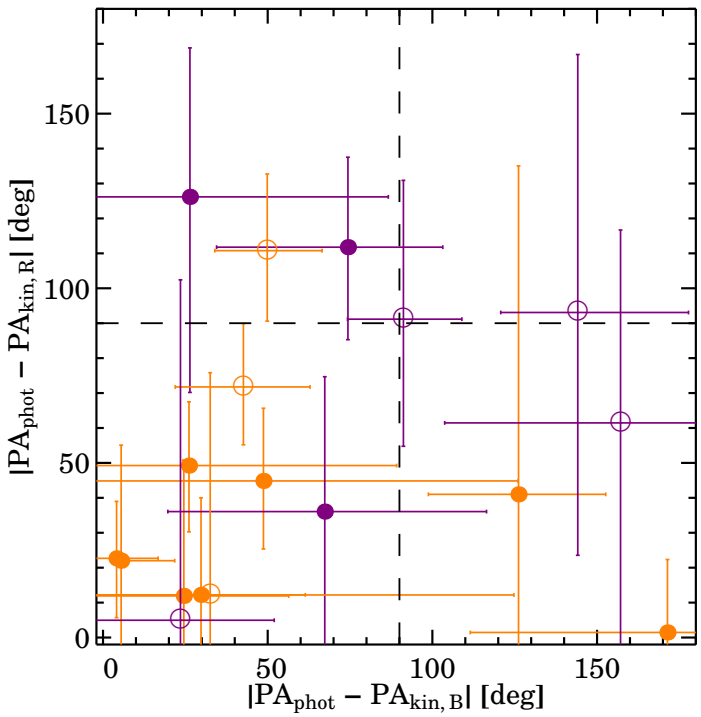

Figure 2.21 GC system position angle misalignments. The horizontal and the vertical axes show the misalignment between the photometric and the kinematic major axes for the blue and the red GC subpopulations respectively. Dashed lines mark a constant 90 degree angle. Rotation along the photometric major axis occurs at 0 deg, rotation along the minor axis at 90 deg and counter rotation at 180 deg. Galaxies with both a blue and red GC kinematic position angle unconstrained are not included for clarity. The rotation of the red GCs is more consistent with the photometric major axis.

ulations, but they do not quantify this effect. Unfortunately, B+05 do not provide radial kinematic misalignments profiles, but they find that the rotation of both GC subpopulations in the outer regions of a merger remnant should be aligned along the photometric major axis, which is in rough agreement with our findings.

2.9.4 The slope of the $V_{\rm rms}$ profile

The $V_{\rm rms}$, sometimes freely named as velocity dispersion if the contribution of the rotation is low, is related the line-of-sight kinetic energy of a galaxy per unit of mass. Its profile has been classically used to model dark matter halos. Here, instead of showing the detailed $V_{\rm rms}$ profile for our GC system sample, we think it is more convenient to parametrize these profiles and to study their overall slopes. We use a maximum-likelihood approach to fit a power-law function to the non-binned $V_{\rm rms}$ profile, similarly to that done in eq. 2.4 for the GC system kinematics. In this case the χ^2 function to be minimized is (Bergond et al., 2006):

$$\chi^2 = \sum_{i=1}^{i=N} \left[\frac{(V_{{\rm rad},i} - V_{\rm sys})^2}{V_{\rm rms}^2 + (\Delta V_{{\rm rad},i})^2} + \ln(V_{\rm rms}^2 + (\Delta V_{{\rm rad},i})^2) \right], \tag{2.7}$$

and the function to be modelled is:

$$V_{\rm rms}^2(R) = V_{\rm rms,0}^2 \times (R/R_0)^{-\gamma}, \tag{2.8}$$

where R_0 is a scale parameter, set here to the median galactocentric distance of each GC system. $V_{\rm rms,0}$ and γ are two parameters free to vary, with the latter representing the slope of the power-law: increasing if $\gamma < 0$ and decreasing if $\gamma > 0$. Uncertainties on this method were obtained by bootstrapping the sample 2000 times in order to obtain the 68 per cent confidence levels.

Bearing in mind that the shape of the profile might change with radius (see the velocity dispersion profile of NGC 1407), in Figure 2.22 we show the best fit γ for each GC subpopulation (including the combination of the two) as a function of the host galaxy magnitude. The overall slope of the $V_{\rm rms}^2$ profile (γ) of the the GC systems is generally positive, but it becomes ≤ 0 for brighter galaxies, implying a constant or even increasing $V_{\rm rms}$ profile. If we now consider the blue and red GC subpopulations separately, it is clear that this effect is caused *only* by the blue GC subpopulations in galaxies with $M_K < -25$ mag. The red GC subpopulations are always consistent with having $\gamma \geq 0$ and a linear fit to the data suggest no significant trend with the magnitude. It is not clear why we do not observe $\gamma \leq 0$ also for the red GC subpopulation. The two GC subpopulations might have different orbital configurations as a consequence of different formation histories and this would alter the shape of the $V_{\rm rms}$ profiles. Therefore, it is important

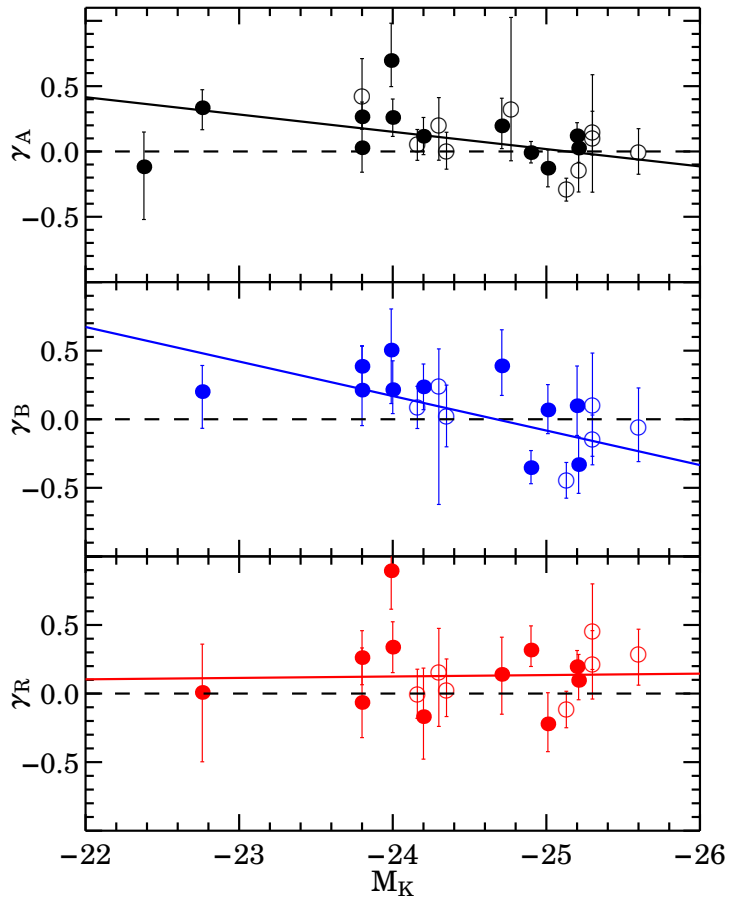

Figure 2.22 Log-slopes of the GC system $V^2_{\rm rms}$ profiles. Symbols are as in Figure 2.19. For each GC system the plot shows the best fit γ parameter to eq. 2.8 for all (top panel), blue (middle panel) and red GC subpopulation (bottom panel) as a function of the absolute magnitude M_K of the respective host galaxy. Lines are weighted linear fits to the data, whereas the dashed lines show an ideal flat $V_{\rm rms}$ profile ($\gamma = 0$). The blue GC subpopulation tends to have a decreasing $V_{\rm rms}$ slope ($\gamma < 0$) in more massive galaxies, while the red GC subpopulation has steady $\gamma \geq 0$ over the whole magnitude range.

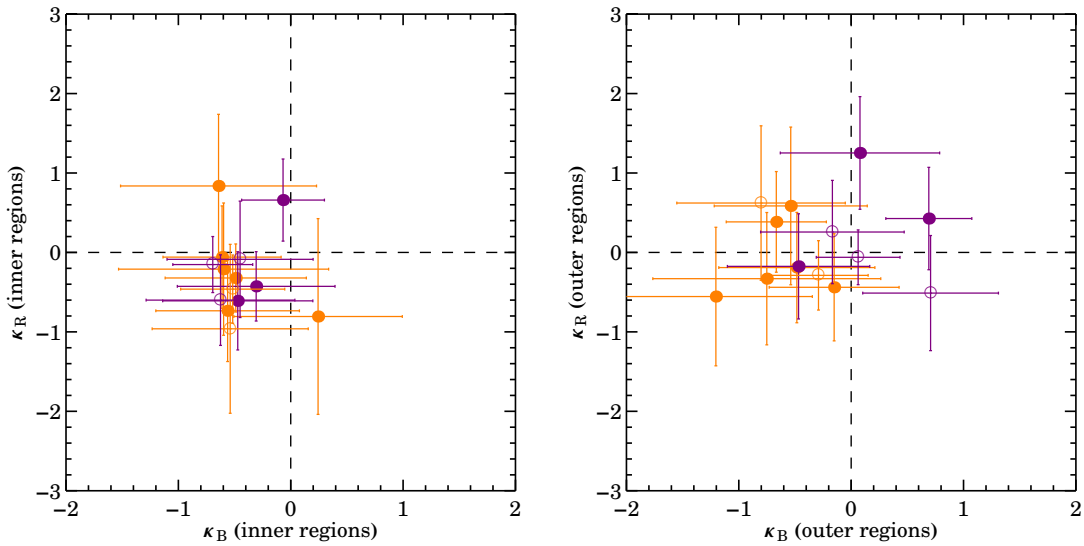

Figure 2.23 GC system velocity kurtosis. Symbols are as in Figure 2.19. The plot compares the kurtosis κ of the blue and red the GC systems in the inner (left panel) and outer radial bins (right panel). Dashed lines represent Gaussian distributions at $\kappa = 0$. GC system orbits are tangential and radial if $\kappa < 0$ and $\kappa > 0$ respectively.

also to study the orbits of the GC systems.

2.9.5 Kurtosis

The galaxy anisotropy has classically been measured through the parameter β that gives the relative ratio of the tangential to the radial velocity dispersion for a given dynamical tracer (Binney & Tremaine, 2008). The calculus of β for our GC systems is not a topic of this Chapter and we will instead keep things simple by calculating the kurtosis κ that measures the deviation of a velocity distribution from a Gaussian. In the regime of a constant velocity dispersion the kurtosis provides a rough estimate of the GC orbits. These will be will be radial ($\kappa > 0$), isotropic ($\kappa = 0$) or tangential ($\kappa < 0$), respectively. Broadly speaking we measure the fourth-order velocity moment:

$$\kappa = \frac{1}{N}\sum_{i=1}^{N}\frac{(V_{\rm rad,i} - V_{\rm sys})^2}{V_{\rm rms}^4} - 3 \pm \sqrt{\frac{24}{N}}, \tag{2.9}$$

but in practice we will use a more complicated bias-corrected formula from Joanes & Gill (1998).

We divide the radial kurtosis profiles in two radial bins in order to have roughly the same number of GCs in each bin. In this case the required number of GC radial velocities per bin is larger because the uncertainties are $\propto N^{1/2}$. We require at least 30 GCs per bin and this excludes smaller galaxies like NGC 1400 or NGC 821. As the calculation of κ does not take the GC radial

velocity uncertainties into account, a bias might be present due to the different velocity resolution of the literature and of our GC samples. Results are presented in Figure 2.23.

We find that in the innermost bin most of the GC systems have $\kappa_B \leq 0$ and $\kappa_R \leq 0$, suggesting isotropic or even tangential orbits. This is also true for kurtosis in the outer bin, but some galaxies (such as NGC 4365, NGC 4486 and NGC 4472) have the tendency of having more radially-biased orbits. In all cases the kurtosis of the blue and red GCs are consistent with isotropic orbits.

2.10 Discussion

2.10.1 GC kinematic bimodality

The origin of GC colour bimodality is still an area of debate. On the theoretical side, there is a lack of consensus regarding the leading processes that drive the formation of GC systems (i.e. merging, collapse, accretion) and whether one (see Muratov & Gnedin, 2010) or more of these processes (e.g., Lee et al. 2010b) are needed to explain the observed colour bimodality. The contrasting numerical predictions are in part due to the diverse recipes with which simulations were built (Bekki et al., 2005, 2008; Moore et al., 2006; Kravtsov & Gnedin, 2005; Diemand et al., 2005), but they might also reflect a real diversity of formation mechanisms that built up the GC systems in the first place.

On the observational side, the GC colour bimodality has been generally accepted because the two colour subpopulations differ in mean size and spatial distribution, and they depend differently on host galaxy properties (Forbes et al., 1997a; Peng et al., 2006). Recently, the colour bimodality itself has been claimed to be an artifact of a strongly non-linear colour-metallicity relation (Yoon et al., 2006, 2011a), which would make the metallicity distribution of a GC system unimodal, skewed towards metal-poor metallicities. The resulting metallicity distribution function would be more metal-rich than the one classically obtained with linear, or broken linear, colour-metallicity relations (Peng et al., 2006; Faifer et al., 2011; Sinnott et al., 2010; Alves-Brito et al., 2011).

We have found that GC systems around most of the surveyed galaxies have different kinematics between the blue and red sides of their GC colour distribution. This includes different kinematic position angle, rotation amplitudes and velocity dispersions. The kinematics generally change smoothly with the GC colour, but we also observe cases in which there is a sharp kinematic transition corresponding to the blue-red dividing colour (see NGC 821, NGC 1407 and NGC 3377 in Figure 2.12). *Our kinematic results are therefore strong evidence against colour bimodality simply being a consequence of a strong non-linear colour-metallicity relation.*

Most of the surveyed galaxies have small, yet significant, blue/red kinematic diversity (especially in their velocity dispersion profiles). The fact that we do not see any sharp kinematic

transition with colour in all galaxies is not surprising because these systems lack intrinsic rotation of both GC subpopulations. Therefore, the rotation amplitude of GC systems can be insensitive for testing kinematic bimodality, especially for massive galaxies, for which one has instead to rely on other proxies such as the slope of the $V_{\rm rms}$ profile (Figure 2.22).

2.10.2 The star-GC system connection

Although the link between the red GCs and the host galaxy was somewhat expected from their similar spatial distributions, its kinematic confirmation was limited to a handful of galaxies (Schuberth et al., 2010; Norris et al., 2012; Romanowsky et al., 2009; Strader et al., 2011). The results that we found for our galaxy sample are diverse in this regard.

On one side we find excellent agreement between the kinematics of the stars (and/or PNe) and that of the red GCs, indicating that the coupling between stars and GC systems holds also for less massive galaxies. On the other hand, we have also found galaxies in which the blue GCs behave as the galaxy stars or, more interestingly, as the PNe. NGC 3377 and NGC 821 are two examples. These are very similar field disk galaxies with a falling stellar rotation curve. However, the blue GCs in NGC 3377 do not rotate and are decoupled from the PNe. Conversely, in NGC 821 blue GCs mimic the minor axis rotation of the PNe, but not of the stars. What is most surprising in the latter case is indeed the fact that the PNe are decoupled from the stars as well. Based on stellar population inferences, Proctor et al. (2005) concluded that NGC 821 has undergone a minor merger or tidal interaction in the last 4 Gyr. Our results would support this scenario. However, it remains to be explained why the PNe are not akin to the underlying stars and how this feature can influence the dark matter estimate of this galaxy (Romanowsky et al., 2003).

How the star-GC system connection arose in the early times is still an open debate. Galaxy mergers may contribute to building the GC system of the remnant. Bekki et al. (2002) have shown that tidal shocks induced by galaxy merging can compress giant molecular clouds to form both new metal-rich GCs and stars. However, based on stellar population studies, Forbes et al. (2007) have shown that most of the red GCs are consistent with being uniformly old, and few, if any, formed in late epoch gaseous mergers.

A possible consensus scenario may arise from the idea that part of the red GCs might have formed during the early turbulent phases of galaxy formation at $z \sim 2$ (Kravtsov & Gnedin, 2005; Shapiro et al., 2010). At this redshift, galaxies are characterised by fast rotating thick discs (Elmegreen et al., 2009) fragmented into super-star forming clumps. Observations have shown that the origin of these clumps is related to disc instability processes (Wisnioski et al., 2011), but they may be also caused by cold flows (Dekel et al., 2009). It is thought that these gas-rich clumps migrate inwards to feed the nascent bulge (dragging along newly formed metal-rich GCs) and

losing their rotational motion to dynamical friction, finally acquiring a typical $V_{\rm rot}/\sigma < 1$ for the bulge. During this migration, $\sim 50\%$ of the clump mass will be stripped off and it will end up forming a rotationally supported disk (Bournaud et al., 2007).

This formation mechanism seems to qualitatively explain the spatial and kinematic similarity between stars and red GCs. However, as far as we know, no numerical simulations have to date been produced to directly compare observations with the kinematics of the red GCs forming during the 'gas-rich clump-driven phase'. Also, the study of dwarf ellipticals in the Virgo cluster (Beasley et al., 2009) and in the Sculptor group (Olsen et al., 2004) suggested that disks may have been significant sites of GC formation at early times.

The poor radial overlap between studies of galaxy stars and GC systems complicates the kinematic comparison between these two. Extended stellar kinematic studies, a la Proctor et al. (2009), will help to test the galaxy star-GC system connection. Also, it will be interesting to see what is the role of the PNe in this scenario and if the PNe-GCs connection in NGC 821 is the rule rather than the exception.

2.10.3 Orbital anisotropy

The GC orbital anisotropy, in this context represented by the kurtosis κ, can provide other clues about the formation of GC bimodality. Theoretical studies predict that dark matter haloes, including the baryonic tracers within them, have radially-biased orbits in their outer regions (McMillan et al., 2007; Prieto & Gnedin, 2008; Dekel et al., 2005). However, the small number of studies in this field, which have usually employed deep integrated stellar light and PNe, seems to suggest that early-type galaxies harbour quasi-isotropic orbits (Gerhard et al., 1998; Douglas et al., 2007; de Lorenzi et al., 2009; Napolitano et al., 2009, 2011; Deason et al., 2011). How does this compare to the GC anisotropy?

Our analysis suggests that in the inner regions both GC subpopulations have isotropic or tangential orbits, whereas in the outer regions there is a hint that some red GC systems might have radial orbits. We recognise that in both cases the GC orbits are still consistent with being isotropic.

As already pointed out by Romanowsky et al. (2009), the lack of radially-biased orbits for the blue GC subpopulation might be connected to the evolutionary history of the GC system within the galaxy. Processes such as evaporation, dynamical friction and the consequent disruption of GCs may change the anisotropy. The disruption of GCs will be more efficient for those on radial orbits because they plunge deepest into the galaxy centre (Baumgardt, 1998; Baumgardt & Makino, 2003). Accordingly, they will become less luminous and eventually vanish altogether, making GCs on tangential and isotropic orbits the most likely ones to survive and be observed today.

The GC orbital anisotropy will need further in-depth investigation but the overall pattern sug-

gests that, if the blue GCs formed from the accretion or minor merger of satellite galaxies, some disruption effects have to be taken into account to explain the general absence of blue GC on radially-biased orbits. The scenario discussed above supports the idea that present day blue GCs were brought into the host galaxy via accretion and/or minor mergers.

The key point here is that the different GC orbits mean that the resulting $V_{\rm rms}$ profiles will be shaped by the orbits themselves (the mass-anisotropy degeneracy). Tangential anisotropy, for example, could mimic the presence of dark matter, whereas radial anisotropy could deplete it. Interestingly, we find that the blue GC subpopulations with tangentially-biased orbits tend to have increasing $V_{\rm rms}$ profiles (suggesting a more dominant dark-matter halo), whereas the red GC subpopulation is consistent with having a decreasing $V_{\rm rms}$ profile and more radial orbits. It will be interesting to test how a classic Jeans analysis that makes use of the different GC anisotropies found in this Chapter compares with recent studies that do not require assumptions on the dark matter halo (Walker & Peñarrubia, 2011).

2.10.4 NGC 7457: a case study for the formation of S0s

GC systems have been exploited to study the unsolved conundrum of the formation of lenticular galaxies (Barr et al., 2007; Arnold et al., 2011). In fact, it is still not clear whether S0s are quenched spirals: the remnant of a gentle gas shut off process that would preserve the kinematic signature of the progenitor spiral (Byrd & Valtonen, 1990; Williams et al., 2010), or very disky ellipticals: the products of violent merging events (Bekki, 1998; Cretton et al., 2001) that would diminish the original disk-rotation. The observational differences between these two scenarios are minimal and it also depends upon the galaxy environment (Kormendy & Bender, 2012). S0s might still be rotationally supported if they form in uneven-mass galaxy mergers, with mass-ratio ratio between 1:4.5 and 1:10 (Bournaud et al., 2005).

In this context, a particularly interesting case study is offered by NGC 7457 that we have discussed in §2.5.9. This nearby lenticular galaxy contains in fact both signatures of a recent merger (Chomiuk et al., 2008) and a disky GC kinematics with a possible counter-rotating core in the innermost regions (Sil'chenko et al., 2002). In Figure 2.24 we compare the $V_{\rm rot}/\sigma$ profile of the stars (Simien & Prugniel, 2000) and of our GC measurements (including the dataset of Chomiuk) with N-body simulations of merging with different mass-ratios of 1:3 (Cretton et al., 2001) and 1:10 (Bournaud et al., 2005), respectively. To do this, we select all the GCs within 1 arcmin from the photometric major axis and we construct two bins of 8 objects each.

Results in Figure 2.24 show that our data are in good agreement with the 1:10 remnant, even though the discrepancies occurring at small and large radii seem to suggest that the mass-ratio involved in the formation of this galaxy was probably smaller than this value. These results, along

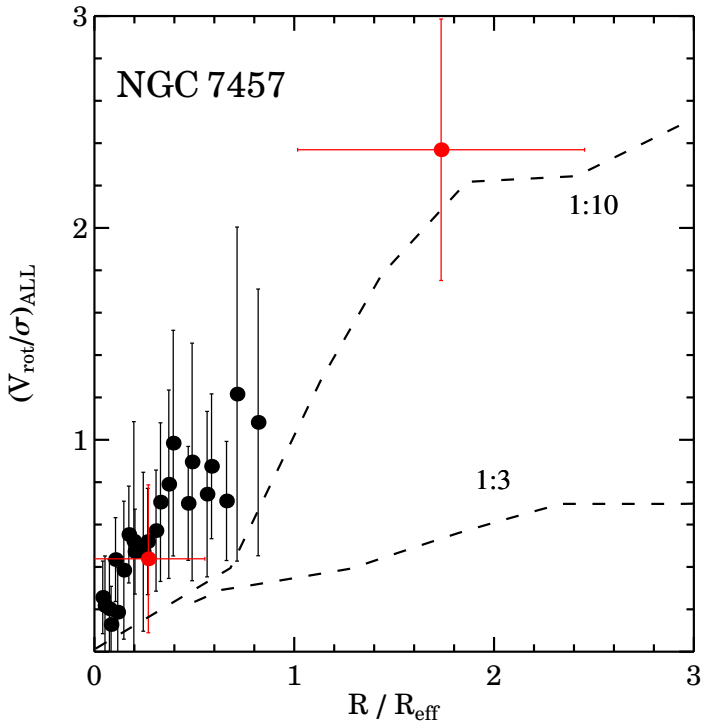

Figure 2.24 GC rotation rate in NGC 7457. GC data from this work (supplemented with Chomiuk et al. 2008) and long–slit data from Simien & Prugniel (2000) are shown as red and black points respectively. Also shown are the simulated merger remnant with a 1:10 (top dashed line) and 1:3 (bottom dashed line) mass ratio from Bournaud et al. (2005) and Cretton et al. (2001), respectively. Typical uncertainties on the merger remnant profiles are 15% at 4 $R_{\rm eff}$.

with the counter-rotating core in the centre and the intermediate-age GCs, seem to favour the minor merger scenario. We also note that the S0 galaxies simulated in B+05 are characterised by a strong rotation of the blue GC subpopulation if formed via merging, but we do not see any significant change of the GC kinematics with the GC colour in NGC 7457. This effect could indeed be real, but it could also be driven by the low number statistics or by the large uncertainties (± 0.2 mag) due to the conversion from *HST* to WIYN magnitudes.

2.11 Summary and Conclusions

We have examined the GC systems in twelve early-type galaxies (from lenticular to large ellipticals over a range of galaxy mass), nine of which published for the first time, with particular emphasis on the kinematics of their blue and red GC subpopulations.

For the newly-presented data, we have used wide-field ground-based imaging (mainly from Subaru/Suprime-cam) and *HST* observations, finding that eight out of nine galaxies have a significant bimodal GC colour distribution. The study of the spatial distribution of these two subpopulations has revealed that red GCs are generally more centrally concentrated and that they have a slope similar to the surface brightness of the underlying galaxy. This is in agreement with the idea that red and blue GC subpopulations trace the spheroidal component and the halo component of the host galaxies, respectively.

Multi-object spectroscopy was performed for a bright sample of GCs using Keck/DEIMOS that provided an average velocity resolution of ~ 15 km s^{-1} (a factor of 3 better than most previous studies). We find a variety of kinematic profiles for both the blue and the red GC subpopulations. The salient results are:

1. The GC kinematics (rotation amplitude, velocity dispersion and rotation axis) varies with GC mean colour. In particular, we find GC systems which have a sharp kinematic transition at the blue-red dividing colour, implying that the GC colour bimodality is real and extends to kinematic bimodality.

2. The rotation velocity and velocity dispersion of the red GC subpopulation mimics the host galaxy stellar kinematics (including those of planetary nebulae). This property supports the scenario in which the red GCs form together with the bulk of stars of the host galaxy, for instance during the 'turbulent disk phase' at high redshift. The rotation of the blue GCs is typically consistent with zero, but their velocity dispersion is always higher or equal to that of the red GCs, especially in the outer regions.

3. The GC kinematics combined with other kinematic studies can reveal interesting features.

We have found that the blue GCs in NGC 821 mimic the minor axis rotation of the PNe, but not that of the stars, suggesting that there might be a blue GC-PNe connection that trace a recent merging event. Also, our data seem to be consistent with the idea that the S0 galaxy NGC 7457 was formed via a minor merger with a 1:10 mass ratio.

We have supplemented our dataset with ten additional GC systems from the literature and compared their kinematics to host galaxy properties. We have compared our results with numerical simulations, finding no strong evidence that GC systems have formed via major-mergers. We find that the correlation between the $V_{\rm rms}$ of the GC systems and the mass of the host galaxy (from lenticular to massive ellipticals) holds for less massive galaxies and that it is tighter for the red GC subpopulation. The blue GCs in more massive galaxies have increasing $V_{\rm rms}$ profiles, whereas the red GCs have always shallower $V_{\rm rms}$ profiles. A study of the GC velocity kurtosis, suggests that blue GCs generally appear to be isotropic or tangentially-biased in the outer regions, unlike the red GCs which instead have more radially-biased orbits.

3

Supermassive black hole correlations with bulges and haloes: investigating globular cluster system velocity dispersions

Understanding whether the bulge or the halo provides the primary link to the growth of supermassive black holes has strong implications for galaxy evolution and supermassive black hole formation itself. In this Chapter, we approach this issue by investigating extragalactic globular cluster (GC) systems, which can be used to probe the physics of both the bulge and the halo of the host galaxy. We study the relation between the supermassive black hole masses ($M_{\rm BH}$) and the globular cluster system velocity dispersions ($\sigma_{\rm GC}$) using an updated and improved sample of 21 galaxies. We exploit the dichotomy of globular cluster system colours, to test if the blue and red globular clusters correlate differently with black hole mass. This may be expected if they trace the potentially different formation history of the halo and of the bulge of the host galaxy respectively.

Recently, Sadoun & Colin (2012) (hereafter SC12), have examined the correlation between the GC system velocity dispersion and $M_{\rm BH}$ for twelve galaxies, including the Milky Way. Their results suggest a tight correlation between $M_{\rm BH}$ and the velocity dispersion for both the red and blue GC subpopulations, with an intrinsic scatter ϵ always $\leq$ 0.33 dex, indicating a very tight correlation. They also find that the red GCs are more closely correlated ($\epsilon = 0.22$ dex) with $M_{\rm BH}$ than the blue GCs ($\epsilon = 0.33$ dex).

With our improved galaxy sample, we still find a strong correlation between $M_{\rm BH}$ and the total GC system velocity dispersion, although not as strongly as claimed by the recent work of Sadoun & Colin. We also examine the $M_{\rm BH} - \sigma_{\rm GC}$ relation for barred/bar-less and core/non-core galaxies, finding no significant difference, and for the first time we quantify the impact of radial gradients in the GC system velocity dispersion profile on the $M_{\rm BH} - \sigma_{\rm GC}$ relation. We additionally predict $M_{\rm BH}$ in 13 galaxies, including dwarf elliptical galaxies and the cD galaxy NGC 3311. We

conclude that our current results cannot discriminate between the bulge/halo scenario. Although there is a hint that the red GC velocity dispersion might correlate better with $M_{\rm BH}$ than the blue GC velocity dispersion, the number statistics are still too low to be certain.

3.1 Galaxy sample

We study a subset of galaxies with direct $M_{\rm BH}$ measurements and with more than ten GC radial velocity measurements. From the literature, we compiled a list of 13 galaxies. This includes all the galaxies discussed in SC12, excluding the Milky Way, and two additional galaxies: NGC 253 (Olsen et al., 2004) and NGC 3585 (Puzia et al., 2004), not studied by SC12 because the uncertainties on the GC velocity dispersion were not quoted in the parent papers. The Milky Way is not included in this study because the results of Côté (1999) suggest that the still uncertain velocity dispersion of the Milky Way GC system is unusually large for its black hole mass. Moreover, the fact that the Milky Way GC analysis is carried out in three-dimensions rather than in projection, makes the comparison with other galaxies not straightforward. We also update the GC catalogue used by SC12 for NGC 4594 with the latest compilation of Alves-Brito et al. (2011). We note that SC12 used $M_{\rm BH}$ values from Gültekin et al. (2009b) although more recent $M_{\rm BH}$ were sometimes available.

For NGC 224 (M31) we use the GC system velocity dispersion measurements from Lee et al. (2008a), because their catalogue is not available on-line.

In regard to NGC 253, there are two public GC catalogues for this galaxy: Beasley & Sharples (2000) and Olsen et al. (2004), for a total 38 GCs. However, we were unable to find a reliable calibration offset between the radial velocities of the four GCs in common between these two datasets. We decided to use the Olsen catalogue only, because it is larger in size (24 GCs) than Beasley's dataset (14 GCs).

The biggest strength of our data set is the addition of a further 9 new early-type galaxies from the SLUGGS survey, one of which (NGC 4486) was already discussed in SC12. We use the most recent black hole mass measurements as summarized in McConnell & Ma (2012) and Graham & Scott (2012). This gives us a sample of 21 galaxies, nearly double the number used by SC12, which are listed in Table 3.1.

Galaxy [NGC] (1)	Type (2)	D [Mpc] (3)	$M_{\rm BH}$ [$10^8 M_\odot$] (4)	σ_* [km s^{-1}] (5)	Core (6)	σ_A [km s^{-1}] (7)	σ_B [km s^{-1}] (8)	σ_R [km s^{-1} (9)	$v_{\rm GC}$ [km s^{-1}] (10)	$v_{\rm GC,B}$ [km s^{-1}] (11)	$v_{\rm GC,R}$ [km s^{-1}] (12)	Ref. (13)
0224	Sb	0.73	$1.4^{+0.8}_{-0.3}$	160 ± 8	n	134^{+5}_{-5}	129^{+8}_{-6}	121^{+9}_{-10}	178^{+4}_{-4}	183^{+5}_{-5}	154^{+11}_{-9}	1
0253	SBc	3.5	$0.1^{+0.05}_{-0.1}$	109 ± 10	n	37^{+6}_{-7}	–	–	58^{+16}_{-13}	–	–	2
0524	S0	24.2	$8.6^{+1.0}_{-0.4}$	235 ± 10	y	175^{+15}_{-15}	167^{+23}_{-27}	164^{+27}_{-33}	192^{+36}_{-26}	202^{+52}_{-34}	174^{+61}_{-37}	3
1316	SB0	21.0	$1.7^{+0.3}_{-0.3}$	226 ± 11	y	168^{+38}_{-41}	–	–	217^{+43}_{-28}	–	–	4
1399	E1	19.4	$4.7^{+0.6}_{-0.6}$	296 ± 15	y	293^{+7}_{-8}	321^{+12}_{-12}	269^{+9}_{-10}	296^{+8}_{-8}	325^{+13}_{-12}	266^{+10}_{-9}	5
3031	Sab	4.1	$0.9^{+0.20}_{-0.11}$	143 ± 7	n	120^{+8}_{-9}	124^{+13}_{-13}	99^{+8}_{-8}	139^{+11}_{-10}	131^{+16}_{-13}	145^{+17}_{-13}	6
3379[a]	E1	10.7	$4.2^{+1.0}_{-1.1}$	206 ± 10	y	184^{+15}_{-14}	–	–	173^{+26}_{-19}	–	–	7/8
3585	S0	20.6	$3.3^{+1.5}_{-0.6}$	213 ± 10	n	158^{+20}_{-22}	–	–	159^{+35}_{-23}	–	–	9
4472[a]	E2	16.7	25^{+6}_{-1}	315 ± 16	y	303^{+15}_{-13}	333^{+19}_{-20}	261^{+18}_{-18}	305^{+15}_{-14}	334^{+22}_{-19}	256^{+22}_{-19}	10
4594[a]	Sa	10.0	$6.7^{+0.5}_{-0.4}$	230 ± 12	y	229^{+10}_{-10}	238^{+13}_{-14}	208^{+13}_{-13}	225^{+11}_{-10}	239^{+17}_{-14}	208^{+16}_{-13}	11
4649[a]	E2	16.5	47^{+11}_{-10}	335 ± 17	y	206^{+13}_{-13}	194^{+14}_{-16}	228^{+28}_{-28}	228^{+17}_{-15}	213^{+21}_{-17}	257^{+37}_{-26}	12
5128[a]	S0	4.1	$0.59^{+0.11}_{-0.10}$	150 ± 7	n	121^{+4}_{-4}	118^{+5}_{-5}	123^{+6}_{-6}	121^{+5}_{-4}	116^{+7}_{-6}	125^{+7}_{-6}	13
0821[a]	E6	23.4	$1.7^{+0.7}_{-0.7}$	209 ± 10	n	151^{+13}_{-13}	129^{+19}_{-20}	162^{+20}_{-19}	150^{+17}_{-12}	145^{+25}_{-17}	154^{+26}_{-17}	14
1023	SB0	10.5	$0.4^{+0.04}_{-0.04}$	204 ± 10	n	141^{+10}_{-10}	139^{+15}_{-16}	139^{+16}_{-18}	152^{+15}_{-12}	146^{+21}_{-15}	160^{+26}_{-18}	18
1407	E0	29.0	47^{+7}_{-5}	274 ± 14	y	222^{+8}_{-8}	231^{+11}_{-11}	210^{+11}_{-10}	223^{+9}_{-8}	231^{+13}_{-11}	215^{+12}_{-10}	14
3115	S0	9.5	$8.9^{+5.1}_{-2.7}$	230 ± 11	n	153^{+7}_{-7}	152^{+9}_{-8}	150^{+10}_{-10}	162^{+9}_{-8}	166^{+13}_{-11}	158^{+13}_{-10}	15
3377[a]	E5	11.0	$1.9^{+1.0}_{-1.0}$	145 ± 7	n	91^{+5}_{-6}	99^{+7}_{-7}	78^{+8}_{-8}	100^{+7}_{-6}	105^{+11}_{-8}	94^{+10}_{-8}	14
4473[a]	E5	15.2	$0.89^{+0.45}_{-0.44}$	190 ± 9	n	147^{+9}_{-9}	134^{+11}_{-11}	162^{+14}_{-16}	148^{+13}_{-10}	135^{+15}_{-11}	170^{+28}_{-19}	16
4486[a]	E1	16.7	62^{+3}_{-4}	334 ± 10	y	327^{+12}_{-10}	336^{+16}_{-17}	293^{+27}_{-25}	328^{+14}_{-12}	337^{+16}_{-14}	296^{+28}_{-22}	17
5846	E0	24.2	$10.7^{+1.9}_{-1.9}$	237 ± 10	y	235^{+17}_{-18}	269^{+17}_{-18}	201^{+13}_{-13}	235^{+12}_{-11}	268^{+21}_{-17}	203^{+15}_{-12}	14
7457[a]	S0	12.2	$0.087^{+0.052}_{-0.052}$	67 ± 3	n	40^{+8}_{-9}	–	–	68^{+12}_{-9}	–	–	14

Table 3.1 Galaxy sample. Galaxy NGC names (1) and Hubble types (2) are from NED database. Galaxy distances (3), SMBH masses (4) and stellar velocity dispersions (5) are from McConnell & Ma (2012) and references therein. If not in McConnell & Ma (2012): distances were obtained by subtracting 0.06 mag (Mei et al., 2007) to the distance modulus from Tonry et al. (2001); central stellar velocity dispersions are weighted values from HyperLeda; $M_{\rm BH}$ are from Oliva et al. (1995) and Hu (2008) for NGC 253 and NGC 5846 respectively. (6) is the presence of a core in the galaxy inner surface brightness profile. Column (7), (8) and (9) are the rotation-subtracted velocity dispersion for all, blue and red GCs respectively. Column (10), (11) and (12) are the root-mean square velocity for all, blue and red GCs respectively. GC references (13) : 1, Lee et al. (2008a); 2, Olsen et al. (2004); 3, Beasley et al. (2004); 4, Goudfrooij et al. (2001); 5, Schuberth et al. (2010); 6, Nantais & Huchra (2010); 7, (Pierce et al., 2006); 8, (Bergond et al., 2006); 9, Puzia et al. (2004); 10, Côté et al. (2003); 11, Alves-Brito et al. (2011); 12, Hwang et al. (2008); 13, Woodley et al. (2010); 14, Pota et al. (2013); 15, Arnold et al. (2011); 16, Foster et al. (in prep.); 17, Strader et al. (2011); 18, Pota et al. in prep. GC system velocity dispersion values for NGC 224 are from Lee et al. (2008a). Galaxies with updated $M_{\rm BH}$ measurements after Gültekin et al. (2009a) are marked with (a).

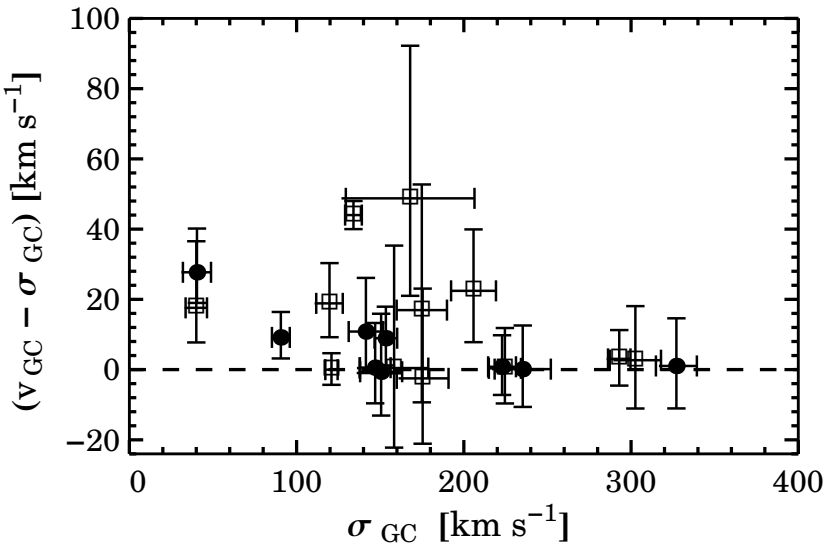

Figure 3.1 Difference between the rotation-subtracted velocity dispersion $\sigma_{\rm GC}$ and the rotation-included velocity dispersion $v_{\rm GC}$ without any colour split. Filled points and empty squares are the data from the SLUGGS survey and the literature respectively. The two quantities are generally consistent with each other, but they disagree by up to ~ 40 km s^{-1} in systems with significant rotation.

3.2 Method

3.2.1 The globular cluster system velocity dispersion

The stellar velocity dispersion, σ_*, used in the $M_{\rm BH} - \sigma_*$ relation is usually defined either as the luminosity-weighted velocity dispersion within $1/8^{\rm th}$ of an effective radius R_e, or within 1 R_e (σ_e), and/or as the central velocity dispersion (σ_0). Although they represent physically distinct quantities, σ_e and σ_0 have been reported to be consistent with each other (Gültekin et al., 2009b). This stems from the fact that the velocity dispersion profiles vary only weakly within these regions (e.g., Emsellem et al., 2011).

The detection of extragalactic globular clusters occurs predominantly at $R \geq R_e$. Therefore none of the stellar velocity dispersion quantities are directly recovered with GC data. We define the GC system velocity dispersion in two different ways, which are similar to the quantities used for stellar data. This also takes into account that some GC systems can have a rotation component which is as large as that of the random motions (Beasley et al., 2006).

The first quantity, $\sigma_{\rm GC}$, assumes a Gaussian velocity distribution and it is defined as the standard deviation with respect to the model function (Côté et al., 2001):

$$v(\theta) = v_{\rm sys} + v_{\rm rot} \sin(\theta_0 - \theta), \tag{3.1}$$

which measures the GC rotation amplitude $v_{\rm rot}$ as a function of the azimuth θ, with θ_0 being the direction of the angular momentum vector and $v_{\rm sys}$ being the systemic velocity of the host galaxy. We use a variation on Equation 3.1, originally designed by Krajnović et al. (2006) for IFU datacubes and then extended to sparsely sampled data by Proctor et al. (2009). We then minimise a χ^2 function (see Bergond et al. 2006) to compute the best fit parameters $(v_{\rm rot}, \sigma_{\rm GC}, \theta_0)$. Uncertainties were derived by bootstrapping the sample 1000 times to derive 68 per cent confidence intervals. We will refer to the rotation-subtracted velocity dispersion of the *red*, *blue* and *all* GCs as $\sigma_{\rm GC,R}$, $\sigma_{\rm GC,B}$, $\sigma_{\rm GC}$ respectively.

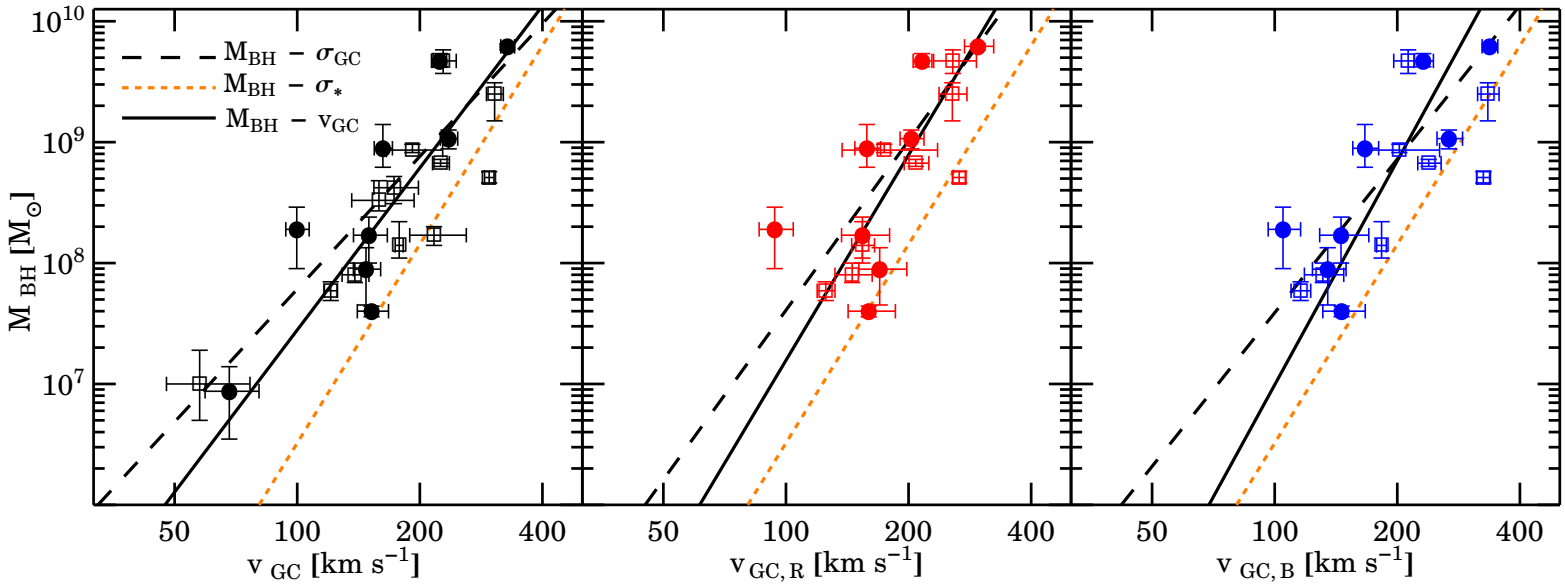

Figure 3.2 Black hole mass as a function of rotation-included GC system velocity dispersion. Left, central and right panels show the $M_{\rm BH} - v_{\rm GC}$ relation for all, red and blue GCs respectively. Data from the literature and from the SLUGGS survey are shown as open squares and filled points respectively. The black solid line is the best fit to the $M_{\rm BH} - v_{\rm GC}$ relation. The dashed lines are the best-fit to the $M_{\rm BH} - \sigma_{\rm GC}$ relations (whose datapoints are not plotted here for clarity). The slope and the intercept of the best-fit lines are the average between the values from the forward and inverse regression (see Table 3.2). The dotted-orange line is the stellar $M_{\rm BH} - \sigma_*$ relation from the average between the forward and the inverse regression from Graham et al. (2011): $\alpha = 8.14 \pm 0.05$ and $\beta = 5.54 \pm 0.40$.

		FORWARD REGRESSION				INVERSE REGRESSION			
Sample	N	α	β	ϵ [dex]	Δ	$\alpha = -\alpha_{\rm inv}/\beta_{\rm inv}$	$\beta = 1/\beta_{\rm inv}$	$\epsilon = \epsilon_{\rm inv}/\beta_{\rm inv}$ [dex]	Δ
$M_{\rm BH} - \sigma_{\rm GC}$	21	$8.76^{+0.11}_{-0.11}$	$3.22^{+0.48}_{-0.33}$	$0.42^{+0.06}_{-0.09}$	0.41	$8.86^{+0.13}_{-0.12}$	$4.35^{+1.02}_{-0.61}$	$0.48^{+0.07}_{-0.11}$	0.51
$(M_{\rm BH} > 10^7 M_\odot) - v_{\rm GC}$	19	$8.75^{+0.11}_{-0.11}$	$3.85^{+0.93}_{-0.76}$	$0.43^{+0.10}_{-0.06}$	0.44	$8.80^{+0.14}_{-0.13}$	$6.18^{+1.37}_{-0.97}$	$0.54^{+0.08}_{-0.13}$	0.57
$M_{\rm BH} - v_{\rm GC}$	21	$8.75^{+0.11}_{-0.10}$	$3.74^{+0.59}_{-0.46}$	$0.40^{+0.09}_{-0.06}$	0.42	$8.83^{+0.12}_{-0.12}$	$5.16^{+0.91}_{-0.62}$	$0.47^{+0.07}_{-0.12}$	0.52
$(M_{\rm BH} > 10^7 M_\odot) - \sigma_{\rm GC}$	19	$8.83^{+0.12}_{-0.10}$	$3.59^{+0.84}_{-0.66}$	$0.41^{+0.10}_{-0.06}$	0.42	$8.93^{+0.15}_{-0.13}$	$5.63^{+1.18}_{-0.88}$	$0.52^{+0.07}_{-0.12}$	0.53
$M_{\rm BH} - \sigma_*$	21	$8.46^{+0.07}_{-0.10}$	$4.44^{+0.74}_{-0.50}$	$0.35^{+0.08}_{-0.05}$	0.37	$8.44^{+0.08}_{-0.11}$	$5.48^{+1.08}_{-0.68}$	$0.39^{+0.06}_{-0.09}$	0.42
$M_{\rm BH} - \sigma_{\rm GC,B}$	16	$8.75^{+0.14}_{-0.12}$	$3.45^{+0.63}_{-0.63}$	$0.47^{+0.07}_{-0.12}$	0.46	$8.82^{+0.19}_{-0.16}$	$5.37^{+1.14}_{-0.86}$	$0.58^{+0.09}_{-0.15}$	0.59
$M_{\rm BH} - v_{\rm GC,B}$	16	$8.73^{+0.13}_{-0.11}$	$3.50^{+0.72}_{-0.68}$	$0.45^{+0.07}_{-0.12}$	0.45	$8.75^{+0.16}_{-0.15}$	$5.53^{+1.17}_{-0.87}$	$0.56^{+0.09}_{-0.16}$	0.57
$M_{\rm BH} - \sigma_{\rm GC,R}$	16	$8.87^{+0.14}_{-0.12}$	$3.77^{+0.93}_{-0.64}$	$0.47^{+0.07}_{-0.13}$	0.47	$9.02^{+0.14}_{-0.16}$	$5.98^{+1.51}_{-1.07}$	$0.60^{+0.10}_{-0.16}$	0.60
$M_{\rm BH} - v_{\rm GC,R}$	16	$8.85^{+0.12}_{-0.12}$	$4.50^{+1.26}_{-0.97}$	$0.44^{+0.07}_{-0.13}$	0.47	$8.93^{+0.15}_{-0.14}$	$6.77^{+1.46}_{-1.11}$	$0.54^{+0.09}_{-0.16}$	0.59

Table 3.2 Solutions to $\log(M_{\rm BH}/M_\odot) = \alpha + \beta \log(\sigma_{\rm GC}/200\,{\rm km\ s^{-1}})$ for different GC subsets. Shown are the sample size N, the intercept α, the slope β, the intrinsic scatter ϵ and the total rms scatter Δ in the $\log M_{\rm BH}$ direction for both the forward (minimise $\log M_{\rm BH}$ residual) and for the inverse regression (minimise $\log \sigma$ residual).

The second quantity, $v_{\rm GC}$, does not assume a Gaussian velocity distribution and it represents the azimuthally averaged second-order velocity moment which includes rotation:

$$v_{\rm GC}^2 = \frac{1}{N}\sum_{i=1}^{N}(v_{\rm i} - v_{\rm sys})^2 - (\Delta v_{\rm i})^2. \tag{3.2}$$

where N is the sample size and $\Delta v_{\rm i}$ is the uncertainty on the radial velocity v_i of the $\rm i^{th}$ globular cluster. The uncertainty on $v_{\rm GC}$ is estimated through the formula from Danese et al. (1980). We will refer to $v_{\rm GC}$ of the *red*, *blue* and *all* GCs as $v_{\rm GC,R}$, $v_{\rm GC,B}$, $v_{\rm GC}$ respectively.

The difference between $\sigma_{\rm GC}$ and $v_{\rm GC}$ is that the former represents the rotation-subtracted velocity dispersion whereas the latter also includes the rotation of the spheroid and it is a better reflection of specific kinetic energy. A comparison between $\sigma_{\rm GC}$ and $v_{\rm GC}$ is given in Figure 3.1 for our galaxy sample without any GC subpopulation split. The two quantities are consistent with each other when the rotation component is negligible, as seen for several systems.

We perform a "sanity check" on all literature data. We prune GCs deviating more than 3σ from the local GC velocity distribution. We also clip outliers with unreasonably large uncertainty (usually > 100 km s^{-1}) and then we recalculate the respective $\sigma_{\rm GC}$ and $v_{\rm GC}$ to avoid methodology biases.

3.2.2 The $M_{\rm BH} - \sigma_{\rm GC}$ and $M_{\rm BH} - v_{\rm GC}$ relations for GC systems

Here we describe how we characterize the $M_{\rm BH} - \sigma_{\rm GC}$ relation. The procedure is identical for the $M_{\rm BH} - v_{\rm GC}$ relation.

In logarithmic space, $M_{\rm BH}$ and $\sigma_{\rm GC}$ appear to be linearly correlated. The relation we want to study is therefore:

$$\log\left(\frac{M_{\rm BH}}{M_\odot}\right) = \alpha + \beta\log\left(\frac{\sigma_{\rm GC}}{200\,{\rm km\ s^{-1}}}\right), \tag{3.3}$$

where α and β are the intercept and the slope of the relation. The numerical constant (200 km s^{-1}) is the normalization factor adopted in similar studies of the stellar $M_{\rm BH} - \sigma_*$ relation. We then use the χ^2–minimization technique (Press et al., 1992) as modified by Tremaine et al. (2002). This ensures that the best fit to Equation 3.3 is not biased in the case of large uncertainties (Park et al., 2012a). Our minimization function is, using the notation $y = \alpha + \beta x$:

$$\chi^2(\alpha,\beta) \equiv \sum_{i=1}^{N}\frac{(y_i - \alpha - \beta x_i)^2}{\epsilon_{y,i}^2 + \beta^2\epsilon_{x,i}^2 + \epsilon^2} \tag{3.4}$$

where ϵ_x and ϵ_y are the errors on x and y respectively. These are defined as $\epsilon_x = (\log\sigma_{\rm upper} - \log\sigma_{\rm lower})/2$ and $\epsilon_y = (\log M_{\rm BH,upper} - \log M_{\rm BH,lower})/2$, respectively. The term ϵ is the intrinsic

scatter in the y direction in units of dex. ϵ is iteratively adjusted so that the value of $\chi^2/(N-2)$ equals $1 \pm \sqrt{2/N}$. Uncertainties on α and β were obtained by bootstrapping the sample 2000 times and selecting the 68 per cent confidence interval.

This χ^2 estimator does not treat the data symmetrically in the presence of intrinsic scatter. An "inverse" regression (minimizing the $\log \sigma_{\rm GC}$ residuals rather than the $\log M_{\rm BH}$ residuals) can lead to very different slopes. The latter is preferable in the presence of possible Malmquist-type biases (see Graham et al., 2011). Given our ignorance of the physical mechanisms which links black hole mass to velocity dispersion, there is no reason to believe that the forward regression should be favored over the inverse regression. Therefore, we perform both the "forward" and the "inverse" regression by replacing ϵ in Equation 3.4 with $\beta^2\epsilon^2$ as suggested by Novak et al. (2006).

3.3 Results

The $M_{\rm BH} - v_{\rm GC}$ (and the $M_{\rm BH} - \sigma_{\rm GC}$) diagrams for our sample are shown in Figure 3.2, in which the final slope and intercept of the relations are the average between the forward and the inverse fit. The respective best fit parameters are reported in Table 3.2.

We find that $M_{\rm BH}$ correlates both with $\sigma_{\rm GC}$ and $v_{\rm GC}$ for all GC subsamples. However, we note that the intrinsic scatter of all our GC subsets are at least two times larger than those reported by SC12. We find that this disagreement is driven by the $M_{\rm BH}$ values of five galaxies in the SC12 sample (marked in Table 3.1 with "a") for which we have updated $M_{\rm BH}$ measurements. In fact, reanalyzing the SC12 sample using our new velocity dispersion values and the $M_{\rm BH}$ values from SC12 (all from Gültekin et al. 2009a and references therein), we always obtain $\epsilon \leq 0.31$ dex, which is in agreement with their findings. Conversely, the regression on the SC12 sample using updated $M_{\rm BH}$ values, returns $\epsilon = 0.38$ dex for the full sample and $\epsilon = 0.44$ dex for the blue and red GC subsets. We conclude that the small intrinsic scatter of SC12 is driven by their black hole mass values and not by their GC system velocity dispersion data. This assumes that the latest values of $M_{\rm BH}$ that we adopt here are also more accurate than those which preceded them.

The slope, intercept and intrinsic scatter of the $M_{\rm BH} - v_{\rm GC}$ and the $M_{\rm BH} - \sigma_{\rm GC}$ relations are consistent with each other within the errors. Similarly, the differences found for the blue and red GCs are not statistically significant. We note that the slopes of the $M_{\rm BH} - v_{\rm GC}$ relations are always steeper than the $M_{\rm BH} - \sigma_{\rm GC}$ ones, because $v_{\rm GC} > \sigma_{\rm GC}$ at low masses. Also, the smaller intrinsic scatter with $v_{\rm GC}$ suggests that the GC kinetic energy (rotation plus dispersion) is a better predictor of black hole masses than the rotation-subtracted velocity dispersion.

The intrinsic scatter of the $M_{\rm BH} - v_{\rm GC}$ and $M_{\rm BH} - \sigma_{\rm GC}$ relations are slightly larger than that of the stellar $M_{\rm BH} - \sigma_*$ relation from McConnell & Ma (2012) and Graham & Scott (2012), who both find $\epsilon \sim 0.4$ dex. The best-fit to the stellar $M_{\rm BH} - \sigma_*$ relation computed using our

21 galaxies has an intrinsic scatter of $\epsilon = 0.35^{+0.08}_{-0.05}$ dex in the $\log M_{\rm BH}$ direction, which is also consistent with previous findings.

Lastly, it is noted that the stellar $M_{\rm BH} - \sigma_*$ relation in Figure 3.2 is shifted towards larger velocity dispersion values with respect to the $M_{\rm BH}-$ (GC system velocity dispersion) relations. This offset is expected because σ_* and the GC system velocity dispersion sample different regions, and maybe different physics, of the galaxy velocity dispersion profile. The stellar velocity dispersion, which probes $(R < R_e)$, is usually larger than the GC system velocity dispersion, which usually probes $R > R_e$. The difference $(\sigma_* - v_{\rm rms,A})$ is found to have a mean of 35 ± 6 km s^{-1} for our 21 galaxies.

3.3.1 Radial trends

It is interesting to see if the properties of the $M_{\rm BH} - v_{\rm GC}$ or $M_{\rm BH} - \sigma_{\rm GC}$ relation vary when the velocity dispersion is computed within different galactocentric radii.

To do so, we first normalize the galactocentric radii of each GC system to the host galaxy effective radius. We then perform χ^2 tests (Equation 3.4) with $v_{\rm GC}$ and $\sigma_{\rm GC}$ computed within different radial bins. For the sake of consistency, we adopt effective radii values from 2MASS, and we use the transformations from Cappellari et al. (2011) to make them consistent with the values of the RC3 catalogue (de Vaucouleurs, 1991).

The cumulative velocity dispersion profiles for our galaxy sample are shown in Figure 3.3 for all GC subsets. The profiles are generally flat over the radial range probed. It is worth noting that GC dispersion profiles span different radial ranges depending on the galaxy, and we do not extrapolate the dispersion profiles to compensate for this effect. Therefore, the number of GC systems within a given effective radius varies with the radius itself. Demanding a minimum of six GC systems per radial bin, we study the $M_{\rm BH} - v_{\rm GC}$ and the $M_{\rm BH} - \sigma_{\rm GC}$ relations between 3.5 and 5.5 R_e for the blue and the red GC subpopulations.

Results are shown in Figure 3.4 for the $M_{\rm BH} - v_{\rm GC}$ relation. Each radial bin contains between six to a maximum of eleven GC systems. As expected from the flatness of the velocity dispersion profiles (Figure 3.3), none of the radial trends seen in Figure 3.4 are statistically significant. The relations for the blue and the red GC subpopulations are also statistically indistinguishable. There is an hint that the intrinsic scatter for the $M_{\rm BH} - v_{\rm GC,R}$ becomes smaller towards the central regions. This result is biased by the fact that the red GCs tend to be more centrally concentrated than the blue GGs. Given the small number statistics, the best fit to the $M_{\rm BH} - v_{\rm GC}$ relation is independent of radius within which the velocity dispersion is measured, at least for $R > R_e$. The same exercise performed on the rotation-subtracted velocity dispersion $\sigma_{\rm GC}$ leads to a similar result.

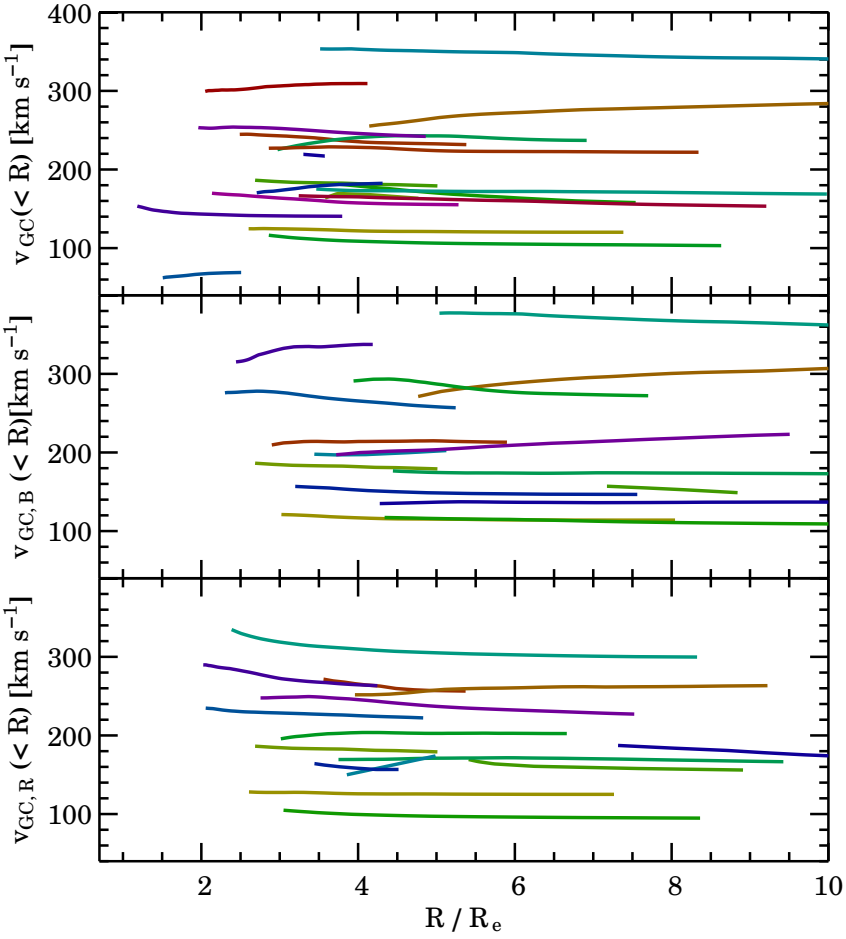

Figure 3.3 Cumulative root-mean-square velocity dispersion profiles. The plot shows the rotation-included velocity dispersion profiles within a certain radius for all (top panel), blue (central panel) and red GCs (bottom panel). A running mean is used. Different colors represent different galaxies. Most of the profiles are generally flat at all radii.

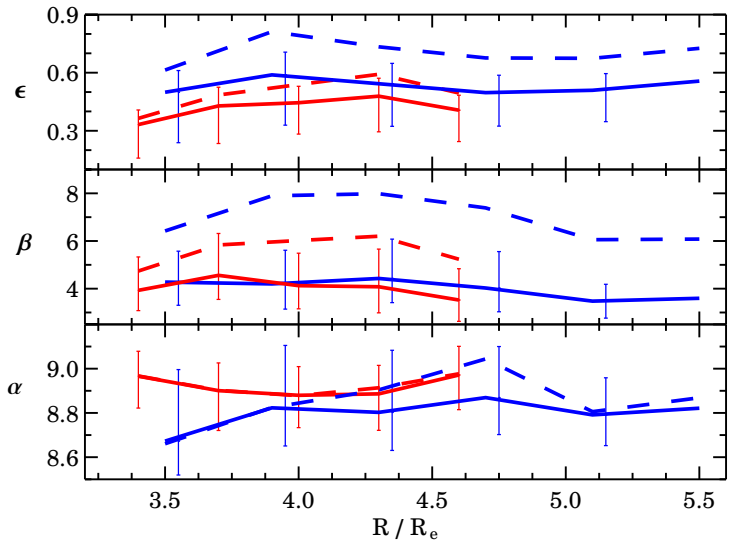

Figure 3.4 Best-fit $M_{\rm BH} - v_{\rm GC}$ relation within different radial bins. The plot shows how the best-fit α, β and ϵ vary when the $v_{\rm GC}$ is computed within an increasing number of effective radii. Blue and red colours represent the two GC subpopulations. Solid and dashed lines are the results from the forward and the inverse regressions respectively. The horizontal axis is the radius of the outermost GC in a given radial bin. For clarity, only the error bars from the forward regression are shown. None of the radial trends are statistically significant.

A caveat to bear in mind is the way the GC system velocity dispersion is computed. Ideally, one should weight the velocity dispersion for the GC surface density within a certain radius, similarly to what is done for the stellar velocity dispersion σ_* (see Equation 1 in McConnell & Ma 2012). Similarly, the scale radius used in Figure 3.3 should be the GC system's effective radius and not the host galaxy's effective radius. However, GC surface density profiles are not available for all our galaxies. They are also dependent on variables such as GC selection criteria and imaging field-of-view, which have been carried out differently in the literature.

On the other hand, total GC system size scales with galaxy effective radius (Kartha et al., 2013) and we see no strong variation of GC system velocity dispersion with radius.

3.3.2 Cores and bars

The stellar $M_{\rm BH} - \sigma_*$ relation is different for galaxies with or without bars (Graham et al., 2011). It is thought that the orbital structure of the bar may elevate the apparent bulge velocity dispersion (Bureau & Athanassoula, 1999), resulting in an offset $M_{\rm BH} - \sigma_*$ relation for barred galaxies with the appropriate bar orientation. On the other hand, the $M_{\rm BH} - \sigma_*$ relation does not differ for non-barred galaxies with or without a 'core' in the inner surface brightness profile (Graham & Scott, 2012). An exception may however exist for ultramassive black holes such as those in NGC 3842

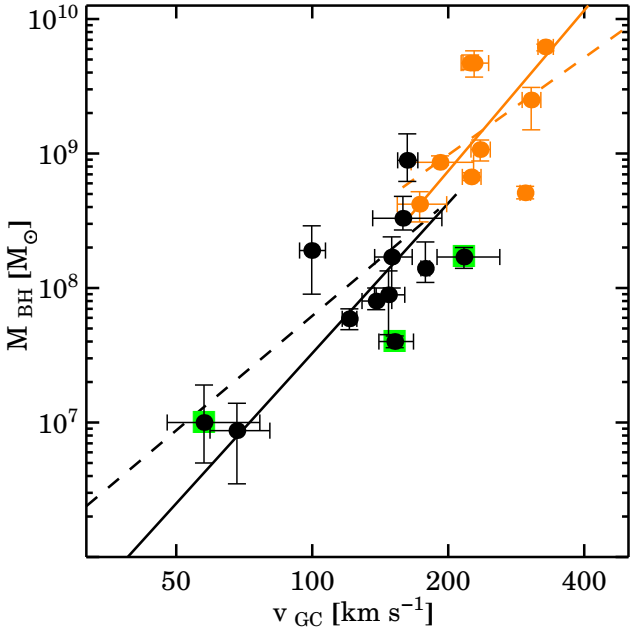

Figure 3.5 $M_{\rm BH} - v_{\rm GC}$ relation. Orange and black points are galaxies with and without a core in the inner surface brightness profile respectively. The filled and dashed lines are the best fits to core and non-core galaxies when using $v_{\rm GC}$ and $\sigma_{\rm GC}$ respectively. Green boxes mark barred galaxies (NGC 1316, NGC 1023 and NGC 253). The slope of the $M_{\rm BH} - v_{\rm GC}$ relation for core galaxies is consistent within the errors with that of non-core galaxies.

and NGC 4489 (McConnell et al., 2011). If these are included in the fit, the $M_{\rm BH} - \sigma_*$ relation for core galaxies is steeper ($\beta \sim 7.0$) than that for non-core galaxies.

We have tested if the trends seen for 'core' and barred galaxies with stellar data are also present in our $M_{\rm BH} - v_{\rm GC}$ and $M_{\rm BH} - \sigma_{\rm GC}$ relations. To avoid low number statistics issues, we only look at the whole GC population, without any colour split.

Our sample contains only three barred galaxies (NGC 1023, NGC 1316 and NGC 253), preventing any statistical analysis. For the sake of completeness, we note that NGC 1023 and NGC 1316 are indeed offset to higher velocity dispersions relative to the best-fit $M_{\rm BH} - v_{\rm GC}$ relation (Figure 3.5). However, only NGC 1023 is offset when considering $\sigma_{\rm GC}$. NGC 253 is neither offset from the $M_{\rm BH} - v_{\rm GC}$ nor the $M_{\rm BH} - \sigma_{\rm GC}$ relation, in agreement with what was found for stellar data.

Regarding 'core' galaxies, our sample contains nine core galaxies and twelve non-core galaxies (see Table 3.1). The centre of the galaxy NGC 1407 is actually unclassified, but assume this galaxy to have a central core given its mass. We treat NGC 1316 (Fornax A) as a cored galaxy (Faber et al., 1997), but the reader should see the cautionary remarks in Graham & Scott (2012) regarding this galaxy's lack of a bulge/disc decomposition.

The relation between $M_{\rm BH}$ and GC system velocity dispersion for core/non-core galaxies is shown in Figure 3.5. We remind the reader that the final slope of the $M_{\rm BH}-$ (GC system velocity dispersion) relations is the average between the forward and the inverse regression. Using the uncertainty on the slope and intercept of each regression, we derived a weighted mean to account for the large uncertainties caused by low number statistics. For non-core galaxies, we obtain a slope of $\beta = 3.6 \pm 1.5$ and $\beta = 2.8 \pm 1.5$ for the $M_{\rm BH} - \sigma_{\rm GC}$ and $M_{\rm BH} - v_{\rm GC}$ relations respectively. For core galaxies, the uncertainty on the slope from the inverse regression is larger than the slope itself. This means that the final slope of this relation is driven only by that of the forward regression. In this case, we find $\beta = 2.2 \pm 1.6$ and $\beta = 2.4 \pm 1.6$ for the $M_{\rm BH} - \sigma_{\rm GC}$ and $M_{\rm BH} - v_{\rm GC}$ relations respectively. In conclusion, the $M_{\rm BH}-$ (GC system velocity dispersion) relations for core and non-core galaxies are consistent with each other as found by Graham & Scott (2012) with stellar velocity dispersion data.

3.3.3 Predicting $M_{\rm BH}$ in other galaxies

We exploit the best fit $M_{\rm BH}-$ (GC system velocity dispersion) relations found in this work to predict $M_{\rm BH}$ in galaxies without direct black hole mass measurements. We collected a sample of 13 galaxies with GC system kinematic information, listed in Table 3.3. The first four galaxies were re-analyzed in Pota et al. (2013) with the methods described in §3.2.1. Similarly, we re-analyzed the GC system kinematics of NGC 4406 (Park et al., 2012b) and of three luminous Virgo dwarf ellipticals (dEs) from Beasley et al. (2009) and Beasley et al. (2006). Given that the $M_{\rm BH}-$ (GC system velocity dispersion) relations for the blue and the red GC subpopulations return consistent results, we decided to use the best fit $M_{\rm BH} - v_{\rm GC}$ relation:

$$\log\left(\frac{M_{\rm BH}}{M_\odot}\right) = 8.79 + 4.45\log\left(\frac{v_{\rm GC}}{200\,{\rm km\ s^{-1}}}\right) \tag{3.5}$$

where the slope and the intercept of this relation are the average between the forward and the inverse regression from Table 3.2.

Predicted black hole masses are given in Table 3.3. Particular emphasis should be given to the three Virgo dEs, whose predicted $M_{\rm BH}$ falls into the range of intermediate mass black holes ($\lesssim 10^6 M_\odot$). All three dEs are known to have a nuclear star cluster (Ferrarese et al., 2006), whose masses are about one order of magnitude larger than our predicted black hole masses, as is expected (Scott & Graham, 2013). In fact, the relation between the mass of the nuclear star cluster $M_{\rm NC}$ and stellar velocity dispersion σ_* does not run parallel to the stellar $M_{\rm BH} - \sigma_*$. At fixed $\sigma_* \lesssim 150$ km s^{-1}, Graham & Scott (2012) shows that $M_{\rm NC} > M_{\rm BH}$, which is in agreement with our findings.

Galaxy	Type	$v_{\rm GC}$ [km s^{-1}]	$M_{\rm BH}$ [$M_\odot$]	Ref.
NGC 1380	S0	160^{+23}_{-17}	$2.2^{+1.8}_{-0.9} \times 10^8$	1
NGC 3311	cD	653^{+48}_{-40}	$1.2^{+0.4}_{-0.3} \times 10^{11}$	2
NGC 3923	E4	273^{+42}_{-29}	$2.4^{+2.1}_{-0.9} \times 10^9$	3
NGC 4636	E2	212^{+11}_{-10}	$7.9^{+2.0}_{-1.5} \times 10^8$	4
NGC 4406	E3	295^{+54}_{-36}	$3.4^{+3.8}_{-1.5} \times 10^9$	5
VCC 1261	dE	56^{+18}_{-11}	$2.1^{+5.1}_{-1.3} \times 10^6$	6
VCC 1528	dE	52^{+22}_{-15}	$1.5^{+5.7}_{-1.1} \times 10^6$	7
VCC 1087	dE	41^{+14}_{-10}	$5.2^{+14}_{-3.7} \times 10^5$	8
NGC 1400	S0	137^{+14}_{-11}	$1.1^{+0.6}_{-0.3} \times 10^8$	9
NGC 2768	E6	165^{+13}_{-11}	$2.6^{+1.0}_{-0.6} \times 10^8$	10
NGC 4278	E2	177^{+9}_{-7}	$3.5^{+0.8}_{-0.6} \times 10^8$	11
NGC 4365	E3	248^{+12}_{-10}	$1.6^{+0.3}_{-0.2} \times 10^9$	12
NGC 4494	E1	99^{+14}_{-12}	$2.6^{+2.1}_{-1.1} \times 10^7$	13

Table 3.3 Black hole mass predictions. Listed from the left to right are: galaxy name, morphological type, GC root-mean-square velocity dispersion, predicted black hole mass from Equation 3.5 and the GC references. Galaxies below the horizontal line are from the SLUGGS survey. References to GC data are: 1, Puzia et al. (2004); 2, Misgeld et al. (2011); 3, Norris et al. (2012); 4, Lee et al. (2010a); 5, Park et al. (2012b); 6, 7, Beasley et al. (2009); 8, Beasley et al. (2006); 9,10,11,12, Pota et al. (2013); 13, Foster et al. (2011).

It is also worth noting that NGC 3311, the dominant elliptical galaxy of the Hydra Cluster, is at first glance predicted to host an ultramassive black hole candidate with $M_{\rm BH} \sim 10^{11} M_\odot$. However, caveats here are the inclusion of ultra compact dwarfs (UCDs) which make up half of the kinematic sample of this galaxy. UCDs can be kinematically distinct from the underlying GC system (e.g. Strader et al., 2011) and they can bias the velocity dispersion calculation. Another source of contamination might come from intra-cluster UCDs/GCs (Misgeld et al., 2011; Richtler et al., 2011). Excluding the 52 UCDs and looking only at the GC sample, which may still be biased by the cluster potential, we obtain $M_{\rm BH} = 8.4^{+4.7}_{-2.6} \times 10^{10}$. This is still more massive than the most massive SMBH known today (McConnell et al., 2011).

3.4 Discussion and conclusions

The aim of this paper was to test how well the velocity dispersion of extragalactic globular cluster systems correlates with the mass of supermassive black holes. This was motivated by the work of Sadoun & Colin (2012) who found an intriguingly tight correlation using 12 globular cluster systems.

In this work we have extended this study to a sample of 21 GC systems and we have used

the latest compilation of SMBH masses. We confirm that the velocity dispersion of GC systems correlates with SMBH mass. However, this correlation is less significant than that inferred by Sadoun & Colin (2012). The tight correlation found by these authors was driven by old, and possibly less accurate, black hole mass values. We observe an rms scatter in excess of 0.4 dex in the $\log M_{\rm BH}$ direction.

We looked at the correlation between $M_{\rm BH}$ and the velocity dispersion of the blue and the red GC subpopulations separately. Different scatters are expected if blue and red GC systems trace the kinematics of the halo and the bulge of the host galaxy respectively. In the case of a stronger correlation with red GCs, this would suggest that SMBHs grew along with the stellar bulge. Conversely, a stronger correlation with blue GCs would suggest that SMBHs formation is more closely related with the halo. Our current results cannot discriminate between these two scenarios. In general, we find no significant difference between the $M_{\rm BH}-$ (GC system velocity dispersion) relation for the blue and the red GCs. This can be due to some factors discussed below.

Ideally, one should analyze the bluer and the redder GCs for each GC system to avoid contamination in proximity to the blue/red dividing colour. This can make a difference in the final value of the GC system velocity dispersion (Pota et al., 2013). At the same time, this would decrease the number statistics for most of the galaxies. Also, uneven GC spatial sampling can affect the final kinematic outcome, as seen for NGC 4636 in Schuberth et al. (2012).

We have looked at the $M_{\rm BH}-$ (GC system velocity dispersion) relation computing the GC system velocity dispersion within different galactocentric radii, obtaining no significant trends with radius. Collectively, this suggests either that the $M_{\rm BH}-$ (GC system velocity dispersion) relation is secondary, or that a larger galaxy sample will be needed to discriminate which of the GC subpopulation trends is the stronger.

We have looked for possible trends in the $M_{\rm BH}-$ (GC system velocity dispersion) relation for core/non-core galaxies, finding similar slopes, in agreement with stellar velocity dispersion results (Graham & Scott, 2012).

The best fit relation between $M_{\rm BH}$ and the rotation-included GC system velocity dispersion has been used to predict black hole masses in 13 galaxies. This implies that NGC 3311 contains an ultramassive black hole with $M_{\rm BH} \sim 10^{11} M_{\odot}$.

4

Cusp or core? The shape of the dark matter halo of the galaxy NGC 1407 from stars and globular clusters

4.1 Introduction

In this Chapter we attempt the first measurement of the shape of the DM halo of an elliptical galaxy using the pinch point technique. The colour/metallicity distribution of globular (GCs) systems in galaxies is bimodal (Brodie & Strader, 2006). We will combine the mass modelling of the two GC supopulations in the outer regions, with that of the stellar component in the galaxy central region. With three independent gravitational tracers (i.e. stars, blue GCs and red GCs) we can derive the mass within three pinch radii with an accuracy of $\sim 20\%$. We carefully analyze how the uncertainty on the stellar mass, and therefore on the initial mass function (IMF), influences our results.

Our test galaxy is NGC 1407, a massive E0 at the centre of the Eridanius group (Brough et al., 2006). This choice is motivated by the copious GC dataset we discussed in Chapter 2 and by the recent wide-field stellar kinematic measurements up to three effective radii from Arnold et al. (2013). The mass content of NGC 1407 has been modeled with half of our current GC dataset (Romanowsky et al., 2009; Spitler et al., 2012) and using X-ray data (Humphrey et al., 2006; Zhang et al., 2007).

We will start by describing the stellar and globular cluster data in Section 4.2. In Section 4.3 we will discuss the method, assumptions and caveats of the mass modelling. The results from the dynamical modelling will be analyzed in Section 4.4 and then combined together to construct the dark matter mass profile of NGC 1407 in Section 4.5. We discuss and summarize our results in Section 4.6 and Section 4.7 respectively.

4.2 Data

In this section we discuss the photometric and kinematic dataset for the stars and the GCs of NGC 1407. They are both data-products of the SLUGGS survey and they have been partially discussed in a series of papers (Proctor et al., 2009; Usher et al., 2012; Pota et al., 2013) and in Chapter 2.

4.2.1 Distance and conventions

The distance of NGC 1407 is very uncertain. Using the GC luminosity function, Forbes et al. (2006) found $D = 20.9$ Mpc, which is the value adopted by Romanowsky et al. (2009). From surface brightness fluctuations (Tonry et al., 2001; Cantiello et al., 2005) one obtains larger distances, 25 Mpc $\leq D \leq$ 29 Mpc, depending on whether or not the Cepheid zero-point correction is applied (Mei et al., 2007; Jensen et al., 2003). The latter is the range of distances adopted in other studies of NGC 1407 (Humphrey et al., 2006; Zhang et al., 2007; Giacintucci et al., 2012; Rusli et al., 2013b). In this paper we will assume $D = 28.05$Mpc as in Rusli et al. (2013b) because it makes it more handy to compare our results with those from the literature, and because we will adopt their stellar surface brightness profile for the reasons explained in this section. With this distance assumption, 1 arcsec corresponds to 0.136 kpc.

Throughout the paper we will refer to the galactocentric 2D (projected) radius and 3D (deprojected) radius as R and r, respectively. The galactocentric radius is defined as the circularized radius $R^2 = (q\,X^2) + (Y^2/q)$, where (X, Y) are the cartesian coordinates of an object with the centre of NGC 1407 at the origin. $q = 0.95$ is the minor-to-major axis ratio and it does not show any significant variation with radius (Spolaor et al., 2008a).

We will show that the three potential tracers are generally pressure-supported, meaning that the rotation is negligible at all radii, with the red GCs being an uncertain exception. For our analysis we will compute the root-mean-square velocity dispersion $v_{\rm rms}^2 \approx v_{\rm rot}^2 + \sigma^2$, that includes the contribution of the rotation velocity $v_{\rm rot}$ and of the true velocity dispersion σ. However, we will often refer to $v_{\rm rms}$ as "velocity dispersion".

All quoted uncertainties are $\pm$ 1 sigma, i.e. 68 per cent confidence interval.

4.2.2 Stellar surface brightness

The galaxy luminosity profile is an essential quantity to measure the underlying dark matter mass in the galaxy central regions, where baryons dominate over the dark matter.

Here we use the surface brightness profile in $B-$band presented in Rusli et al. (2013a). We use the best-fit parameters from their Table 2 and 3. The fit to the data is achieved by fitting three

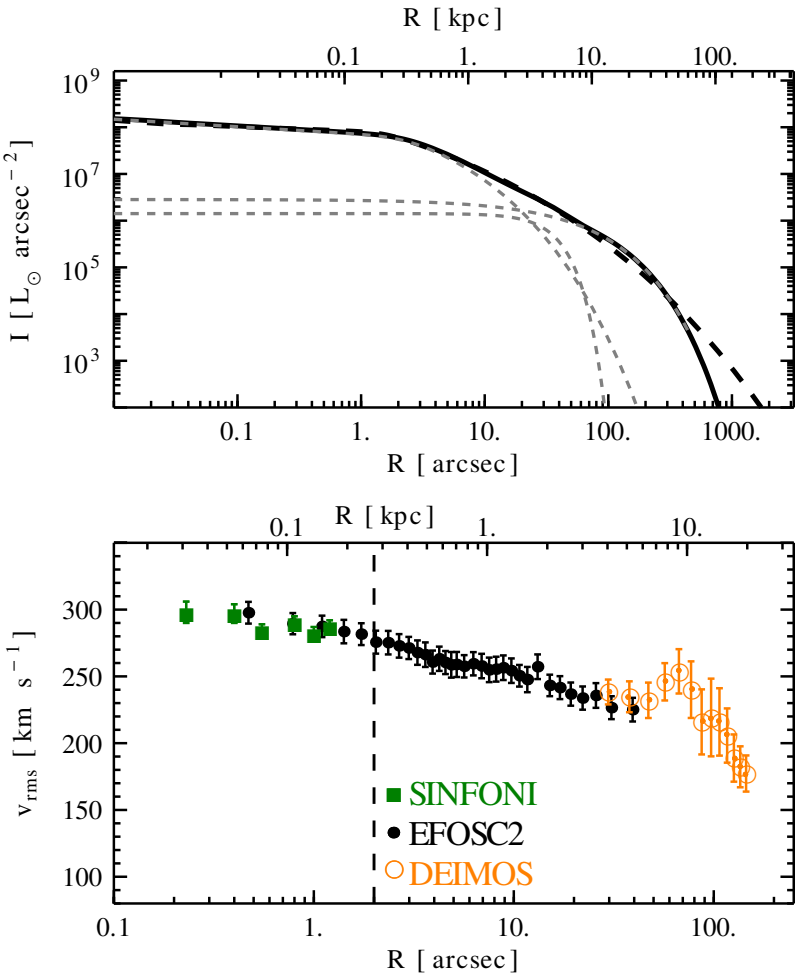

Figure 4.1 Stellar data.*Top panel:* fits to the stellar surface brightness profile using the photometric parameters from Rusli et al. (2013b). Gray dashed lines represent the core-Sèrsic and the two Sèrisc laws needed to fit the data (not shown here). The thick black line is the total surface brightness profile in the B-band. The transition from core to Sèrisc regime occurs at $R \approx 2$ arcsec. *Bottom panel:* stellar velocity dispersion profile. Different colours correspond to data from different spectrographs as labelled on the bottom. The horizontal dashed line at $R = 2$ arcsec shows the transition radius from core to Sèrisc regime.

components: one core-Sèrsic and two Sèrsic profiles. We re-present the PSF deconvolved best fit to the surface brightness profile of NGC 1407 in Figure 4.1. This surface brightness profile corresponds a total luminosity of $7 \times 10^{10} L_{\odot}$ and to a total absolute magnitude $M_B = -21.6$ mag, where we have adopted a solar absolute magnitude of $M_{\odot,B} = 5.48$ mag. We compute the 2D effective radius R_e empirically, by determining the radius which encompasses half of the total luminosity of the galaxy. We find $R_e = 80$ arcsec $= 10.8$ kpc and we will use this value throughout the paper. This value is ~ 10 arcsec larger than the one found in Spolaor et al. (2008b), but their data only extended up to 100 arcsec.

4.2.3 Stellar kinematics

We use ESO3.6/EFOSC2 major axis long slit data from Proctor et al. (2009) between 0 and 40 arcsec. The $v_{\rm rms}$ profile was obtained by folding and averaging the data with respect to the centre of the galaxy[1]. Long slit data were supplemented with Keck/DEIMOS data from Arnold et al. (2013) between 30 and 180 arcsec. This is an improved version of the data published in Proctor et al. (2009). The DEIMOS dataset was processed with a kinemetry approach as described in Foster et al. (2013). For the innermost few arcsecs we also use VLT/SINFONI data from Rusli et al. (2013b). They give stellar velocity dispersion profiles from the major to the minor axis in five azimuthal slices, that we average in order to obtain the azimuthally averaged velocity dispersion profile.

The combined stellar velocity dispersion profile of NGC 1407 is shown in Figure 4.1. The stellar dispersion profile declines smoothly with radius to $R \sim 50$ arcsec. Outside this radius we notice a velocity dispersion "bump" between 50 and 100 arcsec where the velocity dispersion is considerably larger than the surrounding values. Interpreting the meaning of such a substructure goes beyond the aim of this paper. We can confidently state that this feature is not an artifact of the data processing (e.g., wrong wavelength calibration) because the Keck/DEIMOS data are fully consistent with the long slit data in the region of overlap. This kinematic substructure can also be seen in metallicity space, with the stars between 50 and 100 arcsec being more metal-rich (up to 0.5 dex in [Z/H]) than the local metallicity distribution (Pastorello et al., in prep.). These substructures are akin to those found in the Milky Way halo (Kafle et al., 2012) and interpreted as perturbations from ongoing accretion of satellite galaxies (Sharma et al., 2011). In the specific case of NGC 1407 the merger scenario is supported by the presence of a kinematic decoupled core at the centre of the galaxy (Spolaor et al., 2008b). Very recently, Phoebe Schauer et al. (2013) shows that the bump in NGC 1407 can be the signature of a major merger. We will further discuss

[1]Following Napolitano et al. (2009),we estimate the $v_{\rm rms}$ of long slit data as $v^2_{\rm rms} \approx v^2_{\rm rot}/2 + \sigma^2$ because we only have data along the major axis. Note, however, that this has small impact on the final result, given that $v_{\rm rot} \ll \sigma$ at all radii.

these kinematic substructures in §4.3.1.

4.2.4 Globular cluster surface density

We use wide-field imaging from Subaru/Suprime-Cam in gri filters taken in excellent seeing conditions ($\sim$ 0.5 arcsec). Details on data acquisition and reduction are given in Chapter 2 (see §2.3.1). GCs candidates were selected in colour-colour and colour-magnitude space. The resulting GC colour distribution is clearly bimodal, with a dividing colour between blue and red GCs occurring at $(g-i) \approx 0.98$ mag.

The GC surface density was obtained by binning candidates brighter than $i < 25.5$ mag in circular annuli centered on the galaxy, and dividing the resulting number by the area of the annuli. We adopt a fixed number of GCs per bin, usually larger than 50 GCs per bin, depending on the colour cut. Poissonian errors on the surface density were calculated as the ratio $\sqrt{\text{GCs per bin}}/\text{Area of the annulus}$.

The resulting GC surface density profiles was fit with a modified Sérsic function of the form:

$$N_{\rm GC}(R) = N_e \times \exp\left(-b_n\left[\left(\frac{R}{R_e}\right)^{1/n} - 1\right]\right) + bg, \tag{4.1}$$

where $b_n = 1.9992n - 0.3271$, n is the Sersic index, R_e is the projected half-number radius of the GC system, N_e is the surface density at that radius and bg is the background contamination level, which was assumed to be homogeneous across the image. The surface density profile is shown in Figure 4.3 both for the blue and for the red GCs. The red are more centrally concentrated than the blue GCs as found in almost all GC systems studied so far (Kartha et al., 2013, and references therein).

The effect of the colour cut

Although the blue and red GCs are well separated in $(g-i)$ colours, a certain level of contamination between the two is expected at $(g-i) \sim 0.98$, especially for fainter objects. Before performing any mass modelling, we need to quantify this contamination.

We consider the catalogue of photometrically selected GCs with $20 < i < 25.5$ to minimize incompleteness at faint magnitudes and to minimize contamination from Galactic stars at bright magnitudes. This selection returns $\sim 10\,400$ objects. Next, we divide this sample into seven blue subsamples with $(g-i) < 0.98 - k$ and seven red subsamples with $(g-i) > 0.98 + k$, where the index k runs from 0 to 0.13 with step of 0.02. We then fit Equation 4.1 to the fourteen subsamples and we study how the photometric parameters vary with the adopted colour cut.

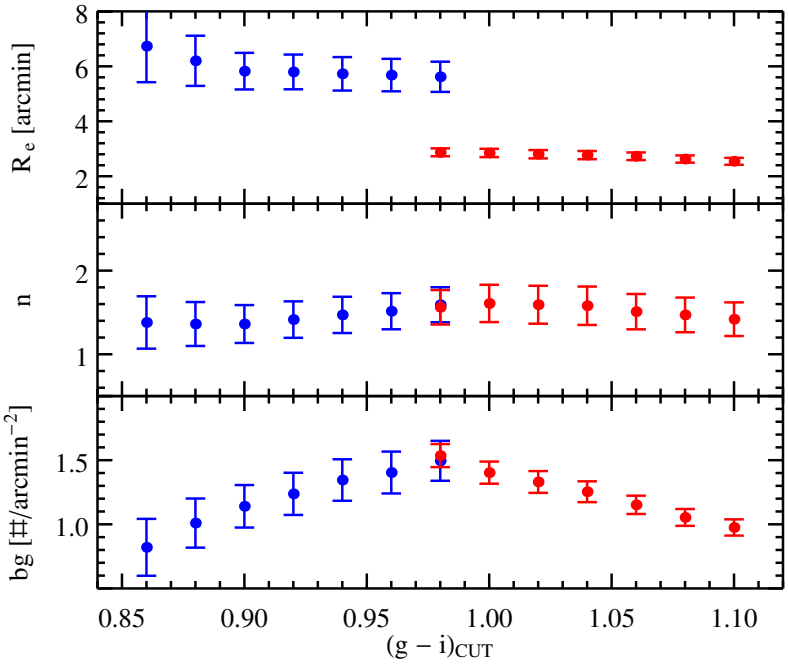

Figure 4.2 Photometric GC system properties as a function of colour. From the top to the bottom we show the projected effective radius R_e, the Sérsic index n and the background level bg computed for different colour cuts at $(g-i)_{\rm CUT}$.

GC Sample	N_e	R_e [arcsec]	n	bg [GCs arcmin^{-2}]
Blue	7.1±1.2	346±35	1.6±0.2	1.4±0.2
Red	20.1±2.2	170±9	1.6±0.2	1.4±0.1

Table 4.1 GC photometric parameters. The table shows the best-fit parameters to Equation 4.1 for a colour cut at $(g-i)_{\rm CUT} = 0.98$ for the blue and the red GCs respectively.

Results are shown in Figure 4.2, where the x-axis is the adopted colour cut. That is, datapoints with $(g-i)_{\rm CUT} \leq 0.98$ represent photometric quantities of blue GCs with $(g-i) < 0.98, 0.96, 0.94...$, whereas datapoints with $(g-i)_{\rm CUT} \geq 0.98$ represent photometric quantities of red GCs with $(g-i) > 0.98, 1.00, 1.02....$ This figure was drawn using 60 GCs per radial bin. We tried different bin sizes and found that results for 30 to 80 GCs per bin give still a stable fit to the data. The scatter from this specific bin size range is included in the uncertainties in Figure 4.2. Larger or smaller bin sizes will tend to oversample and undersample the surface density profile respectively. It can be seen that the best fit parameters to Equation 4.1 are remarkably constant regardless the colour cut. The Sèrsic index is stable around $n \approx 1.5 \pm 0.2$, whereas the effective radius of the two subpopulations is remarkably different as found in almost all GC systems studied so far.

Given the above results, we decided to perform our mass modelling with our fiducial colour cut set at $(g - i)_{\rm CUT} = 0.98$. This cut was applied both to the spectroscopic and to the photometric sample. The photometric quantities for this particular colour cut are given in Table 4.1.

4.2.5 Globular cluster kinematics

We derived GC radial velocities from Keck/DEIMOS spectra, for a total of 356 spectroscopically confirmed GCs. This represents a contaminants-free sample because both background galaxies and Galactic stars are ruled out during the analysis process. The former can be spotted because they show emission lines in their spectra, whereas the latter have radial velocities too low (generally between -200 and $+200$ km s^{-1}) to contaminate the NGC 1407 GC velocity distribution, which has a systemic velocity of 1779 km s^{-1}(from NED).

Moreover, we apply the following cuts:

- we clip confirmed GCs with radial velocities deviating more than 3σ from the local velocity distribution using the friendless algorithm of Merrett et al. (2003).
- We clip objects brighter than the Milky Way GC Ω Centauri ($M_i = -11.6$ mag), because it has been shown that kinematics of brighter and bigger GCs/UCDs is different from that of ordinary GCs (Strader et al., 2011).
- We remove red GCs further than 700 arcsec and blue GCs further than 800 arcsec in galactic radius because the phase-space is poorly sampled.

These selection criteria return 321 confirmed GCs, equivalent to 163 red and 158 blue GCs with a colour cut at $(g - i) = 0.98$. This is the final GC sample that we will use for the mass modelling in the next Section.

We calculate the root mean square velocity dispersion of the GC system as:

$$v_{\rm rms}^2 = \frac{1}{N}\sum (v_i - v_{\rm sys})^2 - (\delta v_i)^2 \tag{4.2}$$

where v_i and δv_i is the observed radial velocity and the associate uncertainty of the ith GC, respectively. $v_{\rm sys} = 1779$ km s^{-1} is the systemic velocity of NGC 1407, which is fully consistent with the median systemic velocity of the GC system (1778 km s^{-1}). The $v_{\rm rms}$ profile of the two GC subpopulations is shown in Figure 4.3.

We measure the amount of GC rotation by running a kinemetry code similar to the one discussed for the stellar component in §4.2.3. We measure the rotation amplitude $v_{\rm rot}$ and the rotation-subtracted velocity dispersion σ for the blue and the red GCs, and we show the ratio $(v_{\rm rot}/\sigma)$ in the bottom panel of Figure 4.3.

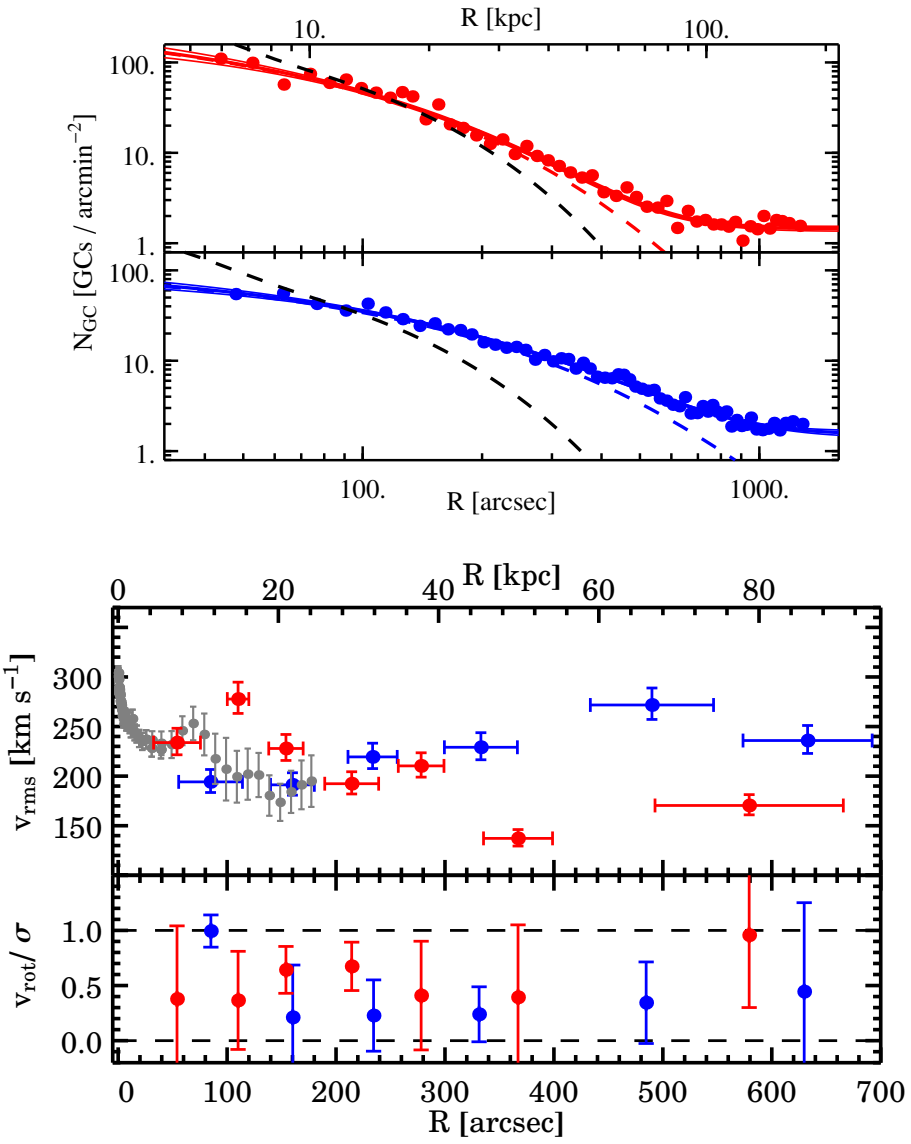

Figure 4.3 Globular cluster data. Plots are colour-coded according to the GC subpopulation. A colour cut at $(g-i) = 0.98$ was adopted to divide the blue and red GCs. *Top panel:* surface density profile of the blue and red GCs respectively. Coloured filled dashed lines represent the background-included and background-subtracted best Sèrsic fit to the data respectively. The black dashed line is the stellar surface brightness arbitrarily rescaled. *Bottom panel:* binned velocity dispersion profile for the blue GCs and the red GCs together with long slit data (gray points) for comparison. The velocity dispersion of the red GCs is structured with two velocity dispersion bumps at 150 arcsec and 250 arcsec. The bottom panel show the GC rotation amplitude $v_{\rm rot}$ over the GC rotation-subtracted velocity dispersion σ. Horizontal lines show $(v_{\rm rot}/\sigma) = 0, 1$ to guide the eye. Both the blue and the red GCs show some hint of rotation.

As we already showed in Chapter 2, the blue and the red GCs, divided at $(g-i)=0.98$, have very different kinematics. Figure 4.3 shows that the velocity dispersion of blue GCs increases with radius, whereas that of the red GCs decreases with radius, similar to the trend measured for the stars. We notice that the velocity dispersion of the red GCs presents two bumps in the range $50 < R < 120$ and $200 < R < 300$ arcsec respectively, at which the velocity dispersion increases with respect to the local value. These features are very similar to those discussed in §4.2.3 for the stellar kinematics. However, the "bump" measured for the red GCs and for the stars does not occur at the same galactocentric radius. The existence of these features is further evidence that the stellar substructures are probably real and possibly linked with those of the red GCs. We have tested that the GC substructures are not an artifact of the binning of the data or of the adopted colour cut.

As far as the GC rotation is concerned, the bottom panel of Figure 4.3 shows that the rotation of both GC subpopulations is very irregular with galactocentric radius. Blue GCs show significant rotation in the innermost radial bin only, whereas the red GCs rotate at intermediate and large radii. Red GC rotation is detected in proximity of to the two velocity dispersion bumps. This suggests that the rotation signal may be the effect of the kinematic substructures rather than streaming motions.

4.3 Jeans analysis

For each potential tracer (i.e., stars, red GCs and blue GCs) we solve the spherical Jeans equation (Jeans, 1915):

$$\frac{\mathrm{d}}{\mathrm{d}r}(\rho\sigma_r^2)+\frac{2\beta}{r}\rho\sigma_r^2=-\rho\frac{GM_{\rm tot}}{r^2} \tag{4.3}$$

where σ_r is the 3-dimensional velocity dispersion, β is the unknown orbital anisotropy parameter and ρ is the 3D density profile of the tracer. The equation above is solved with respect to the term $(\rho\sigma_r^2)$ and its solution is projected onto the sky in order to obtain the line-of-sight velocity dispersion to be compared with observations.

We assume that the total mass of system is given by $M_{\rm tot}(r)=M_*(r)+M_{\rm d}(r)$ where M_* and $M_{\rm d}$ are the mass of the the stellar component and of dark matter component respectively.

For the luminous mass, we de-project the stellar surface brightness by solving the Abel integral numerically, and we integrate the resulting stellar density profile ρ_* in order to obtain the cumulative stellar mass profile:

$$M_*(r)=4\,\pi\Upsilon_*\int_0^r\rho_*(r)r^2\mathrm{d}r, \tag{4.4}$$

where $\Upsilon_*\equiv(M/L)_*$ is the stellar mass-to-light ratio and it will be discussed further in the text.

For the dark matter, we assume a generalized Hernquist density profile (Hernquist, 1990):

$$\rho_d(r) = \rho_0 \left(\frac{r}{r_0}\right)^{-\gamma} \left[1 + \left(\frac{r}{r_0}\right)\right]^{\gamma-3} \tag{4.5}$$

where r_0 and ρ_0 are the scale radius and the characteristic density of the halo respectively. The parameter γ is the inner slope of the halo density profile. For what concerns us, we will only consider two families of dark matter halos: a cored halo with $\gamma = 0$ and a cuspy halo with $\gamma = 1$ which corresponds to a cosmological motivated NFW halo. By integrating the density through:

$$M_d(r) = 4\,\pi \int_0^r \rho_d(r) r^2 \mathrm{d}r, \tag{4.6}$$

one obtains the cumulative dark matter mass within a given radius:

$$M_{\rm NFW}(r) = 4\,\pi\, r_0^3\, \rho_0 \left[\ln\left(1 + \frac{r}{r_0}\right) - \frac{r/r_0}{1 + r/r_0}\right] \tag{4.7}$$

$$M_{\rm core}(r) = 4\,\pi\, r_0^3\, \rho_0 \left[\ln\left(1 + \frac{r}{r_0}\right) - \frac{r(2r_0 + 3r)}{2(r_0 + r)^2}\right] \tag{4.8}$$

for a NFW halo and a cored halo respectively.

The free parameters of our mass modelling are: the DM characteristic radius r_0, the DM characteristic density ρ_0 and the orbital anisotropy β. The stellar mass-to-light ratio in the B-band, $\Upsilon_{*,B}$, is also set as a free parameter for the modelling of the stars only, because we want to put broad constrains on this value and see how it compares with stellar population synthesis (SPS) predictions. We will then use our best-guess $\Upsilon_{*,B}$ as a fixed parameter for the modelling of the GCs.

In summary, for each potential tracer: *1)* we assume two families of dark matter haloes and one with no dark matter; *2)* we construct a grid of free parameters for the stellar component (that is: $r_o, \rho_0, \beta, \Upsilon_{*,B}$), and for the GCs (that is: r_o, ρ_0, β); *3)* we solve the Jeans equations in order to obtain the projected line-of-sight velocity dispersion; *4)* we compare the model velocity dispersion profile to the observed velocity dispersion profile via a χ^2 statistics.

4.3.1 Dealing with kinematic substructures

We have shown that the velocity dispersion profile of both the stellar component and of the red GCs are structured. The velocity dispersion bumps are probably linked to some gravitational interaction (minor merger or accretion) with other galaxies/galaxy. At this stage we do not know if the substructures of the stars and of the red GCs are different manifestations of the same event.

The presence of substructures violates the assumption of equilibrium of the Jeans equations. In

theory, one could alleviate this problem by generalizing the Jeans equations through the addition of streaming motion terms (Falco et al., 2013b). This non-equilibrium Jeans equation has been tested and applied only to galaxy clusters (Falco et al., 2013a). The fact that the solutions to Jeans equations with and without equilibrium returns consistent results when applied to the Coma cluster is reassuring. However it is not clear if this consistency holds true also at galaxy scales. Mass modelling of the Milky Way has shown that kinematic substructures do not impact the final result strongly (Deason et al., 2012), but this will depend on the amplitude of the substructures.

For our specific case, we follow the argument of Kafle et al. (2012), who suggest excluding the substructures from the analysis if these are caused by one massive accretion event. Conversely, if the substructures are superimposition of many events, one should probably include them in the modelling. At this stage we ignore the number of accretion events causing the observed substructures. Therefore we will try both approaches. In other words, we will model the stellar component and the red GCs twice: fitting the whole velocity dispersion profile first, and later masking the substructures. To keep things simple we will mask substructures on the binned velocity dispersion profile, because masking in phase-space would require a more complex approach (Romanowsky et al., 2011).

While writing this paper, Phoebe Schauer et al. (2013) published the results of N-body simulations, which may explain multiple velocity dispersion bumps in NGC 1407 as the signature of a major merger event. They also suggest that the amplitude and position of the bump is linked to the kinematics of the disk stars of the progenitor galaxy. Interestingly, the stellar kinematic substructures do not propagate to the DM, which seems to be undisturbed by the merger.

4.4 Results

In this section we present the results from the dynamical modelling of our three gravitational tracers separately. The best-fit to the dynamical models was sought by minimizing the χ^2 of a multi-parameter grid which can have up to four free parameters: r_0, ρ_0, β and Υ_*. We impose the following constrains on the parameters: $1\,\mathrm{kpc} \leq r_0 \leq 1000\,\mathrm{kpc}$, $0.0001 M_\odot\,\mathrm{pc}^{-3} \leq \rho_0 \leq 2 M_\odot\,\mathrm{pc}^{-3}$, $-10 \leq \beta < 1$ and $5\Upsilon_{\odot,B} \leq \Upsilon_{*,B} \leq 12\Upsilon_{\odot,B}$.

4.4.1 Stellar component

We run three different dynamical models for the stellar component. The first model assumes no dark matter, because we want to test if some additional dark mass is needed within the radial extent of our stellar velocity dispersion profile ($\sim 2.5 R_e$). In this case we only have two free parameters: β and Υ_*. For the remaining models we will assume a cored and a cuspy DM halo. The free

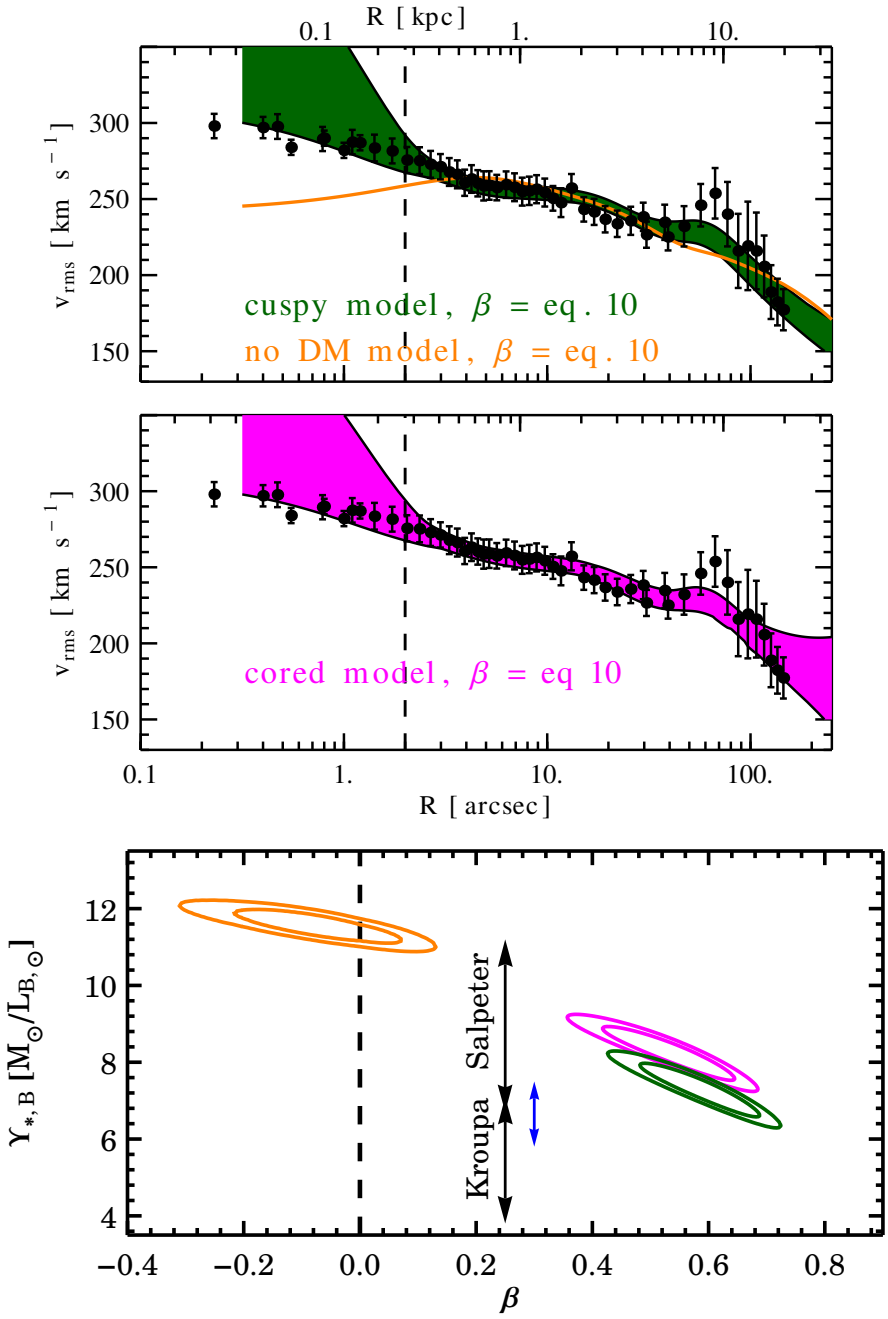

Figure 4.4 Stellar component results. *Top panel:* best-fit to the stellar velocity dispersion profile assuming no DM, a cored and a cuspy DM halo respectively. The plot is the same as Figure 4.1, with all data points coloured in gray. Dashed curves represent extrapolated models at $R < 2$ arcsec, for which data were not fitted. Data can be fitted equally well with a cuspy and a cored halo. *Bottom panel*: Orbital anisotropy vs. stellar mass-to-light ratio $\Upsilon_{*,B}$. Colours are as in the top panel. Black arrows indicate the range of $\Upsilon_{*,B}$ predicted by SPS models of Zhang et al. (2007) assuming a Kroupa and a Salpeter IMF. The blue arrow indicates the range of $\Upsilon_{*,B}$ obtained in Rusli et al. (2013b) at an arbitrary β. The horizontal line indicates isotropy.

parameters in this case are ρ_0, r_0, β and Υ_*. For all stellar dynamical models, we will exclude from the fit datapoints within the stellar core radius, $R_c \approx 2$ arcsec, because our assumption of constant orbital anisotropy is likely not to hold within this radius. The work of Thomas et al. (2013) suggests that dynamical models that include the central supermassive black hole and DM, return very tangential orbits ($\beta < 0$) within the core radius R_c and radial orbits ($\beta > 0$) for $R > R_c$. Therefore, we will keep things simple and assume that $\beta =$ const for $R > R_c$.

The best-fit velocity dispersions are shown in Figure 4.4. The corresponding best-fit halo parameters are presented Figure 4.5 together with the solutions of GCs, that will be discussed later in the text. It is clear that the models without DM cannot reproduce the data outside 40 arcsec, meaning that some additional matter is needed outside this radius. For the non-DM model, we find $\beta = -0.07^{+0.05}_{-0.14}$ and $\Upsilon_{*,B} = 11.6^{+0.3}_{-0.2}\Upsilon_{\odot,B}$. Models with a cored or a cuspy DM halo can fit the data equally well, but the cored halo has a χ^2 per degree of freedom $(\chi^2/\mathrm{dof}) = 0.26$ smaller than that for the NFW halo $(\chi^2/\mathrm{dof}) = 0.33$. The fitted NFW halo is more compact than ΛCDM predictions using WMAP5 results (Komatsu et al., 2009) with the cosmological parameters of Macciò et al. (2008). The cored halo is one order of magnitude denser than the cuspy halo to compensate for the deficit of dark matter in the inner regions.

The bottom panel of Figure 4.4 shows that the best-fit orbital anisotropy for our DM models falls in the range $0.4 < \beta < 0.7$, which implies radially biased orbits. Inside the core radius, the velocity dispersion produced by our model with constant radial anisotropy is larger than the data. Tangential orbits, coupled with the flat surface brightness within this radius, are required to lower the model velocity dispersion profile. This is fully consistent with stellar orbits becoming tangential within the stellar core radius (Thomas et al., 2013).

Although we cannot constrain the stellar mass-to-light ratio, our model solutions prefer a Salpeter IMF while being marginally consistent with a Kroupa IMF, where we have used the SPS estimates of Zhang et al. (2007). Our dynamical $\Upsilon_{*,B}$ is larger than that predicted by Rusli et al. (2013b). However, it should be noted that their modelling focuses in the innermost 100 arcsec and that it also includes the mass of the central supermassive black hole, that we exclude from our model for simplicity. It turns out that the central black hole has a mass $M_{\mathrm{BH}} = 4.5^{+5.4}_{-4.1} \times 10^9 M_\odot$ and it is among the most massive found so far. Therefore, the inclusion of a central point of mass in the modelling, can increase the total mass and lower the stellar mass-to-light ratio. Lastly, the parametrization of the DM density profile used by Rusli et al. (2013b) is slightly different from our generalized Hernquist model and this can also have an impact on the inferred dynamical Υ_*. For what concerns us, these differences in Υ_* will have a small impact on our final results, because they do not alter the location of the pinch radii and because we will consider a much wider range of Υ_* when studying the slope of the DM component.

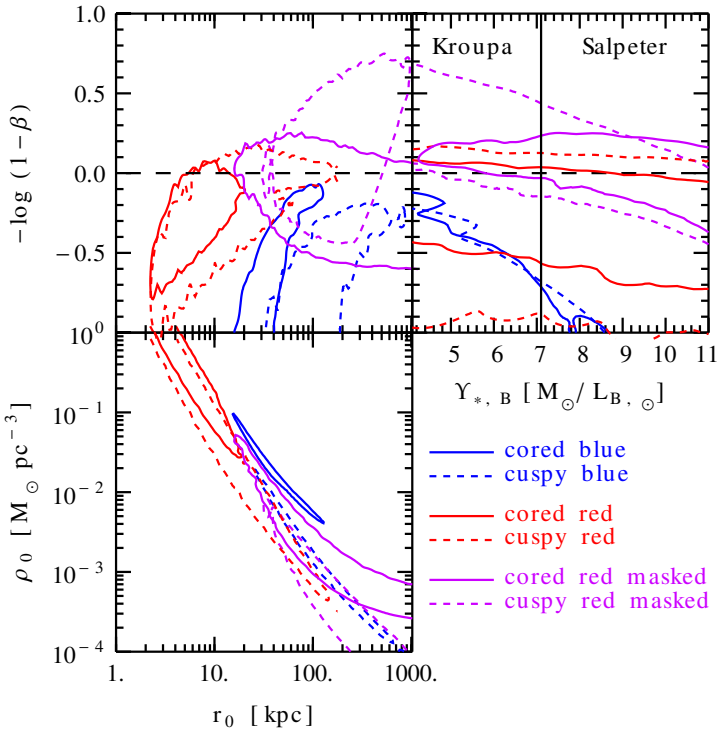

Figure 4.5 Best-fit parameters for stars and globular clusters. The plot shows the 68 per cent confidence contours for (r_0, ρ_0) marginalized with respect to β (*top panel*), and (r_0, β) marginalized with respect to ρ_0 (*bottom panel*). Models are labelled on the top right. The horizontal dashed line indicates isotropy $(\beta = 0)$.The black line $\pm 1\sigma$ marks the ΛCDM predictions assuming a WMAP5 cosmology.

Fitting the stellar component after masking the kinematic substructures in the range 80 arcsec $< R < 110$ arcsec alters the best fit r_0 and ρ_0 by less than 1 sigma, whereas the stellar mass-to-light ratio is ~ 15 per cent higher than the model which includes the kinematic substructures.

For the modelling of the GCs, we will assume a stellar mass-to-light ratio averaged between the DM solutions discussed so far, that is $\Upsilon_{*,\mathrm{B}} = 7.7 \pm 0.5\, \Upsilon_{\odot,B}$.

4.4.2 Globular clusters

Blue and red GCs were modelled similarly to the stellar component, except for the fact that the stellar mass-to-light ratio was fixed to $\Upsilon_{*,B} = 7.7\, \Upsilon_{*,B}$. The solutions to the Jeans equations for the blue and the red GCs are shown in Figures 4.5 and 4.6.

The blue GC velocity dispersion profile can be fitted equally well with a cuspy and with a cored halo. The NFW solution for blue GCs is lower than ΛCDM predictions, as found for the stars. As for the stars the $(\chi^2/\,\mathrm{dof})$ for a cored DM halo is ~ 0.4 dex smaller than that for a NFW

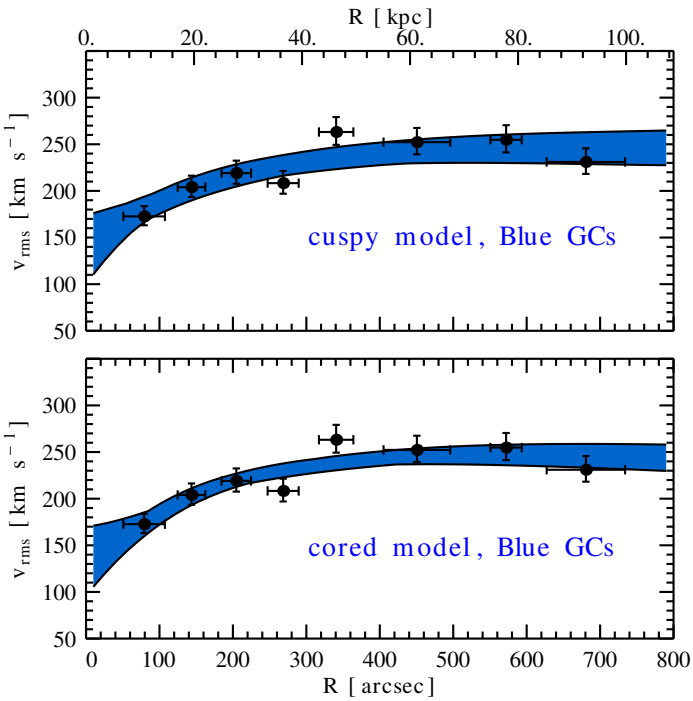

Figure 4.6 Globular cluster results. The *top* and *bottom* panels show the best-fit to the red GC (red points) and blue GC (blue points) velocity dispersion profiles respectively. The stellar velocity dispersion profile is also shown in grey for comparison. The adopted DM haloes are labelled on the top right. A cuspy and cored dark matter halo can fit the data equally well.

halo. The orbital anisotropy for the blue GCs is always tangentially biased to accommodate for the increasing velocity dispersion profile. We find $\beta = -1.6$ and $\beta = -3.7$ for a cored and NFW halo respectively. The latter is in very good agreement with the value found in Romanowsky et al. (2009), that assumed a NFW halo.

The Jeans solutions for the red GCs (including the kinematic substructures) assume more extreme values, about three orders of magnitudes more compact than the solutions for stars and blue GCs. The choice of the DM halo produces equally good fits to the data and in this case the (χ^2/ dof) is identical for a cored and a NFW halo. We constrain the anisotropy of the red GCs to be tangential, for both DM haloes.

Although the Jeans solutions for the red GCs can reproduce the declining velocity dispersion trend, the fact that they are so extreme is worrying. We speculate that this is due to the kinematic, and possibly spatial, substructures which violate the condition of equilibrium required by the Jeans equations. Excluding the datapoints that contain substructures (as shown in Figure 4.4) the Jeans solutions return more meaningful results, about one order or magnitude smaller for ρ_0 and two times larger for r_0, that makes it consistent with ΛCDM predictions. Moreover, the modelling masking the substructures can reproduce the overall stellar velocity dispersion profile, although this was not specifically included in the modelling of the red GCs. Neither model for the red GCs (including or excluding the substructures) can be correct, because we are using the same density profile for both as it is not clear if this is structured or not. We will discuss how this impacts our results in the next Section.

4.5 Constructing the mass profile of NGC 1407

We have shown that the solutions to the Jeans equations return very different dark matter haloes and orbital anisotropies depending on the potential tracers. We can now combine all this information together and seek the radius within which the uncertainties from our modelling assumptions are minimized.

4.5.1 Deriving the "pinch radii"

One of our modelling assumptions is that the total mass of NGC 1407 is $M_{tot} = (\Upsilon_* \times L_*) + M_d$. Here we are mostly interested the dark matter mass M_d, which can be trivially obtained by subtracting the stellar mass off the total mass. In §4.4.1 we have shown that the modelling of the stellar component favors a Salpeter-like IMF and we have used a bona-fide value of $\Upsilon_{*,B} = 7.7\Upsilon_{\odot,B}$ for the modelling of the GCs. Before drawing the best fit mass profiles from our Jeans modelling, we first need to re-model the stellar component fixing $\Upsilon_{*,B} = 7.7\Upsilon_{\odot,B}$ so that the

stellar mass contributes in the same measure to all three gravitational tracers. This affects the DM scale parameters and the anisotropy of the stellar component by less than 1σ.

The cumulative stellar mass profile and the DM profile for stars, blue and red GCs is shown in Figure 4.7. The effect of choosing a different stellar mass-to-light ratio will be discussed further in the text, but we anticipate that this does not alter the location of the pinch radii, but it rather affects the normalization of the profile at these radii.

A glance at Figure 4.7 reveals that each potential tracer is characterized by very different mass profiles. The uncertainty on the mass profile at a given radius is mainly driven by our the choice of the dark matter halo shape (i.e. NFW or cored). In this context, the contribution of the mass-anisotropy degeneracy on the error budget of our mass profiles is only a secondary effect. The overall DM profile of stars and blue GCs is qualitatively similar, $\approx 7 \times 10^{12} M_{\odot}$ at 100 kpc, but the DM mass profile drawn from the red GCs is one order of magnitude lower at this radius.

We also note that, for each potential tracer, the uncertainty on the *total* mass profile is minimized at one specific radius as theoretically expected from the manipulation of the Jeans equations (Wolf et al., 2010). We define the *pinch radius* r_P as the radius at which the uncertainties from our ignorance of the central slope of the DM profile γ and of r_0, ρ_0, β are minimized.

The derivation of the pinch radii for stars and GCs is schematized in Figure 4.8, as the percentage error on the DM mass profile as a function of galactocentric radius. We stress that the combination of a cored and NFW haloes is the key factor to reduce the uncertainties from 100% at the innermost or outermost regions down to 25% at the pinch radius.

The pinch radii of blue GCs and stars is well defined at $r_P = 477$ arcsec ≈ 64 kpc and $r_P = 150$ arcsec ≈ 20 kpc respectively. Normalizing these values at the 2D effective radius of the tracer, we find $r_P/R_e = 1.9$ for the stars and $r_P/R_e = 1.3$ for the blue GCs respectively. The latter is in agreement with the prediction of Wolf et al. (2010), in which the pinch radius is expected at $r_p \approx 1.3R_e$. In this framework, the pinch radius of the stars is larger than the prediction. However, the estimator of Wolf and collaborators was inferred using a single component Sèrsic fit (i.e., what we have used for the blue GCs), and it is not clear if this prediction holds true also for the three-component fit we adopted for the stellar surface brightness.

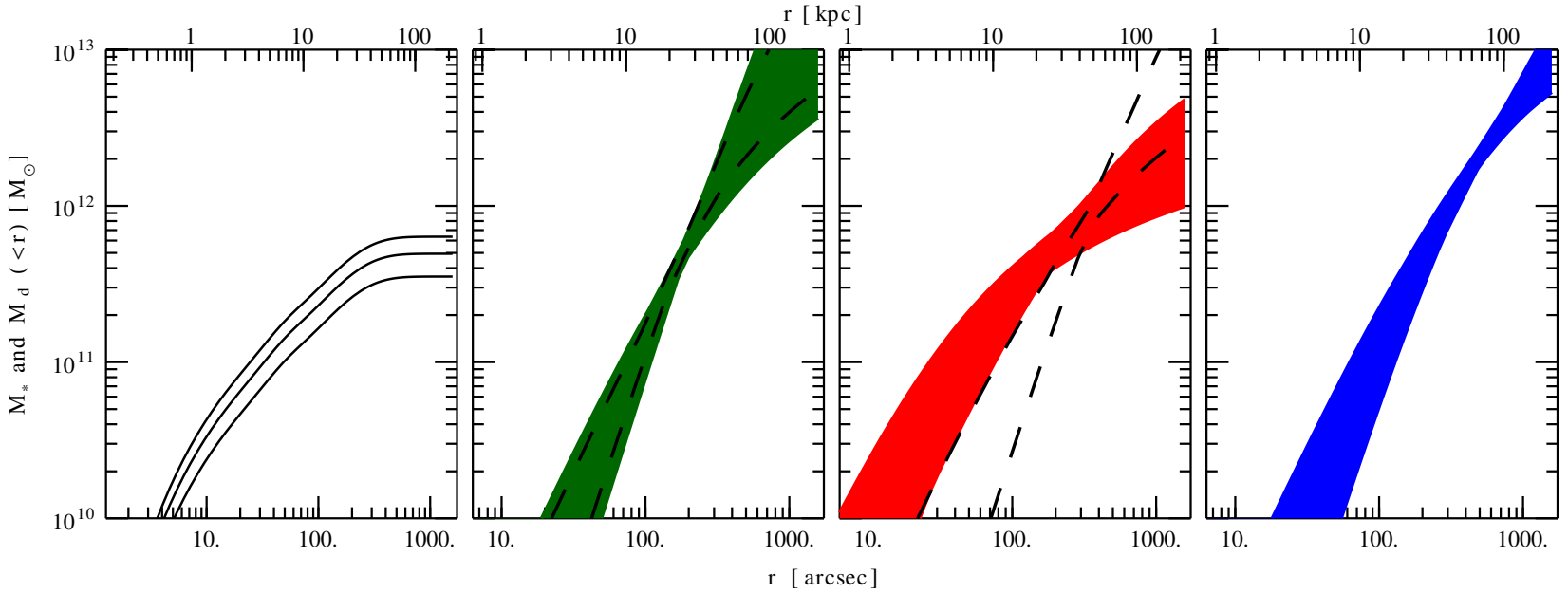

Figure 4.7 Cumulative mass profiles. The left panel shows the cumulative stellar mass $M_* = L_* \times \Upsilon_{*,B}$ for the range $6\Upsilon_{\odot,B} < \Upsilon_{*,B} < 10\Upsilon_{\odot,B}$. The black arrow indicates the mass of the central supermassive black hole at the origin. Remaining panels show the cumulative dark matter profile for the stellar component (gray), red GCs (red) and blue GCs (blue) respectively. These were obtained as $M_d = M_{tot} - M_*$, assuming a stellar mass-to-light ratio of $\Upsilon_{*,B} = 7.7\Upsilon_{\odot,B}$. The filled and dashed lines represent the DM mass profile for a cuspy and a cored halo respectively. Coloured regions are the 68 per cent confidence regions.

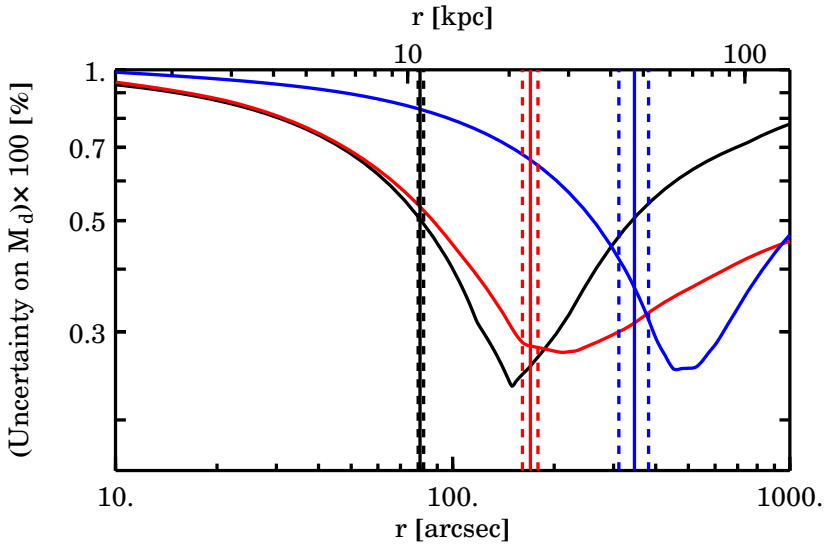

Figure 4.8 Uncertainty on the dark matter mass. Shown is the percentage error on the dark matter mass as a function of galactocentric radius. Black, red and blue lines refer to stars, red GCs and blue GCs. The vertical lines with errors represent the 2D projected effective radii of the three tracers. The uncertainty on the DM mass is minimized at one specific radius.

The pinch radius of the red GCs, $r_P = 270$ arcsec $= 36$ kpc and $(r_P/R_e = 1.6)$, is not well defined as expected from the rather extreme Jeans solutions discussed in §4.4.2 and from the peculiar DM profile seen in Figure 4.7. If we consider the Jeans solution masking the kinematic substructures, we obtain $r_P = 400$ arcsec and an uncertainty at this radius of 31%, the largest among the three tracers.

4.5.2 The effect of the stellar mass-to-light ratio

We have shown that the mass within the pinch radius is much more accurate than the mass within any other radius within the galaxy. However, this does not take into account the uncertainty on the stellar mass-to-light ratio.

There exists a well known degeneracy between the inner slope of the DM halo and Υ_* (Newman et al., 2013), such that an higher Υ_* will produce shallower DM haloes. For the specific case of NGC 1407, the effect of the stellar mass is expected to be stronger for the stellar component, because at its pinch radius the DM contributes to ≈ 50 per cent of the total mass. Whereas at the pinch radius of the blue GCs, the DM makes up 77 per cent of the total mass. The chosen Υ_* does not impact the location of the pinch radius, but it rather affects normalization of the DM mass within it.

As the *total mass* within the pinch radius is minimally affected from our modelling assump-

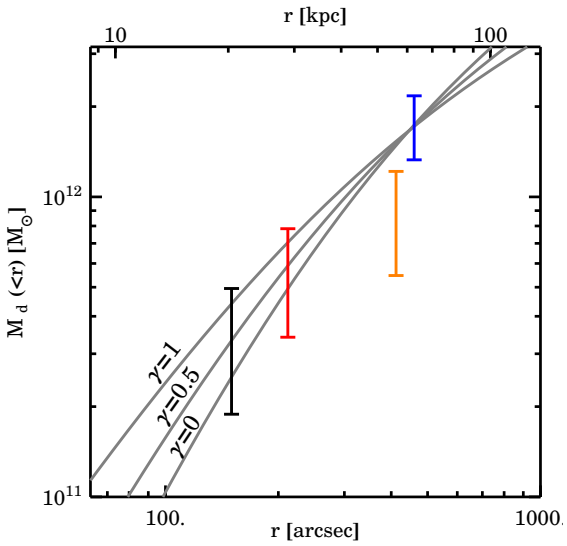

Figure 4.9 Cumulative mass profile of NGC 1407. Shown are the DM mass enclosed within the pinch radii of stars (black), red GCs including (red) and excluding (orange) the substructures in the modelling and of blue GCs (blue). The error bar on the mass profile takes into account both the uncertainty from our dynamical modelling and a stellar mass-to-light ratio varying between $5\Upsilon_{\odot,B} \leq \Upsilon_{*,B} \leq 10\Upsilon_{\odot,B}$. Gray lines are illustrative DM mass profiles with a central cusp ($\gamma = 1$) and with a flat core ($\gamma = 0$). A halo shallower than a NFW is always preferred for the assumed Υ_* range.

tions, we can subtract a reasonable range of Υ_* off the total mass to see how this impact the slope of the DM mass using $M_d = M_{tot} - (\Upsilon_* \times L_*)$. We chose the generous range $5\Upsilon_{\odot,B} \leq \Upsilon_{*,B} \leq 10\Upsilon_{\odot,B}$, which encompasses the range of solutions predicted from our mass modelling (see Figure 4.4), and the values expected by the heavy end of an assumed Kroupa IMF and the predictions from a Salpeter IMF. This range also includes the solution of the modelling of Rusli et al. (2013b), $\Upsilon_{*,B} = 6.6\Upsilon_{\odot,B}$.

The results of this exercise are shown in Figure 4.9. Here the uncertainty on the DM mass within the pinch radii includes both the uncertainty from our modelling assumption (Figure 4.8) and the uncertainty of a stellar mass-to-light ratio varying between $5\Upsilon_{\odot,B} \leq \Upsilon_{*,B} \leq 10\Upsilon_{\odot,B}$.

It is already evident from Figure 4.9 that haloes shallower than a cusped cuspy-NFW halo ($\gamma \geq 1$) are preferred. It is also clear that the pinch radius of the red GCs contains less mass than expected, assuming that the solutions for stars and blue GCs are correct and not affected by the kinematic substructures. This anomalous behavior of the red GCs was expected by the deficit of mass observed in Figure 4.7, by the loosely constrained pinch radius and by the extreme solutions of the Jeans modelling. For all these reasons, from now on we will exclude the red GCs from the study of the DM profile.

4.5.3 The dark matter profile of NGC 1407

We can now study all possible DM haloes that can fit the datapoints in Figure 4.9 assuming different stellar mass-to-light ratios. In order to make the comparison with literature easier, we will adopt three different parametrizations of the DM halo. The first model is the Hernquist model that we have adopted throughout this paper. The key parameter is now the the inner slope of the density profile γ, that we will leave as a free parameter, together with the radius r_0 and the density ρ_0. By integrating Equation 4.5, we obtain the cumulative DM mass for a generalized Hernquist profile:

$$M_{\rm Hern}(r) = \frac{4\pi G \rho_0 r_0^3}{\omega} \left(\frac{r}{r_0}\right)^{\omega} {}_2F_1 \left[\omega, \omega; \omega; -\left(\frac{r}{r_0}\right)\right] \tag{4.9}$$

where and $\omega = 3 - \gamma$ and ${}_2F_1$ is a Gauss' hypergeometric function.

The second halo is a cored-logarithmic halo, known as LOG halo (Binney & Tremaine, 1987), with mass:

$$M_{\rm LOG}(r) = \frac{1}{G} \frac{v_0^2 r^3}{r_0^2 + r^2}, \tag{4.10}$$

where v_0 and r_0 are the asymptotic circular velocity and core radius of the halo. This parametrization assumes a DM core ($\gamma = 0$) and it is the one adopted by Rusli et al. (2013b). Unlike the NFW, that decreases as r^{-3}, the LOG halo decreases as r^{-2} and in many cases it has been shown to fit the data better than a NFW (e.g., Fall & Efstathiou, 1980; Thomas et al., 2007; Napolitano et al., 2011).

The third DM halo is a cored NFW (cNFW, Newman et al., 2013). The cumulative DM mass for this model is algebraically complicated, and here we report the radial density only:

$$\rho_{\rm cNFW}(r) = b\,\rho_0 \left(1 + \frac{b\,r}{r_0}\right)^{-1} \left(1 + \frac{r}{r_0}\right)^{-2}, \tag{4.11}$$

where ρ_0 and r_0 and the characteristic density and radius respectively, while the dimension-less quantity b defines the DM core radius as $r_{\rm core} = r_0/b$. This is will allow us to compare the size of the DM core with the measurements of Newman et al. (2013) in lensed galaxy clusters.

We perform a χ^2 fit to the three haloes above letting all parameters free to vary. Results are shown in Figure 4.10. Here we show the slope γ, the core radius from the LOG model r_0 and the core radius from the cNFW model $r_{\rm core}$ as a function of the assumed stellar mass-to-light ratio. As already suggested in Figure 4.9, the slope γ is biased toward negative values, but it is still consistent with a cusped halo up to $\Upsilon_{*B} < 6.5\Upsilon_{\odot,B}$. For larger values (i.e., consistent with a Salpeter IMF or heavier) the halo of NGC 1407 is significantly shallower than a NFW (i.e., $\gamma < 1$).

For each halo, we compute some important dynamical quantities, shown in Table 4.2. These include the virial radius $r_{\rm vir}$, i.e. the radius at which the density of the halo is $\Delta_{\rm vir} = 101$

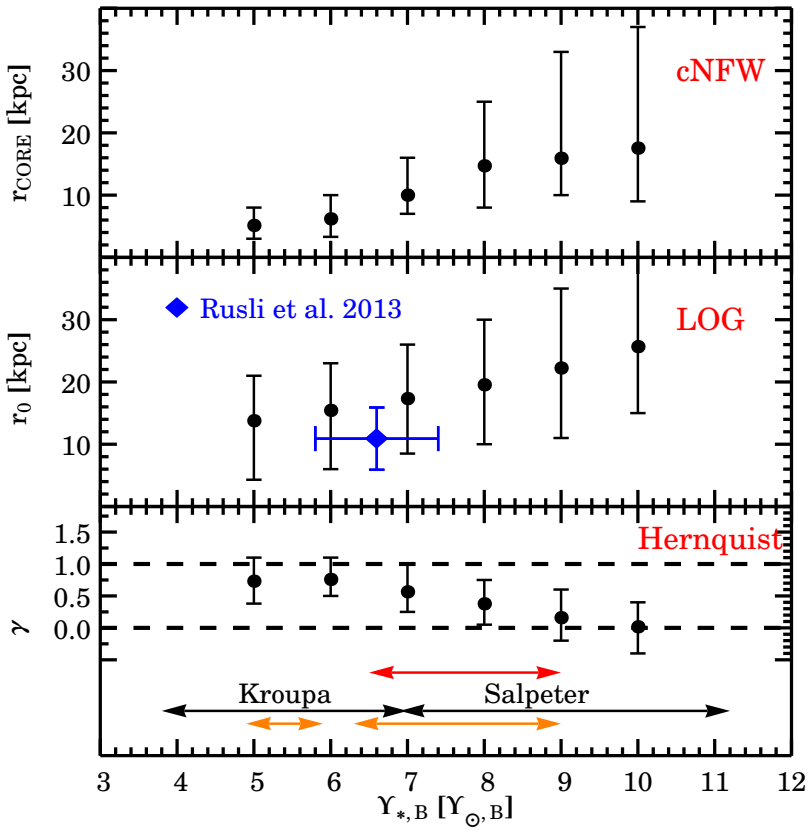

Figure 4.10 Best fit DM halo parameters. Shown are the inner slope γ of the Hernquist halo, the core radius r_0 of the LOG halo and the core radius $r_{\rm core}$ of the cNFW halo as a function of the stellar mass-to-light ratio $\Upsilon_{*,B}$. Left and right arrows indicate the range of predicted $\Upsilon_{*,B}$ assuming a Kroupa or a Salpeter IMF respectively. Black and orange arrows are SPS predictions from Zhang et al. (2007) and Humphrey et al. (2006) respectively. The red arrow marks the range of dynamical $\Upsilon_{*,B}$ from this paper. Horizontal lines mark a cusped halo with $\gamma = 1$ and a cored halo with $\gamma = 0$. The central panel shows the prediction of Rusli et al. (2013b), for which we assumed a $\pm 5\,{\rm km\ s^{-1}}$ error to guide the eye because these authors do not quote the uncertainty on r_0.

DM halo	$r_{\rm vir}$ [kpc]	$\log M_{\rm vir}$ $[M_\odot]$	$c_{\rm vir}$	$f_{\rm DM}(5R_e)$	$\Upsilon(r_{\rm vir})$ $[\Upsilon_{\odot,B}]$
Hernquist	580 ± 200	13.1 ± 0.4	18 ± 4	0.7 ± 0.4	150 ± 35
LOG	730 ± 150	13.6 ± 0.5	$-$	0.8 ± 0.3	323 ± 65
cNFW	560 ± 180	13.0 ± 0.4	21 ± 4	0.7 ± 0.4	137 ± 38

Table 4.2 Important dynamical quantities for different DM haloes in NGC 1407. From the left to the right we show the virial radius, the total mass at this radius, the concentration parameter, the fraction of DM at $5R_e \approx 55$ kpc and the dynamical mass-to-light ratio at the virial radius. A stellar mass-to-light ratio of $\Upsilon_{*,B} = 8\Upsilon_{\odot,B}$.

times the critical density $\rho_{\rm crit} = 1.37 \times 10^{-7} M_\odot$ pc^{-3} of the Universe. It follows that the virial mass is $M_{\rm vir} = 4\pi\Delta_{\rm vir}\rho_{\rm cri}r_{\rm vir}^3/3$ and the concentration parameter is $c_{\rm vir} = r_{\rm vir}/r_0$ (applicable to the Hernquist and cNFW haloes only). We also show the fraction of DM at 5 R_e, that is $M_d(5R_e)/M_{\rm tot}(5R_e)$, and the total dynamical mass-to-light ratio at the virial radius, that is $M_{\rm tot}(r_{\rm vir})/M_*(r_{\rm vir})$.

4.6 Discussion

4.6.1 The role of the IMF

Although we were able to minimize the uncertainties from modelling assumptions on the mass profile of NGC 1407, the larger source of uncertainty in our analysis is the stellar mass-to-light ratio and hence the IMF. If the IMF is Salpeter-like or heavier, the DM of NGC 1407 has a central core, whereas if the IMF is Kroupa-like, the DM halo is consistent with a cuspy-NFW halo.

Recent studies (Thomas et al., 2011; Wegner et al., 2012; Cappellari et al., 2012, 2013; Conroy & van Dokkum, 2012; Conroy et al., 2013; Tortora et al., 2013), all suggest that the IMF becomes heavier (i.e. Salpeter-like) in galaxies with high stellar velocity dispersion. The luminosity-weighted velocity dispersion of NGC 1407 from §4.2.3 is $\langle\sigma\rangle = 260\,{\rm km\ s^{-1}}$. Using the results of Conroy et al. (2013), our $\langle\sigma\rangle$ implies $7.3\Upsilon_{\odot,B} \leq \Upsilon_{*,B} \leq 9.3\Upsilon_{\odot,B}$. This range includes both their dynamical and photometric mass-to-light ratios.

For the specific case of NGC 1407, the SPS predictions of Humphrey et al. (2006) give $\Upsilon_{*,B} = 5.4 \pm 0.5\Upsilon_{\odot,B}$ and $\Upsilon_{*,B} = 7.8^{+1.2}_{-1.5}\Upsilon_{\odot,B}$ for a Kroupa and a Salpeter IMF respectively. These are also shown in Figure 4.10, together with the predictions of Zhang et al. (2007) that we discussed early in the text.

By averaging the Υ_* solutions from our mass modelling (see Figure 4.4), we found $\Upsilon_{*,\rm B} = 7.7 \pm 0.5\ \Upsilon_{\odot,B}$, which is fully consistent with a Salpeter IMF from the predictions above. Lastly, the modelling results the stars excluding the velocity dispersion bump produces $\Upsilon_{*,B}$ values that

are ∼15 per cent higher.

In conclusion, although we can not constrain the stellar mass-to-light ratio of NGC 1407, we can confidently state that the IMF of NGC 1407 is Salpeter-like and the stellar mass-to-light ratio is at least $\Upsilon_{*,\mathrm{B}} > 7\ \Upsilon_{\odot,B}$, meaning that the DM halo of NGC 1407 has a central core. For the analysis below, we will assume that the "true" $\Upsilon_{*,B}$ of NGC 1407 as the average between the SPS predictions (assuming a Salpeter IMF) and our dynamical results. This gives $\Upsilon_{*,\mathrm{B}} = 8\ \Upsilon_{\odot,B}$. With this assumption, we find $\gamma = 0.51^{+0.31}_{-0.28}$ and $r_{\mathrm{core}} = 13^{+9}_{-5}$ kpc.

4.6.2 Core formation

This study was motivated by the ongoing controversy between theory, which predicts DM halo cusped at the centre of galaxies, and observations, that measure cored DM halos in dwarf ellipticals, spiral galaxies and galaxy clusters. An increasing number of computer simulations, that include both DM and baryonic physics, converge towards the idea that feedback can evacuate the DM from galaxy centres. In dwarf galaxies, supernovae feedback with energy $E \sim 10^{53-55}$ erg can create a DM core (Governato et al., 2012; Pontzen & Governato, 2012; Teyssier et al., 2013; Di Cintio et al., 2013), but in order to reproduce observations, the contribution from a peculiar star formation history and DM satellite disruption are also required (Peñarrubia et al., 2012). In normal galaxies and cluster of galaxies, the required energy to remove the cusp comes from AGN feedback (Mead et al., 2010; Martizzi et al., 2012, 2013) triggered by high metallicity cold gas clumps falling into the central supermassive black hole.

There is strong evidence that NGC 1407 was, and still is, an active radio galaxy. Using the Giant Metrewave Radio Telescope (GMRT), Giacintucci et al. (2012) identified multiple radio outbursts in NGC 1407: one diffuse radio emission is linked to an AGN activity at least 300 Myr old, while a compact-double radio source is only 30 Myr old, and consistent with being still active. The first and the second outbursts have released an energy of $E \sim 10^{57}$ erg and $E \sim 10^{58}$ erg respectively, which is of the order of the energy required to produce DM cores in computer simulations.

In the simulations of Martizzi et al. (2012, 2013), the DM density profile starts flattening at $r \approx 20$ kpc, which is in good agreement with the size of the core radius found in this study. This holds true even assuming a much higher Υ_* (see Figure 4.10). The uncertainty on our estimate of γ is still too large to distinguish between the FAST model (in which gas clumps fall into the SMBH short galactocentric distances) and SLOW model (large galactocentric distances) in the models of Martizzi and collaborators. However, the same simulation predicts that the size of the *stellar* core should be similar to that of the DM. The central stellar core of NGC 1407 is $R_{\mathrm{core},*} = 0.2$ kpc (see Figure 4.1), about one order of magnitude smaller than the DM core. This means that

the mechanism that evacuate matter from the galaxy centre, affected dark and luminous matter differently. Future theoretical works will have to explain this discrepancy.

Besides baryonic feedback, other physical processes have been proposed to explain the formation of DM cores. These include the existence of warm dark matter particles (e.g., Menci et al., 2012), decaying dark matter particles (e.g., Peter et al., 2010) or self-interacting DM (Rocha et al., 2013; Peter et al., 2013). The self-interacting scenario is the most attractive because, if the cross-section of the DM particle is ~ 0.1 cm^2 g^{-1}, it is able to produce ~ 20 kpc DM cores in galaxy clusters, in agreement with our findings, without violating the ΛCDM framework. In this context, the AGN feedback and self-interacting scenarios produce indistinguishable predictions.

4.6.3 Comparison with previous studies

To date, the inner slope of the DM profile, γ, has been measured in almost all galaxy types, except in giant ellipticals. Using THINGS data (Walter et al., 2008), Oh et al. (2011) and Chemin et al. (2011) were able to measure γ in dwarf ellipticals (dEs) and spiral galaxies respectively. Their estimates of γ have small error bars due to sthe high quality HI maps of their galaxies. Their results imply DM profiles consistent with cores, with a few exceptions. Similar results were obtained in low surface brightness (LSB) galaxies by deBlok & Bosma (2002). Walker & Peñarrubia (2011) and Amorisco & Evans (2012) measured γ in the Fornax and Sculptor dwarf spheroidals (dSphs) with much larger uncertainties, but their results were still suggestive of DM cores in both systems. Newman et al. (2013) measured the inner slope and the DM core radius of seven galaxy clusters and their brightest cluster galaxies (BCGs) combining stellar kinematics, multiples images from strong lensing, and weak lensing observations. These results are consistent with DM cores. Although Newman et al. (2013) assumed orbital isotropy for their modelling, adopting radial or tangential anisotropy still returns solutions with cored DM halos.

The inferred γ for dSphs, dEs, spiral galaxies and BCGs are summarized in Figure 4.11 as a function of stellar effective radius R_e of the central galaxy and of virial mass $M_{\rm vir}$. The former comes from the parent papers (if given), otherwise from the RC3 catalogue (de Vaucouleurs, 1991). For the Chemin et al. (2011) sample we used their γ and $M_{\rm vir}$ adopting a Kroupa IMF. For the sample of Oh et al. (2011), we adopted their average estimate of $\langle\gamma\rangle = -0.27 \pm 0.07$ for their seven dEs and we chose an average $\langle R_e\rangle = 0.5^{+0.4}_{-0.3}$ kpc typical for dEs. We also show our results for NGC 1407 assuming $\Upsilon_{*,\rm B} = 8\ \Upsilon_{\odot,B}$.

Our estimate of γ is in very good agreement with the average value from all literature studies. The existence of DM cores seems to hold at all galaxy scales. In this framework, the data in Figure 4.11 weaken the claimed correlation between γ and physical quantities of the baryonic matter of central galaxies (the effective radius in this case) (Del Popolo, 2012; Laporte et al.,

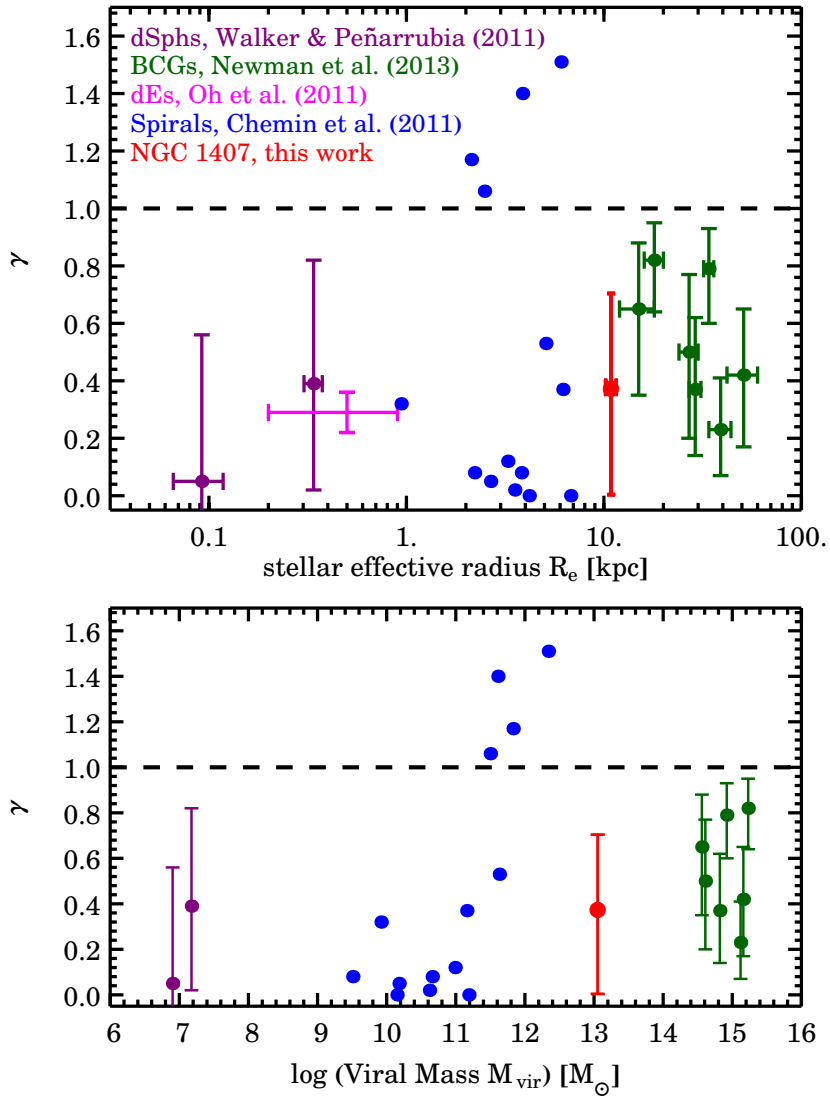

Figure 4.11 Comparison with literature studies. Note the different x-axis range. *Top* and *bottom* panels show the slope of the DM profile γ as a function of stellar effective radius R_e and virial mass $M_{\rm vir}$ of the central galaxy respectively. Colour and references are labeled in the top panel for dwarf spheroidals (dSphs), dwarf ellipticals (dEs), spiral galaxies and bright cluster galaxies (BCGs). dEs are not shown in the bottom panel because their $M_{\rm vir}$ is not quoted in the parent paper. The red point is our result for NGC 1407 assuming a stellar mass-to-light ratio of $\Upsilon_{*,B} = 8\Upsilon_{\odot,B}$. The horizontal line marks the transition from DM cores ($\gamma < 1$) to DM cusps ($\gamma \geq 1$).

2012). At cluster/galaxy scales, such a relation is expected because satellite galaxies infalling into a larger galaxy can heat the primordial cusp via dynamical friction and reduce the central DM density (e.g., Nipoti et al., 2004; Cole et al., 2011). Therefore the inner DM slope is expected to be shallower in galaxies that assembled more stellar mass. Of course, this core-formation process will also affect the infalling satellite galaxies because of their tidal interaction with the potential of the central galaxy. Therefore, we would expect the DM to be more cored in dwarf galaxies in crowded environments (i.e., clusters and groups), with respect to field dwarf galaxies. However, Del Popolo & Cardone (2012) showed that this effect is not statistically significant for a large sample of dwarf galaxies and LSB galaxies in different environments. Moreover, it not clear how the baryonic-feedback scenario (i.e. supernovae and AGN) discussed in §4.6.2 fits in this "dynamical friction" scenario. Naively, we expect them both to be true and future computer simulations will have to explain which one is the most efficient. In conclusion, it seems that the number statistics are too low and the uncertainties too large to infer any trend from Figure 4.11.

4.7 Conclusions

Motivated by the work of Walker & Peñarrubia (2011) on the dynamical modelling of two stellar subpopulations in dwarf spheroidals, we have used a novel mass modelling technique, that we dub the "pinch point technique", to study dark matter profiles with unprecedented accuracy. The advantages of this method are that the uncertainties from our choice of the exact shape of the DM halo and from the mass-anisotropy degeneracy are minimized at one particular galacocentric radius (the pinch radius). We have applied this technique to the blue and red GCs and to the stellar population of the giant elliptical galaxy NGC 1407, the dominant galaxy of the Eridanius group. We identified three pinch radii, within which the total mass of the galaxy is uncertain by ~ 25 per cent, compared to much larger values everywhere else in the galaxy.

The red GCs turned out to be disturbed, with a bumpy velocity dispersion profile, which violates the equilibrium required by the Jeans equations. Indeed, our attempt of modelling the red GCs returned very implausible results, inconsistent with those from the other two gravitational tracers. Recently, Phoebe Schauer et al. (2013) explained the observed velocity dispersion bump in NGC 1407 as the signature of a major merger.

Our results suggest that the initial mass function (IMF) of NGC 1407 is Salpeter-like, consistent with recent claims that the IMF is heavier in galaxies with high stellar velocity dispersions. With this IMF assumption, and parametrizing the inner DM density profile as $\rho \propto r^{-\gamma}$, we find that the DM halo of NGC 1407 is consistent with having a central core with slope $\gamma = 0.51^{+0.31}_{-0.28}$ assuming a stellar mass-to-light ratio $\Upsilon_{*,\mathrm{B}} = 8\ \Upsilon_{\odot,B}$. Larger and smaller $\Upsilon_{*,\mathrm{B}}$ values will produce shallower and steeper density profiles respectively.

This is the first measurement of this kind in an elliptical galaxy, and it is consistent with similar findings in dwarf galaxies, spiral galaxies and galaxy clusters. These results are in contrast with DM-only simulations that predict a central cusp. The formation of DM cores can be explained either as the effect of AGN feedback on the surrounding environment, or with other scenarios, such as warm dark matter, self-interacting dark matter or dynamical friction from infalling satellites. All these scenarios make very similar predictions on the size of the DM core ($\approx$ 20 kpc), which is consistent with our findings. Future computer simulations will have to explain the mechanisms that can produce DM cores at all galaxy scales so efficiently.

5 Conclusions

5.1 Summary

In this thesis we have studied some aspects of galaxy evolution using extragalactic globular clusters. The fundamental idea is that the study of globular cluster systems at the present time, can trace back the formation their host galaxies. This is feasible thanks to some well established properties of globular clusters, such as the colour/metallicity bimodality, their compactness and old ages, that makes these objects the ideal discrete tracers of galaxy *bulges* and galaxy *haloes*. We have focused our attention especially on galaxy *haloes* of early-type galaxies because they are hard to study with integrated stellar light, and because numerical simulations predict that they have observable signatures of their evolutionary history.

We have used a state-of-the-art spectro-photometric dataset, which is part of the ongoing SLUGGS survey. SLUGGS is the SAGES Legacy Unifying Globulars and Galaxies Survey, where SAGES is the Study of the Astrophysics of Globular Clusters in Extragalactic Systems. The photometric part comes from Subaru/Suprime Cam and is used to select GCs around the parent galaxies. These observations return magnitudes, colours, size information (if HST imaging is also available) for thousands of GCs. The spectroscopic part comes from the Keck/DEIMOS multi-spectrograph and it produces spectra for a subset of photometrically selected GCs. Spectra give radial velocities (that we have used in this work) and metallicity information (Usher et al., 2012).

This dataset (described in detail in Chapter 2) was used to study GC systems and their galaxies with three different approaches, discussed in Chapters 2, 3 and 4. We summarize below the main findings.

In Chapter 2 we have studied the kinematic properties of a sample of twelve GC systems, characterized by the finest velocity resolution and the highest number of confirmed GCs when compared to literature studies. Our main goal was to test if the bimodality seen in the colour distribution of GC systems was also present in the GC kinematics. We found that this is the case for

some systems, and it is most evident in galaxies that that exhibit some GC rotation. In the absence of rotation, the GC velocity dispersion provides further evidence for GC kinematic bimodality. The kinematics of the red GC subpopulations are strongly coupled with the host galaxy stellar kinematics. The blue GC subpopulations are more dominated by random motions, especially in the outer regions, and decoupled from the red GCs. We supplemented our galaxy sample with data from the literature and carry out a number of tests to study the kinematic differences between the two GC subpopulations. We confirm that the GC kinematics are coupled with the host galaxy properties and find that the velocity kurtosis and the slope of their velocity dispersion profiles are different between the two GC subpopulations in more massive galaxies.

However, when the studied as single cases, the observed properties of the galaxies in our sample appear very different from each other, even though their global properties appear to be ordinary (e.g., see Figure 2.16) . For instance, peculiar GC kinematic profiles are seen in some galaxies: the blue GCs in NGC 821 rotate along the galaxy minor axis, together with planetary nebulae, but differently from the kinematics of the stars. Rotation axis twists and counter-rotations were also observed in some galaxies. Moreover, we have shown that the GC system of the lenticular galaxy NGC 7457 appears to be strongly rotation supported in the outer region and we have speculated that this can be the result of a minor merger. It worth noting that the latter exercise was conducted only with 21 confirmed GCs, supporting the importance GCs to study the evolutionary history of galaxies.

We found evidence to support the existence of common patterns in the formation of the observed galaxies (with collapse and merging being the main drivers), but we also recognize that each galaxy has its unique formation history, which depends on a number of physical processes, too complex to be included in current day computer simulations. The picture emerging from Chapter 2 is that galaxies behave very differently when looked in their entirety (from the innermost to the outermost regions). This is becoming more and more evident from new observations of galaxy stellar light (e.g., Arnold et al., 2013) and from computer models that can simulate galaxies with increasing resolution. In other words, inferring the formation history of galaxies based only on field-limited observations can return misleading results.

In Chapter 3 we investigated if blue and red GCs correlate differently with the mass of the supermassive black hole (SMBH) of their host galaxy. This may be expected if they trace the potentially different formation history of the halo and of the bulge of the host galaxy respectively. We found that the mass of the SMBH correlates with the total GC system velocity dispersion, although not as strongly as previously claimed. Although there is a hint that the red GC velocity dispersion might correlate better with SMBH than the blue GC velocity dispersion, the number statistics are still too low to be certain. A dataset at least twice as large as the one discussed here

is required in order to obtain more conclusive results.

Lastly, in Chapter 4 we tackled the question: *does the dark matter at the centre of elliptical galaxies have a cusp, as predicted from DM-only simulations*? This is known as the the cusp/core problem and it is still an open question in elliptical galaxies. We have applied a novel modelling technique, that we dub the "pinch point technique", to our best GC dataset from Chapter 2: the elliptical galaxy NGC 1407. By combining the mass modelling of blue GCs, red GCs and stars of NGC 1407, we where able to infer the dark matter profile of NGC 1407 with unprecedented accuracy. Our results suggest that NGC 1407 has a DM core for a reasonable range of assumed stellar mass-to-light ratios. This result is in line with the idea that AGN feedback can carve a DM core in elliptical galaxies, similarly to what supernovae do in dwarf galaxies. In fact, there is strong evidence that the AGN of NGC 1407 was active at least ~ 200 Myr ago and that it now entered in a dying phase since then. The formation of a DM-core has been shown to be irreversible and it is unlikely that the primordial cusp will form again. In this framework, the presence of a DM core is not surprising, because it is becoming evident that the inclusion of baryons in DM-only simulations can alter the physical properties haloes themselves. Limited computing power is the only factor which prevents simulations to give observers a wider range of predictions. Baryonic-feedback is not the only core-formation scenario, but it is the only one for which we have some direct evidence.

5.2 Future directions

It is worth recalling that the data presented in this thesis were part of the ongoing SLUGGS survey. Here we have discussed only twelve of the planned twenty-five galaxies for this survey. Indeed, this is a big improvement to the datasets discussed in the PhD theses of Caroline Foster and Lee Spitler, who both called for more data when the SLUGGS survey was still in a pristine state.

The natural step forward is to carry out research similar to that conducted in Chapter 2 for the whole SLUGGS sample, which includes unpublished catalogues and improved catalogues for already published galaxies. To date, 90 per cent of the survey has been completed and we have already compiled final photometric and spectroscopic catalogues for at least six new early-type galaxies with an average number of 100 confirmed GCs per galaxy.

From an imaging point of view, the field-of-view of Subaru/SuprimeCam used in this thesis, is wide enough to encompass the whole GC system of most nearby galaxies. Nevertheless, it has been shown that the use of different pass-band filters (the u-band in particular) can improve the GC selection (Muñoz et al., 2013). This comes at the cost of longer exposure time, but it has the advantage of reducing the contamination from Galactic stars and galaxies, making the spectroscopic follow-up more efficient. Therefore, we believe that the technology needed to return

more robust results on the properties of GC systems is already in place and in fact the number of new published GC systems is increasing steadily with time. Encouraging is the fact that other groups are collecting large amount of high quality GC data (see the Next Generation Virgo cluster survey, Muñoz et al. 2013), which will help to increase GC samples.

An interesting aspect emerging from Chapter 2 is that in some galaxies the kinematics of the blue GCs are akin to the kinematics of the stars, contrary to what is typically observed in the majority of galaxies. Compelling evidence for this peculiarity was found in NGC 821 and NGC 4494. Interestingly, these two galaxies are both isolated, whereas all other GC systems studied so far belong to groups or clusters. Therefore, it would be interesting to study how (and if) the GC kinematics change with galaxy environment and if the peculiar property of NGC 4494 and NGC 821 is real or just a selection effect. On a similar line, it would be very useful to study GC system kinematics in galaxies of different morphological type. This is feasible in dwarf galaxies although the return rate is low. Unfortunately, GCs in spiral galaxies are notoriously hard to observe because of dust extinction. With the current technology it is challenging to confirm more than a few tens GCs in spiral galaxies (with the Milky Way, Andromeda and M33 being the only exceptions).

The substructures found in the GC velocity dispersion profile of some galaxies (e.g., NGC 1407) also deserve a careful analysis. The recent work of Phoebe Schauer et al. (2013) used the dataset discussed in this thesis to show that these substructures or "σ-bumps" may be linked to major merger events. The amplitude of these bumps can return information on the properties of the progenitor galaxies. A possible idea would be to develop an algorithm that identifies σ-bumps in a quantitative way, and apply this method to a large sample of GC systems. It successful, this project would be a breakthrough for galaxy formation theories, because it will be able to test several aspects of galaxy formation, such as the importance of major mergers compared to accretion, with the minimal observational effort.

From a theoretical point of view, we call for new and improved numerical simulations that predict the properties of GC kinematics in early type galaxies. To date, little improvements have been generated to the numerical simulations discussed in Section 2.6 (e.g., Kruijssen et al., 2012).

As far as the mass modelling is concerned, we are planning to extend the "pinch point technique", applied to an elliptical galaxy for the first time in Chapter 4, to all galaxies of the SLUGGS survey (and possibly from the literature) which obey the criteria of sphericity and equilibrium required from the Jeans equations. Now that cusp/core problem seems to be solved (i.e., the dark matter in galaxies seems to be cored and not cusped), improved computer simulations will have to explain the processes that can produce dark matter cores so efficiently at all galaxy scales. This is not an easy task even for the current computing power, especially if one wants to tackle all

proposed core-formation processes in a single simulation (e.g., warm dark matter, self-interacting dark matter, dynamical friction, baryonic feedback, etc.).

Bibliography

Abazajian K. N. et al., 2009, ApJS, 182, 543

Agnello A., Evans N. W., 2012, ApJ, 754, L39

Alves-Brito A., Hau G. K. T., Forbes D. A., Spitler L. R., Strader J., Brodie J. P., Rhode K. L., 2011, MNRAS, 417, 1823

Amorisco N. C., Agnello A., Evans N. W., 2013, MNRAS, 429, L89

Amorisco N. C., Evans N. W., 2011, MNRAS, 411, 2118

Amorisco N. C., Evans N. W., 2012, MNRAS, 419, 184

Arnold J. A., Romanowsky A. J., Brodie J. P., Chomiuk L., Spitler L. R., Strader J., Benson A. J., Forbes D. A., 2011, ApJ, 736, L26

Arnold J. A. et al., 2013, ArXiv e-prints

Ashman K. M., Bird C. M., Zepf S. E., 1994, AJ, 108, 2348

Ashman K. M., Zepf S. E., 1992, ApJ, 384, 50

Baba H. et al., 2002, in Astronomical Society of the Pacific Conference Series, Vol. 281, Astronomical Data Analysis Software and Systems XI, Bohlender D. A., Durand D., Handley T. H., eds., p. 298

Baes M., Buyle P., Hau G. K. T., Dejonghe H., 2003, MNRAS, 341, L44

Barr J. M., Bedregal A. G., Aragón-Salamanca A., Merrifield M. R., Bamford S. P., 2007, A&A, 470, 173

Bassino L. P., Richtler T., Dirsch B., 2006, MNRAS, 367, 156

Battaglia G., Helmi A., Tolstoy E., Irwin M., Hill V., Jablonka P., 2008, ApJ, 681, L13

Bauer A. E., Hopkins A. M., Gunawardhana M., Taylor E. N., Baldry I., Bamford S. P., Bland-Hawthorn, 2013, MNRAS, 434, 209

Baumgardt H., 1998, A&A, 330, 480

Baumgardt H., Makino J., 2003, MNRAS, 340, 227

Beasley M. A., Baugh C. M., Forbes D. A., Sharples R. M., Frenk C. S., 2002, MNRAS, 333, 383

Beasley M. A., Cenarro A. J., Strader J., Brodie J. P., 2009, AJ, 137, 5146

Beasley M. A., Forbes D. A., Brodie J. P., Kissler-Patig M., 2004, MNRAS, 347, 1150

Beasley M. A., Sharples R. M., 2000, MNRAS, 311, 673

Beasley M. A., Strader J., Brodie J. P., Cenarro A. J., Geha M., 2006, AJ, 131, 814

Begelman M. C., Volonteri M., Rees M. J., 2006, MNRAS, 370, 289

Beifiori A., Courteau S., Corsini E. M., Zhu Y., 2012, MNRAS, 419, 2497

Bekki K., 1998, ApJ, 502, L133

Bekki K., Beasley M. A., Brodie J. P., Forbes D. A., 2005, MNRAS, 363, 1211

Bekki K., Forbes D. A., Beasley M. A., Couch W. J., 2002, MNRAS, 335, 1176

Bekki K., Peng E. W., 2006, MNRAS, 370, 1737

Bekki K., Yahagi H., Nagashima M., Forbes D. A., 2008, MNRAS, 387, 1131

Bell E. F., McIntosh D. H., Katz N., Weinberg M. D., 2003, ApJS, 149, 289

Bender R., Saglia R. P., Gerhard O. E., 1994, MNRAS, 269, 785

Bergond G., Zepf S. E., Romanowsky A. J., Sharples R. M., Rhode K. L., 2006, A&A, 448, 155

Bertola F., Pizzella A., Persic M., Salucci P., 1993, ApJ, 416, L45

Binney J., Tremaine S., 1987, Nature, 326, 219

Binney J., Tremaine S., 2008, Galactic Dynamics: Second Edition. Princeton University Press

Blom C., Spitler L. R., Forbes D. A., 2011, MNRAS, 2118

Bournaud F., Elmegreen B. G., Elmegreen D. M., 2007, ApJ, 670, 237

Bournaud F., Jog C. J., Combes F., 2005, A&A, 437, 69

Box M. J., 1971, Journal of the Royal Statistical Society. Series B (Methodological), 33, pp. 171

Boylan-Kolchin M., Bullock J. S., Kaplinghat M., 2011, MNRAS, 415, L40

Brodie J. P., Romanowsky A. J., Strader J., Forbes D. A., 2011, AJ, 142, 199

Brodie J. P., Strader J., 2006, ARA&A, 44, 193

Brodie J. P., Strader J., Denicoló G., Beasley M. A., Cenarro A. J., Larsen S. S., Kuntschner H., Forbes D. A., 2005, AJ, 129, 2643

Brough S., Forbes D. A., Kilborn V. A., Couch W., Colless M., 2006, MNRAS, 369, 1351

Buchdahl H. A., 1970, MNRAS, 150, 1

Bureau M., Athanassoula E., 1999, ApJ, 522, 686

Burkert A., Tremaine S., 2010, ApJ, 720, 516

Byrd G., Valtonen M., 1990, ApJ, 350, 89

Cantiello M., Blakeslee J. P., Raimondo G., Mei S., Brocato E., Capaccioli M., 2005, ApJ, 634, 239

Cappellari M. et al., 2006, MNRAS, 366, 1126

Cappellari M. et al., 2007, MNRAS, 379, 418

Cappellari M. et al., 2011, MNRAS, 413, 813

Cappellari M., McDermid R. M., Alatalo K., Blitz L., Bois M., Bournaud F., Bureau, 2012, Nature, 484, 485

Cappellari M. et al., 2013, MNRAS, 432, 1709

Caprio M., 2005, Computer Physics Communications, 171, 107

Chemin L., de Blok W. J. G., Mamon G. A., 2011, AJ, 142, 109

Chies-Santos A. L., Larsen S. S., Kuntschner H., Anders P., Wehner E. M., Strader J., Brodie J. P., Santos J. F. C., 2011a, A&A, 525, A20

Chies-Santos A. L., Larsen S. S., Wehner E. M., Kuntschner H., Strader J., Brodie J. P., 2011b, A&A, 525, A19

Chies-Santos A. L., Pastoriza M. G., Santiago B. X., Forbes D. A., 2006, A&A, 455, 453

Cho J., Sharples R. M., Blakeslee J. P., Zepf S. E., Kundu A., Kim H.-S., Yoon S.-J., 2012, ArXiv e-prints

Chomiuk L., Strader J., Brodie J. P., 2008, AJ, 136, 234

Coccato L. et al., 2009, MNRAS, 394, 1249

Cole D. R., Dehnen W., Read J. I., Wilkinson M. I., 2012, MNRAS, 426, 601

Cole D. R., Dehnen W., Wilkinson M. I., 2011, MNRAS, 416, 1118

Conroy C., Dutton A. A., Graves G. J., Mendel J. T., van Dokkum P. G., 2013, ApJ, 776, L26

Conroy C., van Dokkum P. G., 2012, ApJ, 760, 71

Cook M., Lapi A., Granato G. L., 2009, MNRAS, 397, 534

Cooper M. C., Newman J. A., Davis M., Finkbeiner D. P., Gerke B. F., 2012, in Astrophysics Source Code Library, record ascl:1203.003, p. 3003

Côté P., 1999, AJ, 118, 406

Côté P., Marzke R. O., West M. J., 1998, ApJ, 501, 554

Côté P., McLaughlin D. E., Cohen J. G., Blakeslee J. P., 2003, ApJ, 591, 850

Côté P. et al., 2001, ApJ, 559, 828

Cretton N., Naab T., Rix H.-W., Burkert A., 2001, ApJ, 554, 291

Croton D. J., 2006, MNRAS, 369, 1808

da Costa L. N. et al., 1998, AJ, 116, 1

Danese L., de Zotti G., di Tullio G., 1980, A&A, 82, 322

Das P. et al., 2008, Astronomische Nachrichten, 329, 940

de Lorenzi F. et al., 2009, MNRAS, 395, 76

de Lorenzi F., Gerhard O., Saglia R. P., Sambhus N., Debattista V. P., Pannella M., Méndez R. H., 2008, MNRAS, 385, 1729

de Vaucouleurs G., 1991, Science, 254, 1667

Deason A. J., Belokurov V., Evans N. W., 2011, MNRAS, 411, 1480

Deason A. J. et al., 2012, MNRAS, 425, 2840

Debattista V. P., Kazantzidis S., van den Bosch F. C., 2013, ArXiv e-prints

deBlok W. J. G., Bosma A., 2002, A&A, 385, 816

Dekel A. et al., 2009, Nature, 457, 451

Dekel A., Stoehr F., Mamon G. A., Cox T. J., Novak G. S., Primack J. R., 2005, Nature, 437, 707

Del Popolo A., 2012, MNRAS, 424, 38

Del Popolo A., Cardone V. F., 2012, MNRAS, 423, 1060

Di Cintio A., Brook C. B., Macciò A. V., Stinson G. S., Knebe A., Dutton A. A., Wadsley J., 2013, MNRAS

Diemand J., Madau P., Moore B., 2005, MNRAS, 364, 367

Douglas N. G. et al., 2007, ApJ, 664, 257

Eggen O. J., Lynden-Bell D., Sandage A. R., 1962, ApJ, 136, 748

Elmegreen B. G., Elmegreen D. M., Fernandez M. X., Lemonias J. J., 2009, ApJ, 692, 12

Elmegreen B. G., Malhotra S., Rhoads J., 2012, ArXiv e-prints

Emsellem E. et al., 2011, MNRAS, 414, 888

Emsellem E. et al., 2007, MNRAS, 379, 401

Faber S. M. et al., 2003, in Society of Photo-Optical Instrumentation Engineers (SPIE) Conference Series, Vol. 4841, Society of Photo-Optical Instrumentation Engineers (SPIE) Conference Series, Iye M., Moorwood A. F. M., eds., pp. 1657–1669

Faber S. M. et al., 1997, AJ, 114, 1771

Faifer F. R. et al., 2011, MNRAS, 416, 155

Falco M., Hansen S. H., Wojtak R., Brinckmann T., Lindholmer M., Pandolfi S., 2013a, ArXiv e-prints

Falco M., Mamon G. A., Wojtak R., Hansen S. H., Gottlöber S., 2013b, ArXiv e-prints

Fall S. M., Efstathiou G., 1980, MNRAS, 193, 189

Fan X., Strauss M. A., Richards G. T., Hennawi J. F., Becker R. H., White R. L., Diamond-Stanic, 2006, AJ, 131, 1203

Faraoni V., Capozziello S., 2011, Beyond Einstein Gravity

Feigelson E. D., Babu G. J., 1992, ApJ, 397, 55

Ferrarese L., 2002, ApJ, 578, 90

Ferrarese L. et al., 2006, ApJS, 164, 334

Ferrarese L., Ford H., 2005, Space Sci. Rev., 116, 523

Ferrarese L., Merritt D., 2000, ApJ, 539, L9

Filippenko A. V., Chornock R., 2000, IAU Circ., 7511, 2

Forbes D. A., Brodie J. P., Grillmair C. J., 1997a, AJ, 113, 1652

Forbes D. A., Brodie J. P., Huchra J., 1996a, AJ, 112, 2448

Forbes D. A., Brodie J. P., Huchra J., 1997b, AJ, 113, 887

Forbes D. A., Franx M., Illingworth G. D., Carollo C. M., 1996b, ApJ, 467, 126

Forbes D. A., Ponman T., O'Sullivan E., 2012a, MNRAS, 425, 66

Forbes D. A., Ponman T., O'Sullivan E., 2012b, MNRAS, 425, 66

Forbes D. A., Proctor R., Strader J., Brodie J. P., 2007, ApJ, 659, 188

Forbes D. A., Sánchez-Blázquez P., Phan A. T. T., Brodie J. P., Strader J., Spitler L., 2006, MNRAS, 366, 1230

Forbes D. A., Spitler L. R., Strader J., Romanowsky A. J., Brodie J. P., Foster C., 2011, MNRAS, 413, 2943

Forestell A. D., Gebhardt K., 2010, ApJ, 716, 370

Foster C., Arnold J. A., Forbes D. A., Pastorello N., Romanowsky A. J., Spitler L. R., Strader J., Brodie J. P., 2013, MNRAS, 435, 3587

Foster C. et al., 2011, MNRAS, 415, 3393

Fried J. W., Illingworth G. D., 1994, AJ, 107, 992

Gallagher J. S., Knapp G. R., Faber S. M., Balick B., 1977, ApJ, 215, 463

Geisler D., Lee M. G., Kim E., 1996, AJ, 111, 1529

Gerhard O., Jeske G., Saglia R. P., Bender R., 1998, MNRAS, 295, 197

Giacintucci S. et al., 2012, ApJ, 755, 172

Gobat R. et al., 2011, A&A, 526, A133

Goudfrooij P., Mack J., Kissler-Patig M., Meylan G., Minniti D., 2001, MNRAS, 322, 643

Governato F. et al., 2012, MNRAS, 422, 1231

Graham A. W., 2008, ApJ, 680, 143

Graham A. W., Driver S. P., 2007, ApJ, 655, 77

Graham A. W., Driver S. P., Petrosian V., Conselice C. J., Bershady M. A., Crawford S. M., Goto T., 2005, AJ, 130, 1535

Graham A. W., Onken C. A., Athanassoula E., Combes F., 2011, MNRAS, 412, 2211

Graham A. W., Scott N., 2012, ArXiv e-prints

Green A. W. et al., 2010, Nature, 467, 684

Gültekin K., Cackett E. M., Miller J. M., Di Matteo T., Markoff S., Richstone D. O., 2009a, ApJ, 706, 404

Gültekin K. et al., 2009b, ApJ, 698, 198

Guo Q., Cole S., Eke V., Frenk C., 2011, MNRAS, 417, 370

Hargis J. R., Rhode K. L., Strader J., Brodie J. P., 2011, ApJ, 738, 113

Harris G. L. H., Harris W. E., 2011, MNRAS, 410, 2347

Harris W. E., Harris G. L. H., Layden A. C., Wehner E. M. H., 2007a, ApJ, 666, 903

Harris W. E., Harris G. L. H., Layden A. C., Wehner E. M. H., 2007b, ApJ, 666, 903

Hernquist L., 1990, ApJ, 356, 359

Hetznecker H., Burkert A., 2006, MNRAS, 370, 1905

Ho L. C. et al., 2001, ApJ, 549, L51

Hoffman L., Cox T. J., Dutta S., Hernquist L., 2010, ApJ, 723, 818

Hopkins P. F., Cox T. J., Dutta S. N., Hernquist L., Kormendy J., Lauer T. R., 2009, ApJS, 181, 135

Hopkins P. F., Hernquist L., Cox T. J., Robertson B., Krause E., 2007, ApJ, 669, 67

Hu J., 2008, MNRAS, 386, 2242

Hubble E. P., 1926, ApJ, 64, 321

Humphrey P. J., Buote D. A., Gastaldello F., Zappacosta L., Bullock J. S., Brighenti F., Mathews W. G., 2006, ApJ, 646, 899

Hwang H. S. et al., 2008, ApJ, 674, 869

Jahnke K., Macciò A. V., 2011, ApJ, 734, 92

Jarrett T. H., Chester T., Cutri R., Schneider S. E., Huchra J. P., 2003, AJ, 125, 525

Jeans J. H., 1915, MNRAS, 76, 70

Jensen J. B., Tonry J. L., Barris B. J., Thompson R. I., Liu M. C., Rieke M. J., Ajhar E. A., Blakeslee J. P., 2003, ApJ, 583, 712

Joanes D., Gill C. A., 1998, The Statistician, 47, 183

Johansson P. H., Burkert A., Naab T., 2009, ApJ, 707, L184

Jordán A. et al., 2007, ApJS, 171, 101

Kafle P. R., Sharma S., Lewis G. F., Bland-Hawthorn J., 2012, ApJ, 761, 98

Kartha S. S., Forbes D. A., Spitler L. R., Romanowsky A. J., Arnold J. A., Brodie J. P., 2013, ArXiv e-prints

Kissler-Patig M., Richtler T., Storm J., della Valle M., 1997, A&A, 327, 503

Kochanek C. S., 1995, ApJ, 453, 545

Komatsu E. et al., 2009, ApJS, 180, 330

Kormendy J., Bender R., 2011, Nature, 469, 377

Kormendy J., Bender R., 2012, ApJS, 198, 2

Kormendy J., Ho L. C., 2013, ARA&A, 51, 511

Krajnović D., Cappellari M., de Zeeuw P. T., Copin Y., 2006, MNRAS, 366, 787

Krajnović D. et al., 2011, MNRAS, 414, 2923

Kravtsov A. V., Gnedin O. Y., 2005, ApJ, 623, 650

Kronawitter A., Saglia R. P., Gerhard O., Bender R., 2000, A&AS, 144, 53

Kruijssen J. M. D., Pelupessy F. I., Lamers H. J. G. L. M., Portegies Zwart S. F., Bastian N., Icke V., 2012, MNRAS, 421, 1927

Kundu A., Whitmore B. C., 2001, AJ, 122, 1251

Kuzio de Naray R., McGaugh S. S., de Blok W. J. G., 2008, ApJ, 676, 920

Laporte C. F. P., White S. D. M., Naab T., Ruszkowski M., Springel V., 2012, MNRAS, 424, 747

Larsen S. S., Brodie J. P., Beasley M. A., Forbes D. A., Kissler-Patig M., Kuntschner H., Puzia T. H., 2003, ApJ, 585, 767

Larsen S. S., Brodie J. P., Huchra J. P., Forbes D. A., Grillmair C. J., 2001, AJ, 121, 2974

Larsen S. S., Brodie J. P., Strader J., 2005, A&A, 443, 413

Larson R. B., 1975, MNRAS, 173, 671

Lee M. G., Hwang H. S., Kim S. C., Park H. S., Geisler D., Sarajedini A., Harris W. E., 2008a, ApJ, 674, 886

Lee M. G., Park H. S., Hwang H. S., Arimoto N., Tamura N., Onodera M., 2010a, ApJ, 709, 1083

Lee M. G., Park H. S., Hwang H. S., Arimoto N., Tamura N., Onodera M., 2010b, ApJ, 709, 1083

Lee M. G., Park H. S., Kim E., Hwang H. S., Kim S. C., Geisler D., 2008b, ApJ, 682, 135

Macciò A. V., Dutton A. A., van den Bosch F. C., 2008, MNRAS, 391, 1940

Marconi A., Hunt L. K., 2003, ApJ, 589, L21

Martínez-Delgado D. et al., 2010, AJ, 140, 962

Martizzi D., Teyssier R., Moore B., 2013, MNRAS, 432, 1947

Martizzi D., Teyssier R., Moore B., Wentz T., 2012, MNRAS, 422, 3081

Masters K. L. et al., 2010, ApJ, 715, 1419

Mayer L., Kazantzidis S., Escala A., Callegari S., 2010, Nature, 466, 1082

McConnell N. J., Ma C.-P., 2012, ArXiv e-prints

McConnell N. J., Ma C.-P., Gebhardt K., Wright S. A., Murphy J. D., Lauer T. R., Graham J. R., Richstone D. O., 2011, Nature, 480, 215

McDermid R. M. et al., 2006, MNRAS, 373, 906

McMillan P. J., Athanassoula E., Dehnen W., 2007, MNRAS, 376, 1261

Mead J. M. G., King L. J., Sijacki D., Leonard A., Puchwein E., McCarthy I. G., 2010, MNRAS, 406, 434

Mei S. et al., 2007, ApJ, 655, 144

Menci N., Fiore F., Lamastra A., 2012, MNRAS, 421, 2384

Merrett H. R. et al., 2003, MNRAS, 346, L62

Merritt D., Ferrarese L., 2001, MNRAS, 320, L30

Mieske S. et al., 2006, ApJ, 653, 193

Milgrom M., 1983, ApJ, 270, 371

Misgeld I., Mieske S., Hilker M., Richtler T., Georgiev I. Y., Schuberth Y., 2011, A&A, 531, A4

Miyazaki S. et al., 2002, PASJ, 54, 833

Moore B., Diemand J., Madau P., Zemp M., Stadel J., 2006, MNRAS, 368, 563

Moore B., Ghigna S., Governato F., Lake G., Quinn T., Stadel J., Tozzi P., 1999, ApJ, 524, L19

Muñoz R. P. et al., 2013, ArXiv e-prints

Muratov A. L., Gnedin O. Y., 2010, ApJ, 718, 1266

Naab T., Johansson P. H., Ostriker J. P., Efstathiou G., 2007, ApJ, 658, 710

Nagar N. M., Falcke H., Wilson A. S., 2005, A&A, 435, 521

Nantais J. B., Huchra J. P., 2010, AJ, 139, 2620

Napolitano N. R. et al., 2011, MNRAS, 411, 2035

Napolitano N. R. et al., 2009, MNRAS, 393, 329

Navarro J. F., Frenk C. S., White S. D. M., 1997, ApJ, 490, 493

Newman A. B., Treu T., Ellis R. S., Sand D. J., 2013, ApJ, 765, 25

Newman J. A. et al., 2012, ArXiv e-prints

Nipoti C., Treu T., Ciotti L., Stiavelli M., 2004, MNRAS, 355, 1119

Norris M. A. et al., 2012, MNRAS, 421, 1485

Novak G. S., Cox T. J., Primack J. R., Jonsson P., Dekel A., 2006, ApJ, 646, L9

Oh S.-H., Brook C., Governato F., Brinks E., Mayer L., de Blok W. J. G., Brooks A., Walter F., 2011, AJ, 142, 24

Oliva E., Origlia L., Kotilainen J. K., Moorwood A. F. M., 1995, A&A, 301, 55

Olsen K. A. G., Miller B. W., Suntzeff N. B., Schommer R. A., Bright J., 2004, AJ, 127, 2674

Omukai K., Schneider R., Haiman Z., 2008, ApJ, 686, 801

Oser L., Ostriker J. P., Naab T., Johansson P. H., Burkert A., 2010, ApJ, 725, 2312

O'Sullivan E., Forbes D. A., Ponman T. J., 2001, MNRAS, 328, 461

Ouchi M. et al., 2004, ApJ, 611, 660

Park D., Kelly B. C., Woo J.-H., Treu T., 2012a, ArXiv e-prints

Park H. S., Lee M. G., Hwang H. S., 2012b, ApJ, 757, 184

Peñarrubia J., Pontzen A., Walker M. G., Koposov S. E., 2012, ApJ, 759, L42

Pellegrini S., Siemiginowska A., Fabbiano G., Elvis M., Greenhill L., Soria R., Baldi A., Kim D. W., 2007, ApJ, 667, 749

Peng E. W. et al., 2006, ApJ, 639, 95

Peter A. H. G., Moody C. E., Benson A. J., Kamionkowski M., 2010, ArXiv e-prints

Peter A. H. G., Rocha M., Bullock J. S., Kaplinghat M., 2013, MNRAS, 430, 105

Peterson B. M. et al., 2004, ApJ, 613, 682

Phoebe Schauer A. T., Remus R.-S., Burkert A., Johansson P. H., 2013, ArXiv e-prints

Pierce M. et al., 2006, MNRAS, 366, 1253

Pinkney J. et al., 2003, ApJ, 596, 903

Pontzen A., Governato F., 2012, MNRAS, 421, 3464

Pota V. et al., 2013, MNRAS, 428, 389

Press W. H., Teukolsky S. A., Vetterling W. T., Flannery B. P., 1992, Numerical recipes in C. The art of scientific computing

Prieto J. L., Gnedin O. Y., 2008, ApJ, 689, 919

Proctor R. N., Forbes D. A., Forestell A., Gebhardt K., 2005, MNRAS, 362, 857

Proctor R. N., Forbes D. A., Romanowsky A. J., Brodie J. P., Strader J., Spolaor M., Mendel J. T., Spitler L., 2009, MNRAS, 398, 91

Prugniel P., Simien F., 1996, A&A, 309, 749

Puzia T. H. et al., 2004, A&A, 415, 123

Rhode K. L., 2012, AJ, 144, 154

Rhode K. L., Zepf S. E., 2001, AJ, 121, 210

Richardson T., Fairbairn M., 2013, ArXiv e-prints

Richtler T., Salinas R., Misgeld I., Hilker M., Hau G. K. T., Romanowsky A. J., Schuberth Y., Spolaor M., 2011, A&A, 531, A119

Rocha M., Peter A. H. G., Bullock J. S., Kaplinghat M., Garrison-Kimmel S., Oñorbe J., Moustakas L. A., 2013, MNRAS, 430, 81

Rodighiero G., Daddi E., Baronchelli I., Cimatti A., Renzini A., Aussel H., Popesso P., Lutz, 2011, ApJ, 739, L40

Romanowsky A. J., Douglas N. G., Arnaboldi M., Kuijken K., Merrifield M. R., Napolitano N. R., Capaccioli M., Freeman K. C., 2003, Science, 301, 1696

Romanowsky A. J., Strader J., Brodie J. P., Mihos J. C., Spitler L. R., Forbes D. A., Foster C., Arnold J. A., 2011, ArXiv e-prints

Romanowsky A. J., Strader J., Spitler L. R., Johnson R., Brodie J. P., Forbes D. A., Ponman T., 2009, AJ, 137, 4956

Rubin V. C., Ford, Jr. W. K., 1970, ApJ, 159, 379

Rusli S. P., Erwin P., Saglia R. P., Thomas J., Fabricius M., Bender R., Nowak N., 2013a, AJ, 146, 160

Rusli S. P. et al., 2013b, AJ, 146, 45

Sadoun R., Colin J., 2012, MNRAS, 426, L51

Sand D. J., Treu T., Smith G. P., Ellis R. S., 2004, ApJ, 604, 88

Sandage A., Bedke J., 1994, The Carnegie Atlas of Galaxies. Volumes I, II., Sandage, A. & Bedke, J., ed.

Schlegel D. J., Finkbeiner D. P., Davis M., 1998, ApJ, 500, 525

Schuberth Y., Richtler T., Hilker M., Dirsch B., Bassino L. P., Romanowsky A. J., Infante L., 2010, A&A, 513, A52

Schuberth Y., Richtler T., Hilker M., Salinas R., Dirsch B., Larsen S. S., 2012, A&A, 544, A115

Scott N., Graham A. W., 2013, ApJ, 763, 76

Searle L., Zinn R., 1978, ApJ, 225, 357

Sérsic J. L., 1963, Boletin de la Asociacion Argentina de Astronomia La Plata Argentina, 6, 41

Shapiro K. L., Genzel R., Förster Schreiber N. M., 2010, MNRAS, 403, L36

Shapley H., Curtis H. D., 1921, Bulletin of the National Research Council, Vol. 2, Part 3, No. 11, p. 171-217, 2, 171

Sharma S., Johnston K. V., Majewski S. R., Bullock J., Muñoz R. R., 2011, ApJ, 728, 106

Sil'chenko O. K., Afanasiev V. L., Chavushyan V. H., Valdes J. R., 2002, ApJ, 577, 668

Simien F., Prugniel P., 2000, A&AS, 145, 263

Sinnott B., Hou A., Anderson R., Harris W. E., Woodley K. A., 2010, AJ, 140, 2101

Skrutskie M. F. et al., 2006, AJ, 131, 1163

Snyder G. F., Hopkins P. F., Hernquist L., 2011, ApJ, 728, L24

Sofue Y., Rubin V., 2001, ARA&A, 39, 137

Spitler L. R., Forbes D. A., Strader J., Brodie J. P., Gallagher J. S., 2008, MNRAS, 385, 361

Spitler L. R., Larsen S. S., Strader J., Brodie J. P., Forbes D. A., Beasley M. A., 2006, AJ, 132, 1593

Spitler L. R., Romanowsky A. J., Diemand J., Strader J., Forbes D. A., Moore B., Brodie J. P., 2012, MNRAS, 423, 2177

Spitzer L., 1987, Dynamical evolution of globular clusters

Spolaor M., Forbes D. A., Hau G. K. T., Proctor R. N., Brough S., 2008a, MNRAS, 385, 667

Spolaor M., Forbes D. A., Proctor R. N., Hau G. K. T., Brough S., 2008b, MNRAS, 385, 675

Springel V. et al., 2008, MNRAS, 391, 1685

Strader J., Brodie J. P., Cenarro A. J., Beasley M. A., Forbes D. A., 2005, AJ, 130, 1315

Strader J., Brodie J. P., Spitler L., Beasley M. A., 2006, AJ, 132, 2333

Strader J. et al., 2011, ApJS, 197, 33

Tal T., van Dokkum P. G., Nelan J., Bezanson R., 2009, AJ, 138, 1417

Teodorescu A. M., Méndez R. H., Bernardi F., Riffeser A., Kudritzki R. P., 2010, ApJ, 721, 369

Teyssier R., Pontzen A., Dubois Y., Read J. I., 2013, MNRAS, 429, 3068

Thomas J., Saglia R. P., Bender R., Erwin P., Fabricius M., 2013, ArXiv e-prints

Thomas J., Saglia R. P., Bender R., Thomas D., Gebhardt K., Magorrian J., Corsini E. M., Wegner G., 2007, MNRAS, 382, 657

Thomas J. et al., 2011, MNRAS, 415, 545

Tomita A., Aoki K., Watanabe M., Takata T., Ichikawa S.-i., 2000, AJ, 120, 123

Tonini C., 2013, ApJ, 762, 39

Tonry J., Davis M., 1979, AJ, 84, 1511

Tonry J. L., Dressler A., Blakeslee J. P., Ajhar E. A., Fletcher A. B., Luppino G. A., Metzger M. R., Moore C. B., 2001, ApJ, 546, 681

Toomre A., Toomre J., 1972, ApJ, 178, 623

Tortora C., Romanowsky A. J., Cardone V. F., Napolitano N. R., Jetzer P., 2013, ArXiv e-prints

Tremaine S. et al., 2002, ApJ, 574, 740

Usher C. et al., 2012, MNRAS, 426, 1475

van der Marel R. P., Franx M., 1993, ApJ, 407, 525

Vesperini E., Zepf S. E., Kundu A., Ashman K. M., 2003, ApJ, 593, 760

Vitvitska M., Klypin A. A., Kravtsov A. V., Wechsler R. H., Primack J. R., Bullock J. S., 2002, ApJ, 581, 799

Walker M. G., Mateo M., Olszewski E. W., Peñarrubia J., Wyn Evans N., Gilmore G., 2009, ApJ, 704, 1274

Walker M. G., Peñarrubia J., 2011, ApJ, 742, 20

Walter F., Brinks E., de Blok W. J. G., Bigiel F., Kennicutt, Jr. R. C., Thornley M. D., Leroy A., 2008, AJ, 136, 2563

Wegner G. A., Corsini E. M., Thomas J., Saglia R. P., Bender R., Pu S. B., 2012, AJ, 144, 78

Weijmans A.-M. et al., 2009, MNRAS, 398, 561

Weil M. L., Pudritz R. E., 2001, ApJ, 556, 164

Weinmann S. M., Neistein E., Dekel A., 2011, MNRAS, 417, 2737

Williams M. J., Bureau M., Cappellari M., 2010, MNRAS, 409, 1330

Wisnioski E. et al., 2011, MNRAS, 417, 2601

Wolf J., Martinez G. D., Bullock J. S., Kaplinghat M., Geha M., Muñoz R. R., Simon J. D., Avedo F. F., 2010, MNRAS, 406, 1220

Woodley K. A., Gómez M., Harris W. E., Geisler D., Harris G. L. H., 2010, AJ, 139, 1871

Yoon S.-J., Lee S.-Y., Blakeslee J. P., Peng E. W., Sohn S. T., Cho J., Kim H.-S., Chung C., 2011a, ApJ, 743, 150

Yoon S.-J., Sohn S. T., Lee S.-Y., Kim H.-S., Cho J., Chung C., Blakeslee J. P., 2011b, ApJ, 743, 149

Yoon S.-J., Yi S. K., Lee Y.-W., 2006, Science, 311, 1129

Younes G., Porquet D., Sabra B., Grosso N., Reeves J. N., Allen M. G., 2010, A&A, 517, A33

Zhang X., Lu Y., Yu Q., 2012, ApJ, 761, 5

Zhang Z., Xu H., Wang Y., An T., Xu Y., Wu X.-P., 2007, ApJ, 656, 805

Zitrin A. et al., 2010, MNRAS, 408, 1916